MICROSTRUCTURAL CHARACTERIZATION OF RAPIDLY QUENCHED AND ANNEALED Nd-Fe-B HARD MAGNETIC ALLOYS USING MÖSSBAUER SPECTROSCOPY AND X-RAY DIFFRACTION

by

Bryan P. Templeton

ProQuest LLC.
789 East Eisenhower Parkway
P.O. Box 1346
Ann Arbor, MI 48106 – 1346

A thesis submitted to the Faculty and the Board of Trustees of the Colorado School of Mines in partial fulfillment of the requirements for the degree of Master of Science (Metallurgical and Materials Engineering).

Golden, Colorado

Date 3/31/98

Signed: _____
Bryan P. Templeton

Approved: _____
Dr. John P. Hager
Thesis Co-Advisor

_____
Dr. Don L. Williamson
Thesis Co-Advisor

Golden, Colorado

Date 3/31/98

_____
Dr. John J. Moore
Professor and Head, Department of
Metallurgical and Materials Engineering

ABSTRACT

In this study, Mössbauer spectroscopy and x-ray diffraction were used to characterize the microstructure of Nd-Fe-B nano-structured hard magnetic powders. Eight alloys with four different nominal compositions were analyzed. Alloys with no refractory metal additions, with 2% Nb additions, with 2% Ti additions, and with 1% Nb and 1% Ti additions were investigated. The as-received powders had been rapidly quenched into a metallic glass. Annealing experiments were performed to crystallize the metastable amorphous precursor into a matrix containing nano-scale $Nd_2Fe_{14}B$ crystallites. The as-quenched and annealed samples were characterized with ^{57}Fe Mössbauer spectroscopy and x-ray diffraction. Mössbauer spectroscopy was used to determine the iron-containing phase composition and distribution in the samples. Using the Scherrer equation and x-ray diffraction line broadening, a technique was developed and applied to determine the grainsizes of $Nd_2Fe_{14}B$ crystallites in the various alloy samples. X-ray diffraction was also used to confirm the phases detected by the Mössbauer spectroscopy, and to detect any non iron-containing phases present in the matrix. The final microstructure evolved in the alloys

consisted of $Nd_2Fe_{14}B$ crystallites with an average grainsize on the order of 30-40 nm, separated by a residual disordered grain boundary phase (25-35% of the total volume in optimally annealed samples). The magnetic coercivity of the powders was found to be highly dependent on the amount of crystalline $Nd_2Fe_{14}B$ present in the head samples, but did not seem to be dependent on the grainsize or phase distribution of the annealed samples. The magnetic remanence did not seem to be affected by the amount of crystallinity in the head samples, the grainsize distribution or the phase distribution of the annealed samples. The refractory metal additions were successful at preventing grain growth. The grainsize developed in the samples that contained refractory metal additions seemed to be independent of annealing time or temperature. The alloys with the 1% Ti and 1% Nb additions showed the finest grainsize at 30 -34 nm, but the finer grainsize did not improve magnetic properties. The alloy that did not contain any refractory metal additions experienced continual grain growth until a 50 nm grainsize, at which no further growth occurred independent of annealing time or temperature. Thermodynamic analysis suggests that niobium and titanium borides are precipitated in this alloy system, perhaps in the melt before casting.

TABLE OF CONTENTS

LIST OF TABLES

LIST OF FIGURES

ACKNOWLEDGMENTS

Funding for this research was provided by Rhodia Rare Earths and Gallium. I would like to thank Dr. Charles O. Bounds, Director of Research and Development, for supporting this research, supplying reference materials, and technical advice. I would like to thank Dr. Bao-Min Ma, Project Coordinator, for his assistance, technical expertise and advice, and for serving on the thesis committee. I would also like to thank Dr. Valerie Archambault of Rhodia's Centre De Recherches d' Aubervilliers in Paris and her co-workers Nicole Ouillon, Pascale Fevrier, and Daniel Pèrè for their technical expertise, cooperation and collaboration in several aspects of this research effort.

The thesis committee members included Dr. John P. Hager (advisor), Dr. Don L. Williamson (co-advisor), Dr. Chester J. Van Tyne, and Dr. Bao-Min Ma. Dr. Williamson was invaluable in his assistance with all details of Mössbauer spectroscopy and x-ray diffraction, with clever insights into all technical matters of the project, and attention to scientific detail. I would like to thank the faculty of the Metallurgical and Materials Engineering Department at the Colorado School of Mines for all their assistance and support. I would like to extend a special thank you to Steve Stephens of Iron Carbide Holdings for allowing the use of Iron

Carbide Holdings' Mössbauer system on several occasions.

A special acknowledgment must be made to Dr. John P. Hager for his guidance and patience in completing this project. His administrative and mediating skills, together with his technical expertise and uncompromising demand for excellence made this project possible and successful.

Chapter 1

INTRODUCTION

1.1 Ferromagnetism and Hard Magnets

Each electron in an atom has both an orbital magnetic dipole moment and a spin magnetic dipole moment that combine vectorially to produce an electronic magnetic moment [1]. There is also a nuclear magnetic dipole, but it is negligible in comparison to the electronic magnetic dipole [2]. All of the individual electronic magnetic dipole moments in an atom combine vectorially to produce an atomic resultant dipole moment. All of the atomic dipole moments in a sample of material combine vectorially to form a resultant magnetic moment **M**, which represents a magnetic moment per unit volume [1].

In ferromagnetic materials, some of the atoms align their resultant magnetic dipole moments to produce regions with strong magnetic dipole moments called magnetic domains [1]. Domains are generated in ferromagnetic materials because of a quantum physical effect called exchange coupling [1]. In exchange coupling, the spins of the electrons in one atom interact with the spins of electrons in neighboring atoms. The result is an alignment of the magnetic dipole moments of the atoms, in spite of the randomizing tendency of thermal energy [1]. The magnetization vector **M** is not constant within a macroscopic sample of material. However, the magnitude of the vectoral sum within a domain is uniform and is termed the spontaneous magnetization M_s. The direction of the magnetization vector varies from domain to domain and usually follows a specific crystallographic axis [2]. In equilibrium, the magnetization over the entire volume

of a sample sums to zero [2]. Figure 1-1 is a schematic representation of a polycrystalline ferromagnet in the stable unmagnetized state, and in the state with a net remanent magnetization. When an external field **H** of gradually

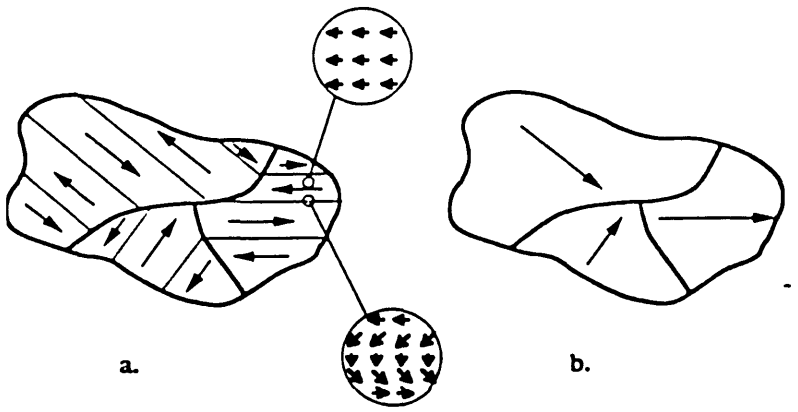

Figure 1-1: Schematic representation of a polycrystalline ferromagnet in the stable unmagnetized state (a), and in the state with a net remanent magnetization (b). Grain boundaries and domain walls are represented by the dark and thin lines respectively. Inserts show the alignment of the atomic moments within domains and in the domain walls [2].

increasing strength is applied to a ferromagnetic material, two effects are produced [1]. One, the domains that are oriented along the external field grow at the expense of the domains not favorably oriented. Two, the orientation of the dipoles within a domain are shifted, as a unit, to become closer to the external field. In ferromagnetic materials, the magnetic field generated by domain alignment can partially persist after **H** is removed, therefore creating a permanent magnet [1]. Figure 1-1 illustrates the difference between a ferromagnet in its equilibrium unmagnetized state, and in the remanent state after saturation in a horizontal magnetic field which eliminated the domains in each crystallite.

Because an external field irreversibly changes the state of magnetization of a ferromagnetic material by altering the domain alignment, permanent magnets exhibit a hysteresis behavior. Figure 1-2 shows a typical magnetization curve M vs. H [2]. In Figure 1-2, M is the material magnetization, and H is the applied

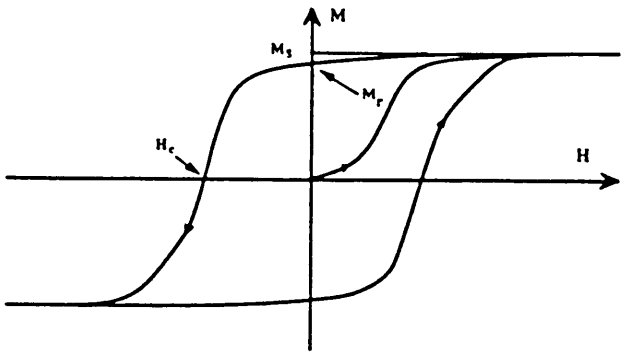

Figure 1-2: A typical hysteresis loop M vs. H for a permanent magnet [2].

field. The loop shows that as the external field H is applied, the material magnetization increases until saturation, M_s. As the external field intensity is decreased back to zero, the magnetization does not return to zero, but maintains a value M_r called the magnetic remanence. As the external field is applied in the opposite direction, the magnetization continually decreases until it reaches zero at some non-zero value of H, called the magnetic coercivity H_c. Although the M_s is an intrinsic property of the ferromagnetic phase, the remanence M_r and coercivity H_c, defined as the points where the loop cuts the axes, are not. "The remanence M_r and coercivity H_c depend in a complex way on the particle size, shape, and metallurgical microstructure of the magnet" [2].

The B vs. H hysteresis loop shown in Figure 1-3 is related to the M vs. H

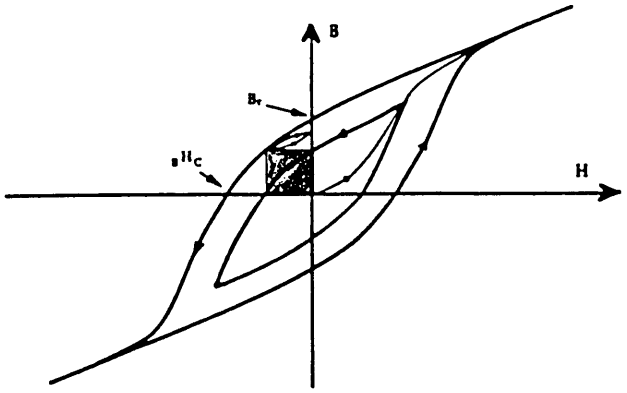

Figure 1-3: A typical hysteresis loop B vs. H for a permanent magnet. The shaded rectangle of maximum area in the second quadrant represents the energy product $(BH)_{max}$ [2].

loop of Figure 1-2 by the following equation which defines the magnetic flux density in a magnet :

$$B = \mu_o (H + M) \qquad [1.1]$$

where:

B = B-field; magnetic flux density [Tesla]
H = H-Field; magnetic field intensity [A/m]
M = Magnetization (magnetic moment / volume) [$J/(Tm^3)$]
μ_o = magnetic permeability of free space [$4\pi\ 10^{-7}$ Tm/A]

In this format, the remanence B_r is equal to $\mu_o M_r$ since H=0 at this point on the

curve, but the coercivity ${}_BH_c$ may measure a lesser value than before. H_c is sometimes referred to as the intrinsic coercivity, although coercivity is not an intrinsic property of the ferromagnetic phase [2]. M vs. H loops are typically measured by physicists interested in magnetism, whereas B vs. H loops typically are found in engineering applications. "The maximum potential energy is obtained at the point on the loop, in the second quadrant, where the product -B · H is maximized" [2]. Figure 1-3 shows $(BH)_{max}$ as the shaded region. $(BH)_{max}$, a commonly measured and published value, is twice the maximum potential energy.

Ferromagnets are divided into two categories by their hysteresis behavior. Soft magnetic materials have large magnetization saturation points and therefore large remanence values, but almost no coercivity. It is easy to magnetize soft magnetic materials in an applied field, but they do not resist reverse domain formation in an oppositely applied field. Electrical steels used in electrical generators and motors are soft magnetic materials. Hard magnetic materials, also called permanent magnetic materials, have large coercivities.

"The ideal permanent magnet would have a square hysteresis loop where the remanence has the highest possible value, $M_r = M_s$, and the magnetization remains independent of the applied reverse field up to H_c"[2]. Real hard magnets have the following intrinsic limitations [2]:

$$B_r \leq \mu_o M_s \qquad \textbf{[1.2]}$$

$${}_BH_c \leq M_s \qquad \textbf{[1.3]}$$

$$(BH)_{max} \leq (\mu_o M_r^2) / 4 \qquad \textbf{[1.4]}$$

The transition elements iron, cobalt, nickel and the rare earth elements like gadolinium, dysprosium, samarium, and neodymium and their alloys exhibit ferromagnetic behavior. Iron alloys usually generate a $\mu_o M_s$ less than ~ 2 T. Note that the $(BH)_{max}$ corresponding to $\mu_o M_s$ = 2 T is limited by equation [1.4] to a value less than 800 kJ/m^3. Cobalt and nickel alloys have lower magnetizations, and correspondingly smaller upper limits to their energy products. "Ferromagnetic alloys composed mainly of heavy rare-earths such as Dy or Ho, which have the largest atomic moment (10 μ_B) [μ_B is the Bohr magneton, a unit of magnetic dipole moment equivalent to the magnetic moment of the electron (9.27 x 10^{-24} J/T)] of any element in the periodic table, could in theory show energy products in excess of 3000 kJ/m^3 and produce a flux density approaching 4 T" [2]. Table 1-1 shows some typical properties of some commonly used oriented magnets [2].

TABLE 1-1: Typical Properties of Some Oriented Magnets [2].

Type	Main Phase	B_r (T)	$\mu_o M_s$ (T)	H_c (kA/m)	$_BH_c$ (kA/m)	$(BH)_{max}$ (kJ/m^3)
Ferrite	$SrFe_{12}O_{19}$	0.39	0.46	275	265	28
Alnico 5	$Fe_{48}Al_{16}Ni_{13}Co_{21}Cu_2$	1.28	1.40	54	52	43
Sm-Co	$SmCo_5$	0.88	0.95	1400	680	150
Sm-Co	Sm_2Co_{17}	1.08	1.15	900	800	220
Nd-Fe-B	$Nd_2Fe_{14}B$	1.25	1.34	1000	920	300

1.2 History of Rare Earth Magnets

Permanent magnet technology has come a long way in the last two millennia.

The first known permanent magnets were lodestones, naturally occurring ferromagnetic iron oxides that were aligned in the Earth's magnetic field during cooling from geologic activity. By 960-1279, the technology of magnetizing steel wire with lodestone or by cooling in a magnetic field, to produce compass needles, had been mastered in both China and Europe [2]. This relatively primitive technology that produced weak unstable carbon steel magnets was not significantly improved until the twentieth century. The first modern advances in hard magnets came from Japan, where in 1917, cobalt magnet steels were discovered [2]. Shortly after in 1931, Japanese know-how came through again when Alnico alloys, iron-aluminum-nickel-cobalt alloys (Table 1-1), the first truly permanent magnets, were discovered by Mishima [2]. The next advance came in the early 1950s in The Netherlands. The first synthetic hard ferrite magnets composed of iron oxides like $BaFe_{12}O_{19}$ or $SrFe_{12}O_{19}$ were developed at Philips, a Dutch company [2]. "Ferrites are cheap to produce, effective and reliable, and today, account for 90% of the mass and a little over half of the value of all hard magnets produced worldwide, an annual market worth roughly US$2-3 billion" [2].

Rare-earth permanent magnets represent the largest single breakthrough in permanent magnet technology. Working in the United States, Strnat is credited with drawing attention to the potential of rare-earth ferromagnetic alloys for permanent magnet applications in the 1960s [2]. The advantage of rare earth - transition metal alloys is the coupling of 3d and 4f elements. The 3d orbitals in Fe, Co, and Ni provide ample magnetization and increase Curie temperatures (the temperature above which thermal energy disrupts the exchange coupling that produces stable magnetic domains). The 4f orbitals of the rare-earth elements amplify the magnetocrystalline anisotropy required to maintain the metastable domain configuration required for hard magnetism. In addition, the 4f orbitals of the light rare earth elements readily undergo an exchange coupling

with the 3d orbitals of the ferromagnetic transition metals that leads to parallel alignment of the 3d and 4f magnetic moments, and therefore enhanced magnetization, **M** [2].

The first rare-earth permanent magnets were samarium-cobalt alloys. Philips bonded oriented $SmCo_5$ powder in resin, to produce the first samarium-cobalt magnet in 1967 with a energy product of 65 kJ/m^3 [2]. Shortly after, sintered magnets incorporating the $SmCo_5$ phase or the Sm_2Co_{17} phase led to energy products in excess of 200 kJ/m^3 [2] (Table 1-1). It is interesting to note that the typical Alnico 5 alloy listed in Table 1-1 has an energy product of only 43 kJ/m^3. Samarium-cobalt alloys persisted as the high-performance hard magnetic material of choice until uncertainties in the world cobalt supply in the late 1970s led to huge cobalt price fluctuations [2].

Attention was focused on iron-neodymium alloys to be the replacement for samarium-cobalt for several reasons. First, iron is the most abundant metal on earth and is therefore extremely accessible and cheap. In addition, ferromagnetic α-Fe has the largest 3d atomic magnetic moment of the ferromagnetic metals, 2.2 μ_B [2]. Third, neodymium is the most abundant magnetic light rare-earth element, and has the largest 4f magnetic moment, 3.3 μ_B [2]. Unfortunately, no magnetic Nd-Fe binary compound exists with a Curie temperature above 500°K. The research effort was redirected to finding a suitable ternary phase or a metastable phase produced during rapid quenching. In 1983, Sumitomo in Japan successfully produced a $Nd_{15}Fe_{77}B_8$ permanent magnet with an energy product of 290 kJ/m^3 [2]. Simultaneously, a General Motors research team in the United States including Koon, Hadjipanayis, Croat and Herbst, independently produced permanent magnets based on similar compositions, and identified the active hard magnetic phase as $Nd_2Fe_{14}B$ [2]. "Neodymium-iron-boron magnets currently hold the record for energy product,

which now exceeds 400 kJ/m^{3}" [2].

1.3 The $Nd_2Fe_{14}B$ Phase and Optimizing Magnetic Properties

Since the discovery of the $Nd_2Fe_{14}B$ phase as the active hard magnetic phase in Nd-Fe-B permanent magnets in 1983, there has been considerable effort to characterize its properties. The $Nd_2Fe_{14}B$ (2-14-1) phase is a stoichiometric line compound occurring in the Nd-Fe-B ternary system with a 1250°C melting point. It has a tetragonal crystal structure with a c-axis lattice parameter = 1.22 nm and an a-axis lattice parameter = 0.88 nm. The 2-14-1 crystal is complex with 68 atoms in the unit cell. Figure 1-4 shows the tetragonal unit cell. Because of its many-atom unit cell structure, the 2-14-1 phase has a complex x-ray diffraction

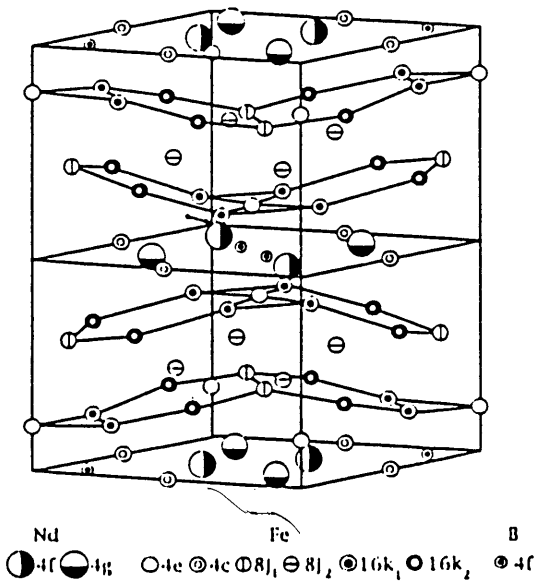

Figure 1-4: The tetragonal $Nd_2Fe_{14}B$ unit cell [2]. The Wyckoff notation used in the International Tables of X-ray Crystallography [3] identifies the atomic sites.

pattern. Figure 1-5 demonstrates the x-ray powder diffraction pattern for pure 2-14-1. The Curie temperature of the 2-14-1 phase is 585°K.

As mentioned in section 1-1 there are intrinsic limits to the magnetic performance of hard magnetic alloys. Equation 1-2 shows that the remanence B_r is limited by the magnetic polarization of the magnetic phase. The $\mu_o M_s$ value for the 2-14-1 phase is 1.61 T and the $(\mu_o M_s^{2)}/4$ is 516 kJ/m^3, which represents the upper limit on the $(BH)_{max}$ energy product as shown by Eq. 1-4. Equation 1-3 shows that the coercivity H_c is limited by the saturation magnetization M_s which is 1.28 (MA/m) for the 2-14-1 phase. The magnetic properties of actual production magnets deviate significantly from the theoretical limitations. The goal of current research is to close the gap between the actual magnetic performance of Nd-Fe-B alloys and the intrinsic limitations predicted by theory. Optimizing remanence and coercivity are completely different problems, and their solutions often run contrary to one another.

1.3.1 Optimizing coercivity

The magnetic coercivity of a magnet, H_c, is a measure of the magnet's ability to resist the reordering affects of an applied magnetic field. A magnetic field applied in the opposite direction to the resultant magnetization of the ferromagnetic material will reverse the magnet's field direction by nucleating and growing domains that conform to the new magnetic field direction. Morphological and intrinsic characteristics of a ferromagnetic material that prevent either the nucleation or growth of reverse domains increase the material's coercivity.

Reverse domains nucleate at defects within the magnetic structure where the energy to rotate the magnetic spin alignment is the lowest. Rough surfaces are good examples of energetically favorable reverse domain nucleation sites, because of the presence of high energy defects. Inherent in hard magnetic

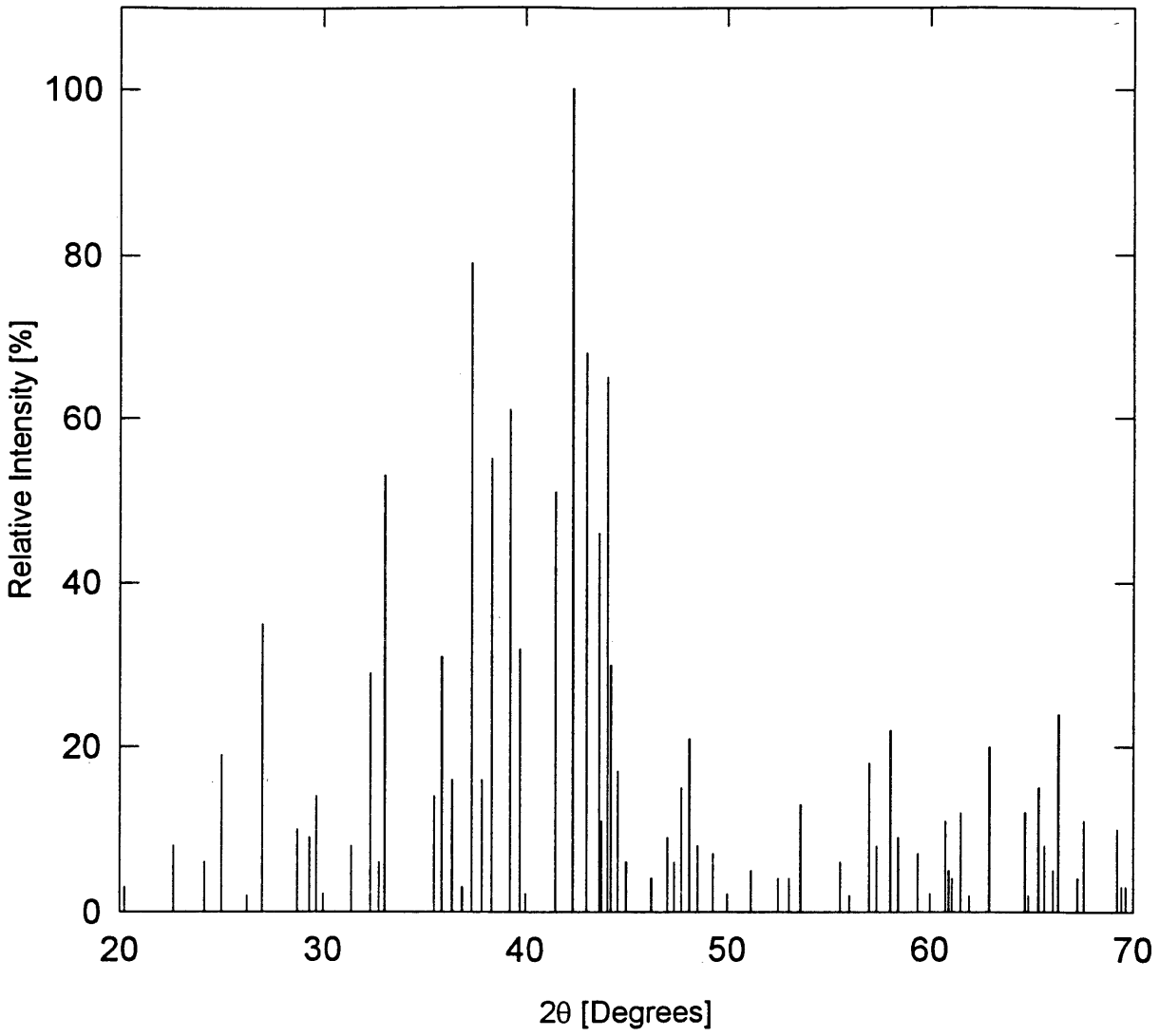

Figure 1-5: X-ray diffraction pattern for pure randomly oriented 2-14-1, assuming Cu-$K_{\alpha 1}$ radiation.

materials is atomic level magnetocrystalline anisotropy. Electronic spin interactions between the 3d and 4f electrons in the alloy produce easy and hard magnetization directions in the unit cell. The electronic level anisotropy interferes with the nucleation of reverse domains, and therefore the greater the magnetocrystalline anisotropy the greater the coercivity. Alloying additions that increase the magnetocrystalline anisotropy increase the coercivity.

There is another type of magnet anisotropy that is generated in the crystal structure. The 2-14-1 macro-crystals tend to crystallize as elongated precipitates, elongated in the c-axis. There is an easy magnetization direction in an elongated 2-14-1 precipitate that would tend to correspond to the c-axis of the individual unit cells. Therefore, there is a precipitate shape anisotropy. This type of anisotropy enhances coercivity. If a reverse magnetic field is applied to a 2-14-1 crystal that opposes the two natural magnetization directions (c vs -c), then the 2-14-1 crystal will resist magnetic realignment and therefore resist the nucleation of reverse domains. Additions that enhance the shape anisotropy, enhance the coercivity of the microstructure.

As a single atomic spin is reversed, it has a direct effect on its neighbors because of the exchange coupling that is inherent to ferromagnetic materials. The perturbation that a single spin reorientation causes will decay over a characteristic scale called the exchange length l_{ex}, which is about 3 nm for ferromagnetic iron or cobalt based alloys [2]. In hard ferromagnetic materials, l_{ex} is approximately the same size as a domain wall width (Bloch wall width) δ_W. "There is another important length parameter known as the single-domain particle size, d_c, the size of the largest crystallite for which the cost of creating a domain wall in equilibrium exceeds the gain in magnetostatic energy" [2]. It seems obvious that single domain particles would resist reverse domain nucleation better than multiple domain particles in which reverse domains do not have to be nucleated. Therefore, it would seem that reducing the grainsize of a

ferromagnetic material to a nanoscale structure so that all the crystallites would be single domain particles would enhance coercivity. However, if the size of the particles becomes fine enough that the l_{ex} approximates the grainsize, then one spin reversal can completely reverse the entire domain structure by exchange interactions, and coercivity is completely lost.

As stated before, anything that prevents the nucleation or growth of reverse domains increases coercivity. Domain walls (Bloch walls) move like grain boundaries. Inclusions and particle dispersions can inhibit Bloch wall motion in the same manner that they inhibit grain boundary motion. Figure 1-6

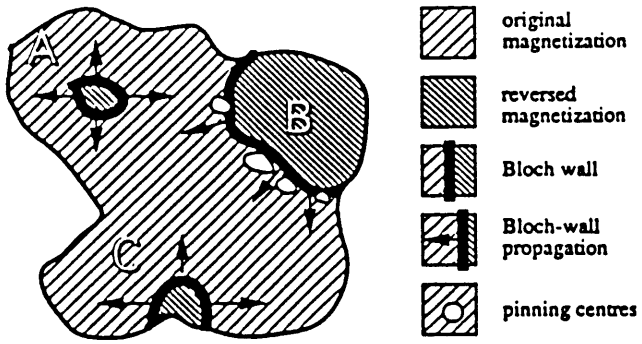

Figure 1-6: Figure demonstrating the formation of reverse domains. Point A shows a reverse domain nucleated at an internal defect or from a spontaneous thermal fluctuation. Point B shows how Bloch walls can be trapped by pinning centers. Point C is a reverse domain that nucleated at a rough surface [2].

demonstrates how pinning centers can inhibit reverse domain growth and therefore increase the material's coercivity.

Current research has focused on producing nanoscale composite microstructures of 2-14-1 and a soft magnetic phase like α-Fe by melt-spinning

molten Nd-Fe-B alloy into an amorphous precursor, and crystallizing a specific microstructure through careful heat-treating [4,5,6,7,8]. Soft magnetic materials have poor coercivity by definition. Therefore, an increasing phase fraction of soft magnetic material in a magnetic composite reduces the overall coercivity of the composite. However, if the grainsize of the system is reduced so that the exchange length of the hard phase approximates the size of the soft magnetic grains, then the soft material can be exchange hardened by the 2-14-1, and coercivity is maintained [4].

1.3.2 Remanence optimization

There are several ways to optimize remanence. The remanence ratio is often noted in discussions of magnetic materials. The optimum microstructure for a uniaxial material like the 2-14-1 phase would be one in which the c-axes of all the crystallites were aligned parallel. "The remanence for a fully anisotropic texture could be as high as the spontaneous magnetization if the magnetic phase was fully dense" [2]. When there is any misorientation the local magnetization will tend to revert to the nearest c-direction. The ultimate in misorientation would be a isotropic magnet with a random distribution of crystallite orientations. Provided there are no reverse domains, the following equation defines the remanence to magnetic saturation ratio M_r/M_s [2]:

$$M_r/M_s = \int P(\Psi) \cos \Psi \, d\Psi \; / \; \int P(\Psi) \, d\Psi \qquad \textbf{[1.5]}$$

where:

$P(\Psi)$ = the texture of the distribution of crystallite orientations
Ψ = the angle between the c-axis and the magnetizing field

"When the distribution is completely isotropic, $P(\Psi) = \sin \Psi$ and the $M_r/M_s = 0.5$, which in turn would lead to a $(BH)_{max} < 0.25$ of the value obtainable in a fully oriented magnet of the same material" [2]. The crystallites grown from a fully amorphous matrix would tend to be isotropic.

Remanence can be enhanced above $M_r/M_s = 0.5$ for a single phase isotropic material in a nanometer scaled structure. If the grainsize is fine enough that exchange coupling across grain boundaries occurs, then the microstructure will experience enhanced remanence. For optimal enhanced remanence, the grain thickness must be small enough that the surrounding grains' exchange length l_{ex} encompasses the grain. Since the exchange length of the 2-14-1 phase is 4.2 nm [4], the 2-14-1 grain size including grain boundary would have to be on the order of 10 nm for complete enhanced remanence. The drawback to such a structure is a significant loss in coercivity, as explained before.

Remanence can also be enhanced by generating nanoscale composite materials of hard and soft magnetic phases. Soft magnetic phases typically show much higher magnetization polarizations than hard magnetic materials; for 2-14-1 the $\mu_o M_s = 1.6$ T while the $\mu_o M_s = 2.1$ -2.3 T in α-Fe and Fe-Co alloys [2]. If the hard phase is distributed with the soft phase in a microstructure with a fine enough grainsize that the soft phase can be hardened by exchange coupling with the hard phase, then an enhanced remanence above the optimal enhanced remanence for a single phase 2-14-1 microstructure could be generated. The soft phase would need to have a grainsize on the order of two times the exchange length l_{ex} of the hard phase or ~10 nm for a 2-14-1 microstructure. In addition, because the 2-14-1 grains are not exchange coupling directly, there is little loss in coercivity [5].

1.4 Purpose and Scope of Thesis Research

The goal of this research was to characterize the microstructure of various Nd-Fe-B rapidly quenched and annealed magnetic powders with Mössbauer spectroscopy and x-ray diffraction, and to correlate microstructural differences with magnetic properties. The as received powders had been melt-spun into highly amorphous flakes. This research is part of a larger effort to generate nano-structured $Nd_2Fe_{14}B$ powders for resin-bonded permanent magnets. The goal is to precipitate a nanoscale composite microstructure composed of a hard 2-14-1 phase and a soft magnetic phase through controlled heat-treating of an amorphous precursor. Optimally, the composite morphology would experience enhanced remanence by exchange coupling between soft and hard magnetic phases while maintaining coercivity. Refractory metal additions were made to the alloys in the hopes that a refractory metal boride matrix would precipitate to inhibit grain growth during heat-treatments. Increasing the composite's coercivity by domain wall pinning was anticipated as a possible secondary benefit of a refractory metal boride matrix.

Eight alloys with four different compositions were supplied by Rhodia for the study. The four nominal compositions studied are included in Table 1-2.

TABLE 1-2: Four Nominal Compositions (atomic%) of Alloys Examined in this Study

Alloy	(Nd + La)	(Fe + Co)	Refractory Metal		B
			Nb	Ti	
N28	12	82	0	0	6
U43, U44, U45, U54	11	77	2	0	10
U23	9	79	0	2	10
U57, U58	11	77	1	1	10

Note that titanium and/or niobium additions were made to 3 of the 4 compositions. The N28 composition was used as a control sample to determine if the refractory metal additions were the source of any grain size reduction. Figure 1-7 shows the positioning of the compositions examined in the Nd-Fe-B ternary diagram. All of the compositions lie in the iron rich corner of the

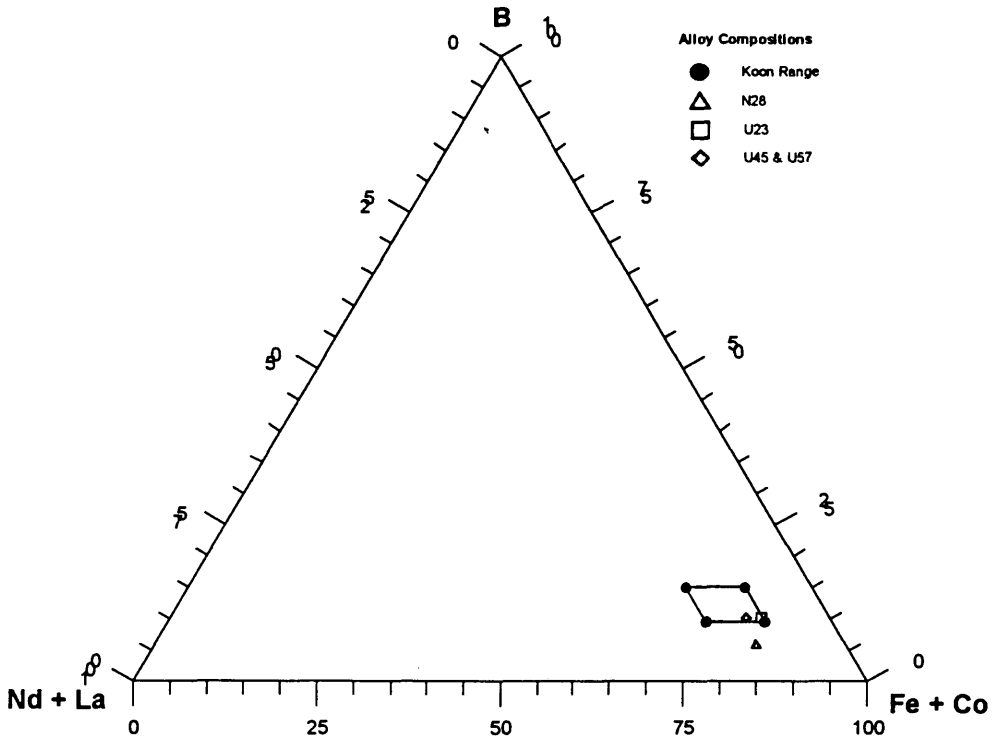

Figure 1-7: Ternary diagram of the Nd-Fe-B system showing compositions of alloys studied

Nd-Fe-B ternary diagram. Note that the only composition that lies outside the Koon patent range is the N28 composition, which is a Magnequench International MQP-B composition.

Heat-treating experiments were performed at the Colorado School of Mines in

which several different annealing conditions were used to generate different microstructural morphologies. The purpose of the study was to characterize the microstructure of the as-quenched and annealed powders with Mössbauer spectroscopy and x-ray diffraction. ^{57}Fe Mössbauer spectroscopy was used to determine the phase distribution of the powders. ^{57}Fe Mössbauer spectroscopy can be used to identify and quantify any iron-containing phase. Since all of the compositions examined were iron rich, it was assumed that most if not all of the phases precipitated would contain iron. A grain size measuring technique based on x-ray peak line broadening and the Scherrer equation, was developed in cooperation with a Rhodia laboratory in Paris, France. In addition, x-ray diffraction was used to identify any non iron-containing phases. Magnetic measurements were undertaken by a Rhodia laboratory in Cranbury, New Jersey. The current study began optimization of the magnetic performance of the four alloy compositions examined by characterizing microstructural differences between samples with x-ray diffraction and Mössbauer spectroscopy, and then correlating these results with the measured magnetic properties.

Chapter 2

BACKGROUND ON EXPERIMENTAL TECHNIQUES

2.1 The Mössbauer Effect

To understand the Mössbauer effect, several basic quantum physics concepts must be explored. First, quantum mechanics shows that like the electron orbitals in atoms, the atomic nucleus exists in specific allowed quantized energy states. There are several different modes to the nuclear energy levels. One mode is quantified by the number and type of nucleons present in the nucleus, and their interaction with the electron cloud. The thermal mode has to do with the binding energy associated with the valence electron binding to surrounding atoms. The atom can be thought of as a mass attached to the surrounding atoms by springs. In this analogy the atom becomes a harmonic oscillator. Like all harmonic oscillators, the atom will have specific allowed vibrational modes related to the formation of standing waves. The vibrational modes that the atom as a whole has are directly related to the atom's thermal energy. Because the nucleus comprises most of the mass of the atom, it can be thought of as the object exhibiting the quantized allowed thermal vibrational modes.

Second, like the electron, the nucleus can shift from one energy state to another by the absorption or emission of a photon. Nuclear energy states correspond to the gamma-ray band of the electromagnetic spectrum. A photon is a bundle or packet of a specific amount of electromagnetic energy that has no mass, but does have momentum. If a photon strikes the nucleus it can either

pass through unaffected or be absorbed. When a nucleus absorbs a photon it absorbs both the photon's energy and momentum, and jumps from its previous equilibrium energy level (ground state) to a new higher energy level. To return to its ground state the nucleus must re-emit another photon; these re-emitted photons are released in random directions. However, because photons have energy and momentum, both the absorption and re-emission of photons generates recoil in the nucleus. The absorption recoil is similar to when a bowling ball is dropped on a mattress, the mattress is deformed and vibrates the extra energy away. The emission recoil is similar to when a cannon is fired, the cannon recoils in the opposite direction of the cannon ball. Therefore, it would be expected that the energy of a nuclear re-emitted photon would be less than the energy level of an absorbed photon, by twice the amount of energy consumed in the nuclear recoil. In a solid, the nuclear recoil energy should manifest itself in a shift from one thermal vibrational mode to another.

The Mössbauer effect is the recoilless emission and absorption of a gamma ray photon. How is a recoilless emission possible? The best way to describe the Mössbauer effect is to examine a specific example. The recoil energy imparted to a free nucleus by a departing gamma ray is shown by basic conservation of energy and momentum as:

$$E_R = p_n^2/2M = (E_\gamma^2)/(2Mc^2) \qquad \textbf{[2.1]}$$

where:

E_R = recoil energy
p_n = momentum imparted to nucleus by emission
M = mass of nucleus
E_γ = energy of gamma ray

For the 14.4 keV gamma-ray from ^{57}Fe, the recoil energy given to the nucleus by

equation [2.1] is 0.002 eV. The smallest harmonic oscillation vibrational mode energy gap of a ^{57}Fe nucleus in Fe metal can be estimated by the Einstein or Debye energy of the nucleus, which is about 0.04 eV. This energy is more than an order of magnitude larger than the recoil energy imparted to the free nucleus by a 14.4 keV gamma ray. Since the recoil energy is insufficient to excite the nucleus to its next higher vibrational energy state, the gamma ray leaves the nucleus with the full 14.4 keV of energy. The recoil is not absorbed by the individual nucleus, but by the crystal lattice as a whole. Therefore the mass used in equation [2.1] is not the mass of the nucleus, but rather the mass of the entire crystal lattice, which drives the recoil energy to an infinitesimal amount. A direct analogy is a man throwing a baseball. Since the man is firmly planted on the ground, the recoil that the man experiences from throwing the baseball is transmitted to the Earth. When the baseball flies away, the entire Earth recoils, but the recoil is so insignificant that it can not be measured.

2.2 ^{57}Fe Mössbauer Spectroscopy

Mössbauer spectroscopy uses the Mössbauer effect to characterize materials. When a gamma ray beam containing a range of photon frequencies is directed at a sample, only the specific frequencies corresponding to nuclear transitions will be absorbed and re-emitted in random directions. Normally, if a detector is set to intercept a gamma ray beam, it will detect all of the frequencies of the beam with an equal probability. However, if some of the frequencies are being absorbed due to the Mössbauer effect and re-emitted in random directions, then these particular frequencies will show lower than normal photon counts thereby generating an absorption spectrum. Therefore, by detecting a spectrum of incoming frequencies on the other side of a target, there will be a statistical decrease in photon counts in the photon frequencies being absorbed during the

Mössbauer effect. This means that the absorption spectrum produced can act like a fingerprint and be used to characterize and quantify the phases present in a sample.

Although the Mössbauer effect exists in many elements, the most common and useful is iron. The key to using Mössbauer spectroscopy is generating photons of exactly the right frequencies to be absorbed in a sample. Normally you need a nucleus of exactly the same energy state to emit a photon that can be later absorbed by the nucleus that you are trying to detect. There is a man-made isotope of cobalt ^{57}Co that undergoes electron capture radioactive decay (E.C.) to a excited isotope of iron, ^{57}Fe. Figure 2-1 shows the decay scheme for ^{57}Co. The excited ^{57}Fe nucleus then relaxes to its equilibrium state by emitting

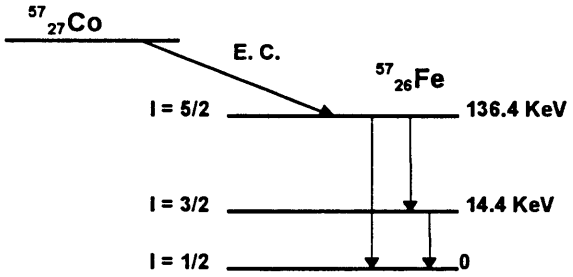

Figure 2-1: Decay scheme of ^{57}Co to ^{57}Fe (I = spin quantum number).

gamma-ray photons. The 14.4 keV gamma ray photon emitted from the excited ^{57}Fe source can then be absorbed, via the Mössbauer effect, by the ^{57}Fe nuclei within a sample. ^{57}Fe is one of the four stable isotopes of iron, and constitutes 2.14% of the total iron on earth [9]. Therefore, by the laws of isotope distribution,

on average 2.14 out of every 100 iron atoms within any sample will be ^{57}Fe atoms. To generate a range of gamma ray photon frequencies being emitted from the radioactive ^{57}Co source, the source is moved back and forth with constant acceleration (positive and negative). This motion causes a Doppler shift in the frequencies of emitted photons, thus generating a spectrum of gamma ray frequencies to be absorbed by the sample being analyzed. The end result is that Mössbauer spectroscopy can be used to detect and quantify any iron-containing phase within a sample. A precise explanation of the method of phase quantification by Mössbauer spectroscopy is included in Appendix I, which came from private communications with Dr. Williamson [10]. Since the Nd-Fe-B-Co alloy compositions being examined are all greater than 75 atomic percent iron, every phase present will likely contain iron. Therefore, Mössbauer spectroscopy could be a useful tool in characterizing this type of rare earth alloy.

2.3 Mössbauer Spectra Differentiation

Mössbauer absorption spectroscopy can only be useful as a characterization tool if it can differentiate between different phases containing a Mössbauer element. There are three electron-nuclear hyperfine interactions that act to clearly differentiate Mössbauer fingerprints. In all three hyperfine interactions there is a nuclear differentiation that is amplified by electron cloud interaction with the nucleus to produce a noticeable Mössbauer spectrum change.

The first electron-nuclear hyperfine interaction is the electric monopole, which results in the isomer shift. The number and type of nucleons determines the elemental isomer nuclear size. However, the size of the nuclear radius is not a constant for a given elemental isotope. The size and shape of the nucleus will change depending on the nuclear energy states. As the size of the nucleus changes, the quantized allowed nuclear energy levels shift due to the

electrostatic interactions between the electron cloud and the nucleus. Nuclear energy level shifts imply that different Doppler velocities will need to be imparted to the gamma-rays to enable maximum absorption by the Mössbauer effect. Therefore, the position of the Mössbauer absorption line on a Doppler velocity spectrum shifts as a result of this electric monopole interaction. The valence state, coordination number, type, positions, and bonding types of surrounding atoms directly affect the electron distribution of an atom, which directly affects the electron cloud that interacts with the nucleus. Therefore the phase that an atom finds itself in will determine the amount of isomer shift in a Mössbauer absorption spectrum.

"The second electron-nuclear interaction is the electric quadrupole which generates the quadrupole splitting observed in iron spectra as a typical doublet line pattern" [11]. Asymmetry in the electron charge distribution of an atom generates an electric field gradient, which interacts with an asymmetry in the nuclear shape. "Any nuclear state with a spin I >1/2 has a quadrupole moment, Q, and this can align itself either with or across an electric field gradient, q" [12]. A non-spherical nucleus within an asymmetrical electron cloud has a quadrupole moment, creating two possible energy states. Figure 2-2 , taken from reference [12], shows the separation of the higher-level energy state of ^{57}Fe into two states due to this interaction. The amount of separation between the two energy states, Δ, is determined by the following equation:

$$\Delta = (\text{constant})\ Q\ q \qquad \textbf{[2.2]}$$

where:

Q = the quadrupole moment of the 14.4 keV excited state of ^{57}Fe
q = electric field gradient created by a non-spherical electron cloud

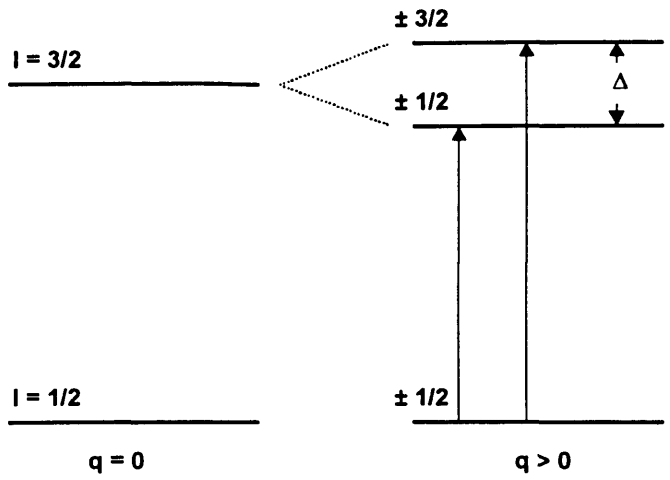

Figure 2-2: Quadrupole splitting of nuclear energy levels.

The two energy states are reflected in two different absorption lines in a Mössbauer absorption spectrum. The amount of asymmetry in the electron cloud directly effects the amount of separation between the two absorption lines. The amount of atomic electron cloud asymmetry is a function of the coordination number and type surrounding atoms and the bonding-type formed with surrounding atoms. Non-cubic crystal structures or local atomic sites tend to generate asymmetrical electron distributions.

The third electron-nuclear interaction is the nuclear magnetic dipole, which generates hyperfine Zeeman splitting of the nuclear energy levels in a magnetic field. "Each level of spin quantum number I will split into (2I +1) sublevels, with energies given by the following equation" [12]:

$$E = -\mu Hm/I \qquad [2.3]$$

where:

E = energy level shift
μ = nuclear magnetic moment
H = hyperfine magnetic field
m = magnetic quantum number
I = total spin quantum number

Note that the allowed nuclear energy levels depend on both the nuclear magnetic moment and the magnetic field, H, which is generated at the nucleus by the electron cloud. By the laws of quantum mechanics, the change in the quantum number m, Δm, is only allowed to be 0, +1, or -1. Therefore, there are six allowed energy transitions. Figure 2-3, taken from reference [12], shows the allowed hyperfine splitting of nuclear energy levels for ^{57}Fe. Note that Figure 2-3

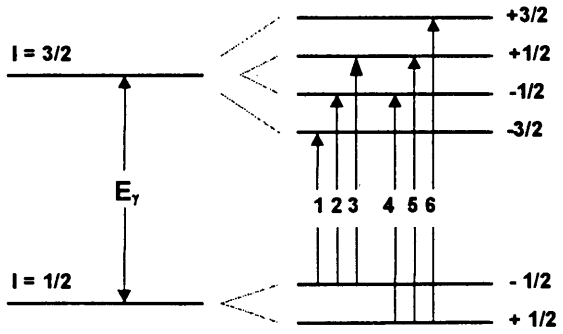

Figure 2-3: Hyperfine splitting of nuclear energy levels in a magnetic field, H.

shows that the single energy level transition is separated into six energy level transitions by the Zeeman splitting. The six energy transitions are represented

by a splitting of the single Mössbauer absorption line into six separate ^{57}Fe lines for magnetic compounds of iron containing a unique crystallographic iron site.

There is another fundamental effect that acts to differentiate Mössbauer spectra. Mössbauer spectra absorption lines have an intrinsic line width associated with the uncertainty associated with nuclear energy states. Like the uncertainty in finding the exact location of an electron, the nuclear energy states have an uncertainty defined by the Heisenberg uncertainty principle which states:

$$\Delta T \, \Delta E = h/2\pi \qquad \textbf{[2.4]}$$

where:

ΔT = the lifetime of excited state
ΔE = the uncertainty of the energy level
h = Planck's constant = 4.135669×10^{-15} eV · s

Since the lifetime of the 14.4 keV ^{57}Fe nuclear excited state is 141 ns, Equation [2.4] predicts that the uncertainty in the energy level will be 4.67×10^{-9} eV. The energy level uncertainty defines the intrinsic line width of the absorption spectra (twice this uncertainty due to convolution of emission and absorption lines), and therefore the line width would be 0.194 mm/s on a Doppler velocity scale. This represents the minimum possible experimental line width. Typical values are somewhat larger (~0.3 mm/s) due to unavoidable sample and equipment effects [10].

2.4 Nd-Fe-B Mössbauer Spectra

Because the magnetic alloys of Nd-Fe-B all reside in the iron-rich corner of the Nd-Fe-B ternary diagram (Figure 1-7), most if not all of the phases precipitated in this system will contain iron, making ^{57}Fe Mössbauer spectroscopy an ideal tool for phase identification and quantification. However, the Mössbauer spectra generated by the primary phases in this system are extremely complex. The active hard magnetic phase in the system, the tetragonal $Nd_2Fe_{14}B$ (2-14-1) phase, has six different crystallographic Fe sites (Figure1-4). Each of the six Fe sites in the 2-14-1 phase has a different coordination number, type, and distribution of surrounding atoms. Therefore, each of the six sites will experience different Mössbauer absorption line splittings and shifts due to the three types of electron-nuclear hyperfine interactions. Each site will have a different isomer shift, but since all six iron sites are magnetic, they will all experience the six line ^{57}Fe Zeeman splitting. However, each site will have a different value of H. The quadruple splitting will be non-zero and different at each of the non-cubic sites and will be combined with the six line Zeeman splitting to make each six-line pattern asymmetric. Therefore, the single phase 2-14-1 generates six asymmetrical six-line Mössbauer absorption patterns, for a total pattern of 36 lines.

An asymmetrical 36-line pattern is complicated enough, however the 2-14-1 phase is not the only phase seen in this system. In each of the samples examined in the study at least two other iron-containing phases were detected. α-Fe was detected in several of the Mössbauer spectra. Like all iron-containing phases (that are not identical to the ^{57}Fe source phase), α-Fe experiences an isomer shift. However, the α-Fe phase is cubic so it does not experience quadrupole splitting. α-Fe is magnetic and every Fe site is identical. Therefore, it exhibits a single Zeeman symmetric split six-line pattern. Its isomer shift is

defined as zero on the Doppler velocity scale since it is commonly used as the reference absorber for defining the velocity calibration.

The $NdFe_4B_4$ (1-4-4) phase was also commonly detected in this alloy system. In addition to the isomer shift, the tetragonal 1-4-4 phase experiences quadrupole splitting. However, the 1-4-4 phase is not magnetic but instead paramagnetic, and so it does not experience Zeeman splitting into a six line pattern. Therefore, the Mössbauer pattern for the 1-4-4 phase consists of a two-line ^{57}Fe absorption pattern due to the quadrupole splitting.

The as-quenched samples were mostly amorphous and almost all of the annealed samples examined contained a fraction of either retained amorphous phase or residual disordered grain boundary phase. In either case, this phase does not have a long-range ordered crystal structure, and so therefore there is a large spectrum of possible ^{57}Fe sites. This phase has been identified as being soft magnetic. A symmetric, broad Zeeman six-line pattern of absorption lines was used to fit this amorphous-like phase.

The Fe_3B phase was detected in a few of the Mössbauer patterns. Since Fe_3B has a body-centered tetragonal crystal structure with three non-equivalent Fe sites Fe_I (8g), Fe_{II} (8g), and Fe_{III} (8g) at the vertices of a trigonal prism [13]. Each site experiences a different isomer shift. Because the sites are non-cubic, all three Fe sites in the Fe_3B phase experience a different degree of quadrupole splitting. In addition, the Fe_3B is a soft magnetic material and therefore, the three Fe sites also experience Zeeman splitting. Fe_3B has a complicated 18-line Mössbauer absorption pattern.

Even the simplest Mössbauer spectra generated in the study of this system contains more than 42 separate absorption lines, each with an inherent line width, superimposed on one another. It would seem that accurate phase identification would be almost impossible. However, like with x-ray diffraction tables of thousands of known crystal structures, there are published parameters

for the Mössbauer patterns of many known phases. The published values can be used as a baseline to begin quantitative analysis. Table 2-1 shows some published Mössbauer parameters for the five phases discussed, taken from the five sources [14[a], 15[b], 16[c], present work [d], 13[e]].

TABLE 2-1: Mössbauer Hyperfine Parameters and Relative Site Populations for 5 Phases Examined.

Phase	Fe-Site	H (T)	δ (mm/s)	Δ (mm/s)	Ref.
2-14-1	16k1	28.6	-0.045	0.25	a
	16k2	30.7	-0.116	0.14	a
	8j1	26.5	-0.126	0.16	a
	8j2	34.3	0.081	0.62	a
	4c	25.1	-0.037	0.03	a
	4e	28.8	0.122	-0.47	a
α-Fe		32.95	0	0	b
1-4-4		0	0.02	0.55	c
a-Nd-Fe-B		24.6	-0.065	0	d
Fe_3B	Fe_I (8g)	28.43	-0.05	-0.01	e
	Fe_{II} (8g)	26.45	-0.12	0.04	e
	Fe_{III} (8g)	22.12	-0.03	0.02	e

2.5 X-ray Diffraction

X-ray diffraction by regularly spaced solid crystal structures is a wave interference phenomenon that relies on electromagnetic scattering and wave phase relations. The wavelengths of x-rays (1-2 Å) are similar to the interatomic distances of atoms in solid crystals. Therefore, such distances can be resolved. The atoms in a crystal will scatter the incident beam of x-ray photons in all directions. However, because of the repetitive planar nature of solid crystal

structures, some of the scattered waves will exhibit constructive interference to form strong diffracted beams. "A diffracted beam may be defined as a beam composed of a large number of scattered rays mutually reinforcing one another" [17]. Only the scattered waves that obey the following Bragg law will form diffracted beams:

$$n\lambda = 2d \sin\theta \qquad \textbf{[2.5]}$$

where:

n = order of diffraction
λ = wavelength of incident gamma ray photons
d = interplanar spacing
θ = angle of incidence of x-ray photons (angle between the flat sample surface and the incident x-ray beam)

Note that the interplanar spacing of the scattering atoms, d, is the phase identifying factor in the Bragg law. Because the types of diffracting planes, and the spacing between diffracting planes is dependent on the crystal structure, they will vary from phase to phase. The types of crystal structure planes are usually labeled by their Miller indices (a good explanation of Miller indices can be found in reference [17]). The relative intensities of the various diffracted beams depend on many factors including interference within the unit cell, and the degree of randomness of the sample in a powder form. The diffraction pattern generated by an incident beam of x-rays can be used as a fingerprint to characterize the phases present in a given target sample.

There are several different types of x-ray diffraction. In this study, a constant beam of x-rays from a Cu source was scattered off a powder sample in the symmetric Bragg-Brentano geometry. A x-ray detector was positioned to intercept the diffracted beam after it had passed through a graphite crystal

monochromater to eliminate $Cu_{K\text{-}\beta}$ x-rays. The detector is moved in an arc so that a range of different diffraction angles is intercepted. The detector counts the number of x-ray photons that intercept its path in a given time frame and at a specific angle. In this way a diffraction pattern is generated by comparing the number of photonic counts at a given diffraction angle.

2.6 Line Broadening and the Scherrer Equation

The x-ray diffraction (XRD) patterns generated are plotted as x-ray counts per second versus 2θ (twice the Bragg angle). Figure 1-5, presented earlier, shows the diffraction pattern for the pure $Nd_2Fe_{14}B$ phase; this pattern was artificially generated and represents only the peak positions and intensities, without any peak widths. Figure 2-4 shows an actual XRD pattern for a well-crystallized $Nd_2Fe_{14}B$ sample. Notice that the peaks in real XRD patterns have a finite width over a small range of diffraction angles. Remember that only the scattered waves that obey the Bragg law will be diffracted in phase and experience constructive interference. The scattered waves that diffract on angles and planes that do not obey the Bragg law will have different path lengths, will be out of phase, and therefore will annihilate one another by destructive interference. In a perfect crystal of infinite thickness, there are an infinite number of planes that will contribute to the destructive interference and the scattered rays from all the non-Bragg planes will sum to zero. However, real crystals are not infinite, and therefore, there is a range of incident rays that make Bragg angles only slightly different from the ideal angle and the destructive interference is incomplete [17]. Therefore diffraction peaks have a range of diffraction angles that do not experience complete destructive interference. This range is called the peak width. The size of the diffracting crystal determines the number of diffraction planes, which determines the degree of successful destructive interference, and

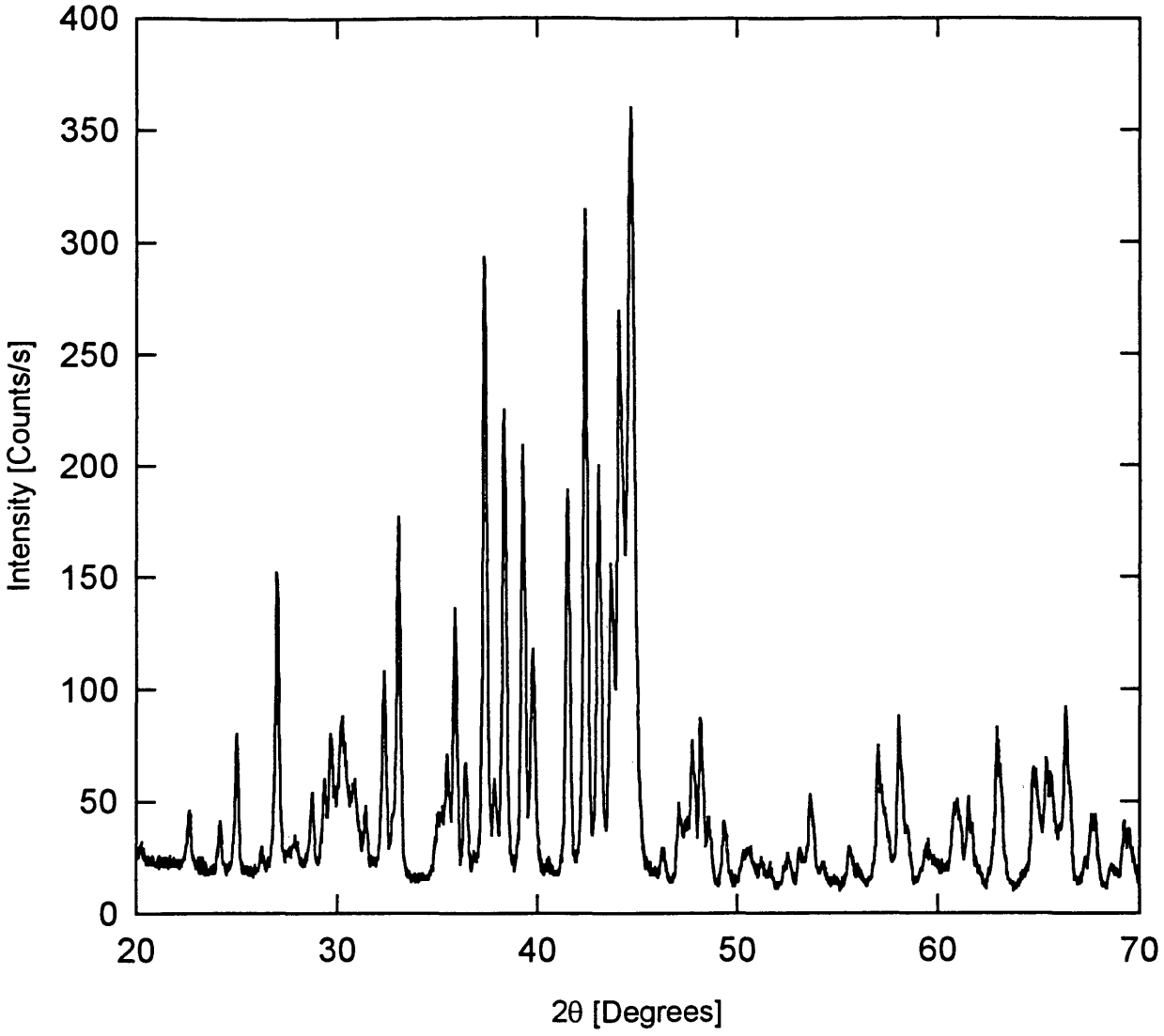

Figure 2-4: X-ray diffraction pattern for N28 sample annealed for 60 min at 750°C.

therefore, the peak widths. As the crystal thickness is reduced the peak width increases. The Scherrer equation defines the relationship between the crystal thickness (actually the crystal depth in the vertical direction perpendicular to the horizontal plane of the aluminum alloy powder holder) and the peak width (breadth):

$$t = \frac{0.9\,\lambda}{B\cos(\theta_B)} \qquad \textbf{[2.6]}$$

where:

t = particle thickness (grainsize)
λ = x-ray wavelength
B = peak broadening measured at half-maximum intensity
θ_B = expected peak Bragg angle

When does the effect of the Scherrer equation become noticeable in actual XRD patterns? "Suppose λ = 1.5 Å, d = 1.0 Å, and θ = 49°, then for a crystal 1 mm in diameter the breadth B, due to small crystal effect alone, would be about 2 x 10^{-7} radian (10^{-5} degrees), or too small to be observable. Such a crystal would contain some 10^7 parallel lattice planes of the spacing assumed. However, if the crystal were only 500 Å thick, it would contain only 500 planes, and the diffraction curve would be relatively broad, namely about 4 x 10^{-3} radian (0.2°), which is easily measurable" [17]. The peak broadening effect is only pronounced at crystal sizes finer than about 1000 Å (100 nm) [17].

The Scherrer equation can be applied to determine the grainsizes of fine crystallites with a particle size finer than 100 nm, by measuring the amount of peak broadening. The peak broadening of a sample with a very fine grainsize is most easily determined by the Warren method. The peak widths of a well crystallized standard with large grains is compared to the peak widths of a

sample with fine crystal line broadening by the following equation [17]:

$$B^2 = B^2_M - B^2_S \qquad \textbf{[2.7]}$$

where:

B = breadth used in the Scherrer equation
B_M = width at half maximum of the measured sample
B_S = width at half maximum of the standard sample

With this equation the line broadening generated by the finite resolution of the x-ray diffraction system is separated from the line broadening generated by crystal size refinement.

There is another source of peak broadening that can interfere with accurate particle size determination. First, non-uniform strain in the crystal lattice represented by dislocation slip can also generate line broadening. The dislocation slip breaks uniform crystals into sections with slightly different planar orientations and positioning. The misorientation can disturb the effectiveness of the destructive interference that removes peak broadening. It is hard to differentiate between the peak broadening generated by crystal size refinement and the peak broadening generated by a dislocation substructure. Therefore, any non-uniform strain present in a powder sample will decrease the accuracy of particle size measurements. Because the peak breadth(B) term appears in the denominator of the Scherrer equation, any additional factors that contribute to the amount of peak broadening will make the reported thickness (t) finer than the actual crystal thickness.

In real x-ray diffraction equipment is not possible to generate a truly monochromatic x-ray beam. In this study a copper target was used to generate the $Cu_{K\alpha}$ x-rays for the diffraction beam. $Cu_{K\alpha}$ x-rays are actually composed of

two closely spaced wavelengths $\lambda_{K\alpha-1}$ and $\lambda_{K\alpha-2}$. Because there are two different x-ray wavelengths, two different diffraction peaks are generated. Since the wavelengths are so close to one another, the peaks are indistinguishable at small diffraction angles, but are nonetheless a definite source of line broadening. Fortunately most modern XRD peak analysis software packages include a mathematical stripping program that removes the $Cu_{K\alpha-2}$ peaks from the XRD pattern.

Chapter 3

EXPERIMENTAL TECHNIQUES

3.1 Starting Material

The Nd-Fe-B-Co alloys arrived at the Colorado School of Mines in a mostly amorphous state. The alloys had been melt-spun and then crushed to a nearly uniform particle size of approximately -100 mesh (this is subsequently referred to as the 'head' material). The powder was used in the as-received condition in all annealing experiments.

3.2 Sample Preparation

Preparing powder samples for Mössbauer spectroscopy and x-ray diffraction was one of the most time consuming steps of the experimental procedure. After heat treating, the alloy powders had the same particle size as the as-received head samples, approximately -100 mesh. Therefore, both the head sample powders and the annealed sample powders were prepared in the same way for Mössbauer spectroscopy and x-ray diffraction. Optimal Mössbauer spectroscopy results and x-ray diffraction results are obtained if the particle size is -270 mesh or finer, because reducing the granularity generates more interaction between the gamma-ray and/or x-ray beams and the alloy powder [10]. Table 3-1 shows the results of a grinding study to determine if grinding to a finer particle size affected grainsize measurement. The grinding study indicated that sample variance in XRD measured grainsizes is reduced by grinding to a finer particle size. The reduced variance is directly due to improved peak intensities which

TABLE 3-1: Results of Grinding on XRD Grainsize Measurements

SAMPLE	MESH SIZE	OPENING (μm)	GRAINSIZE (nm)
U23-43-S1-270-1	-270	53	39.7 (+1.8, -2.7)
U23-43-S1-270-2	-270	53	39.1 (+0.5, -1.2)
U23-43-S1-270-3	-270	53	36.7 (+3.0, -2.7)
U23-43-S1-70-1	-70	212	37.8 (+3.6, -2.8)
U23-43-S1-70-2	-70	212	43.0 (+2.3, -1.8)
U23-43-S1-70-3	-70	212	38.5 (+1.6, -1.5)

generated more statistical clarity in the samples ground to -270 mesh. Therefore, the as-received and heat-treated powders had to be crushed to a finer particle size. However, the reactivity of the rare-earth elements causes Nd-Fe-B-Co powders to oxidize readily. The energy input to the system during crushing could catalyze surface oxidation. Therefore, the alloys were crushed in an inert argon atmosphere.

Early in the research effort, two energy intensive crushing techniques were attempted with poor results. First, a ring and puck shatterbox was used for powder crushing. Several problems quickly developed with the shatterbox technique. First, it was difficult to maintain an inert argon atmosphere in the shatterbox equipment, which led to surface oxidation of the finely crushed powders. Second, the high-energy motion of the shatterbox generated enough localized thermal energy to crystallize the powder particles. The shatterbox technique was abandoned in favor of a SPEX pulversizer WC ball mill. Because it was easier to maintain an argon atmosphere in the ball mill, less oxidation was experienced with the ball mill than the shatterbox. However, the ball mill was time intensive and also generated some crystallization in the amorphous powders.

All of the samples used in this study were prepared in the same manner. A glovebox was fitted with a vacuum pump and an argon feed line to produce an inert crushing atmosphere. To ensure representative sampling, a riffle-splitter was used to cut the as-received and heat-treated powders into 5 gram samples. An alumina mortar and pestle was used to grind the powders by hand. During a crushing run, a 5 gram powder sample was inserted into the glovebox's transfer chamber within the mortar, and a three-step evacuation and argon purge procedure was used to ensure no oxygen contamination. While crushing, a 270 mesh mini-sieve was used to periodically extract the powder already fine enough to pass. Crushing continued until approximately 80% (visual examination) passed the 270 mesh screen. The remaining 20% of the powder that did not pass the 270 mesh screen was then added to the portion that did, so that no sample material was lost.

At this point, sample preparation of the alloy powders was complete for loading into x-ray diffraction aluminum slides. However, a few more steps were required for Mössbauer sample preparation. The finely crushed powder was dispersed randomly in a binder and pressed into a wafer that acted as the absorber for the gamma-ray beam during Mössbauer analysis. Dr. Williamson had previously determined that a 200 mg mass of alloy powder produced the best signal-to-noise ratio in the Mössbauer analysis [18]. Therefore, 200 mg (weighed on a balance) of crushed powder was pulled from the 5 gram powder sample and mixed with 500 mg of powdered sugar with a "wigglebug" mixer in a plastic capsule. Powdered sugar acted as an inert binder. Since powdered sugar contains no Fe atoms (and therefore no ^{57}Fe), it is invisible to the Mössbauer gamma-ray beam. The alloy powder and powdered sugar mixture was pressed into a 2.54 cm diameter cylindrical wafer with a hand operated miniature press. The pressed wafer was then sealed in masking tape to maintain the integrity of the fragile wafer.

3.3 Mössbauer Analysis

Figure 3-1 is a schematic diagram of a typical Mössbauer spectrometer provided courtesy of Iron Carbide Holdings [19]. As discussed in chapter 2, the spectrometer detects the number of photon counts per second over a spectrum of gamma-ray frequencies generated by Doppler motion. The photon counts are accumulated in a series of 256 data channels, representing 256 Doppler velocities, in a multi-channel analyzer, controlled by a personal computer. The velocities that show the lowest photon counts correspond to the maximum absorption by the Mössbauer effect. Each iron-containing phase found in the sample has a specific spectrum of absorption lines that can be represented as the summation of a series of Lorentzian absorption curves, the typical shape for nuclear transitions. Figures 3-2, 3-3, and 3-4 are reference spectra for pure bcc-Fe, pure 2-14-1, and pure amorphous Nd-Fe-B respectively. The output spectrum is the superposition of all the resonance lines from all the Fe sites present in the indicated phase. Figure 3-5 is a reference spectrum showing various mixtures of 2-14-1 and amorphous Nd-Fe-B. The output spectrum can be decomposed into its component iron phase spectra for phase identification and quantification.

The generation of the end spectra is a statistical process. Since not every photon that could be absorbed via the Mössbauer effect strikes the interaction area of a nucleus, most of the photons, even at maximum absorption, pass through the absorber wafer to the detector. However, over a large number of photon counts, a statistical difference in photonic counts at the absorbing velocities compared to non-absorbing velocities will develop; the larger the total number of photon counts the better the statistical difference. The number of photon counts can be increased in two ways: with a stronger ^{57}Co radioactive source, or with a longer exposure time. The ^{57}Co source used during this

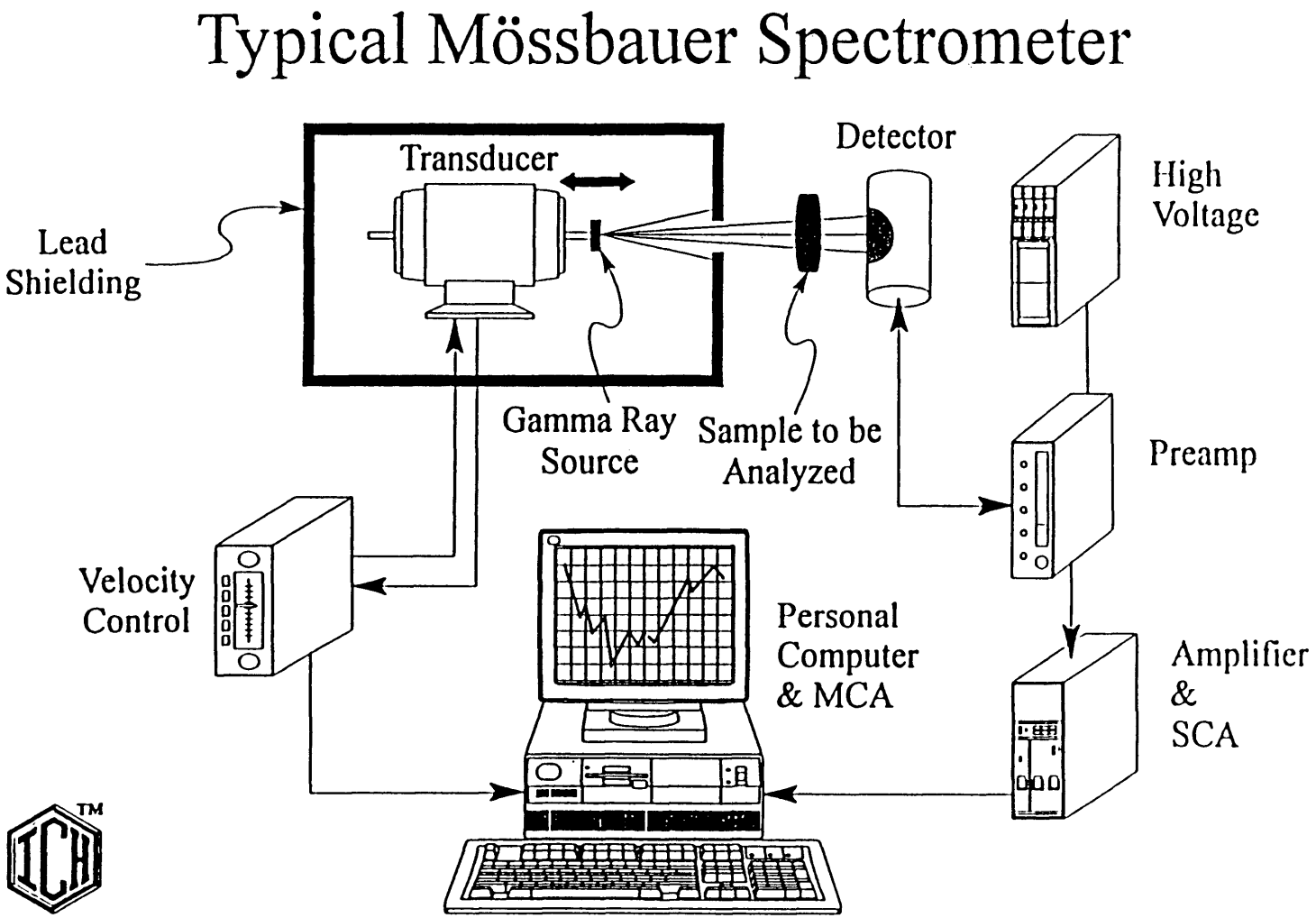

Figure 3-1: Schematic diagram of a typical industrial Mössbauer spectrometer [18].

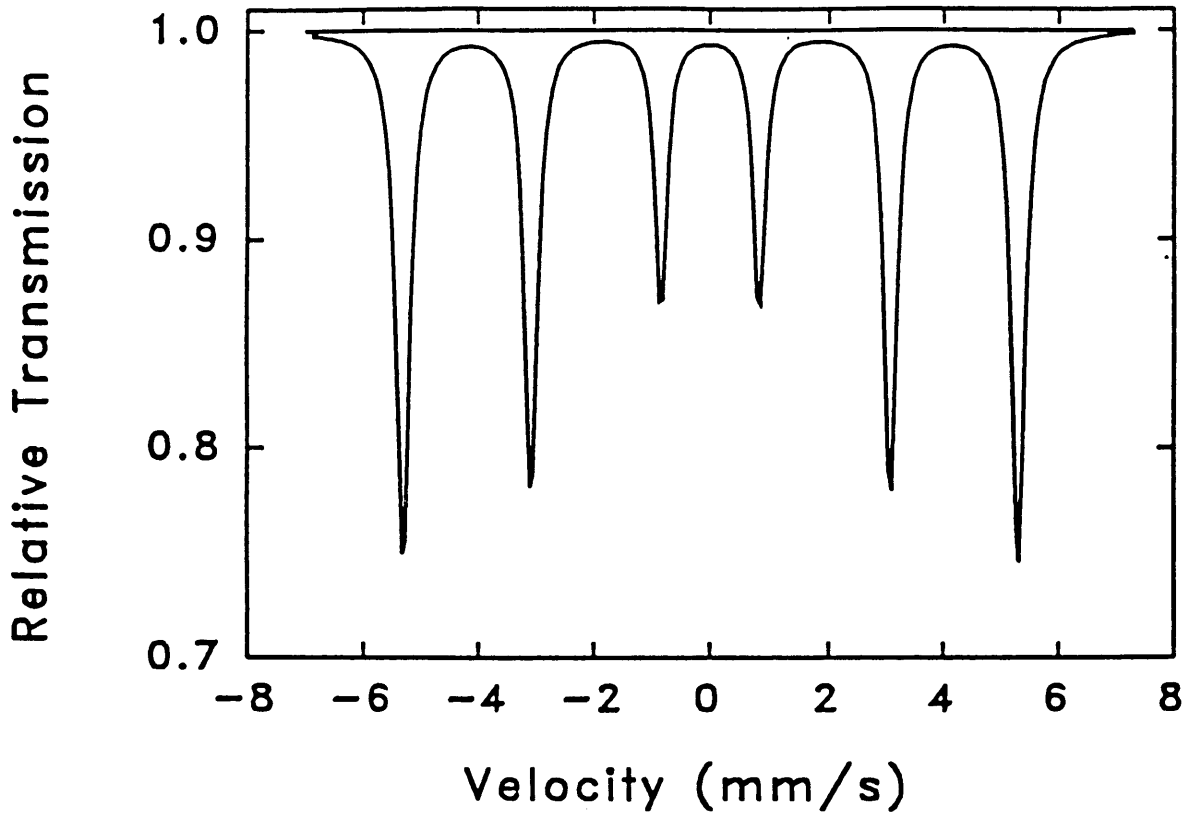

Figure 3-2: Mössbauer reference spectrum for pure bcc-Fe.

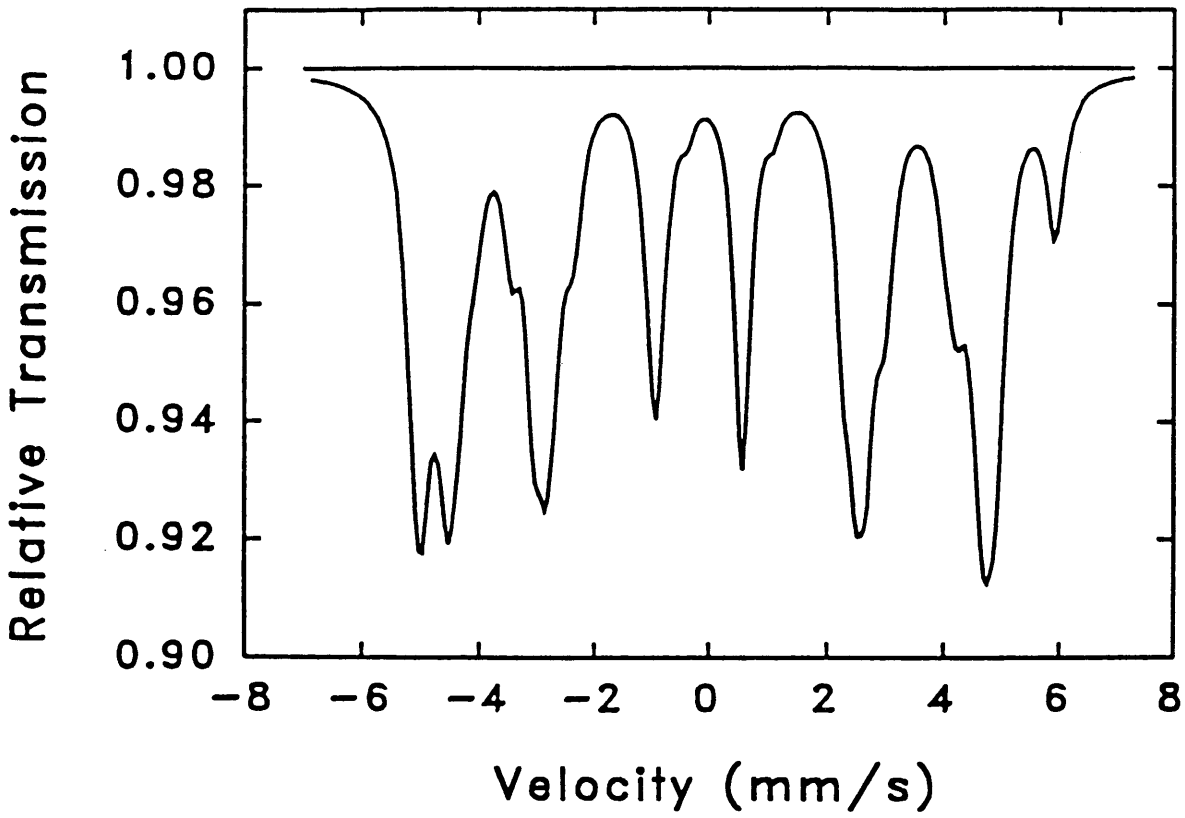

Figure 3-3: Mössbauer reference spectrum for pure 2-14-1 (based on Pringle et al parameters) [14].

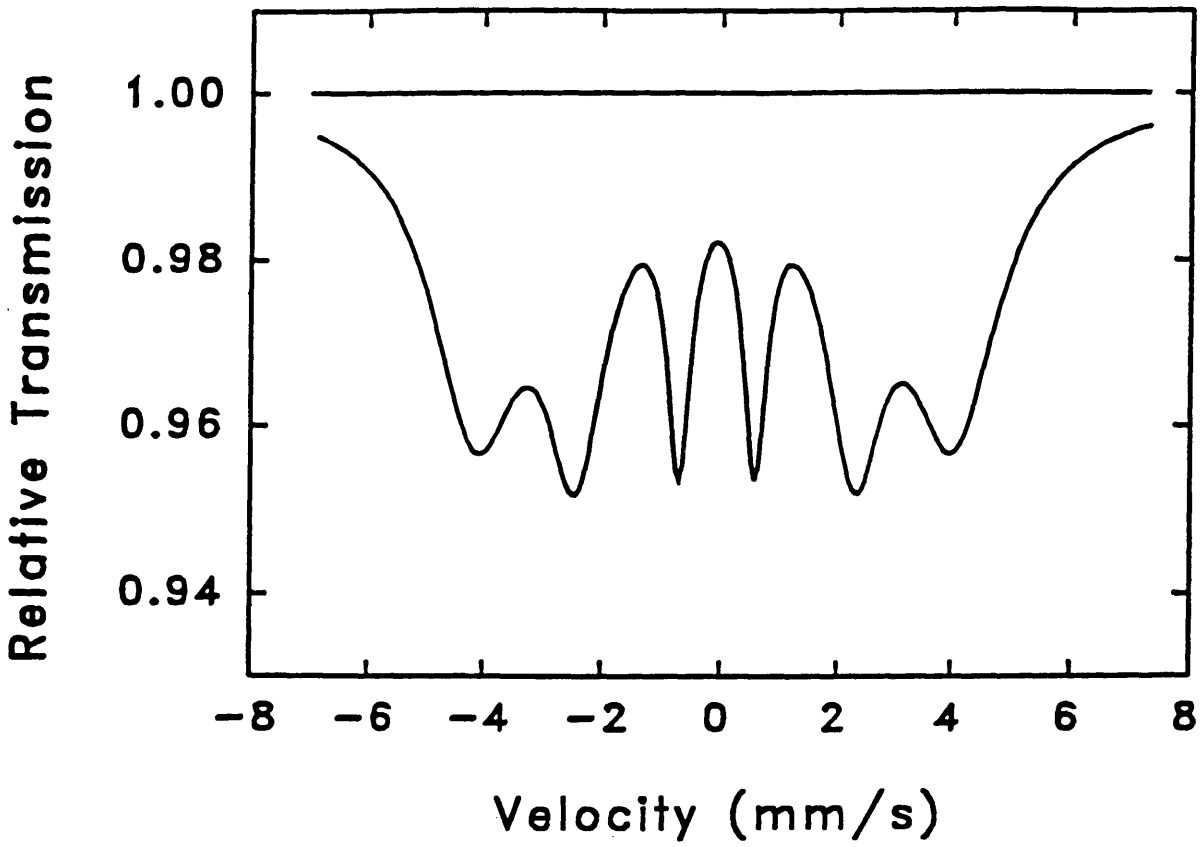

Figure 3-4: Mössbauer reference spectrum for amorphous phase based on N28 composition.

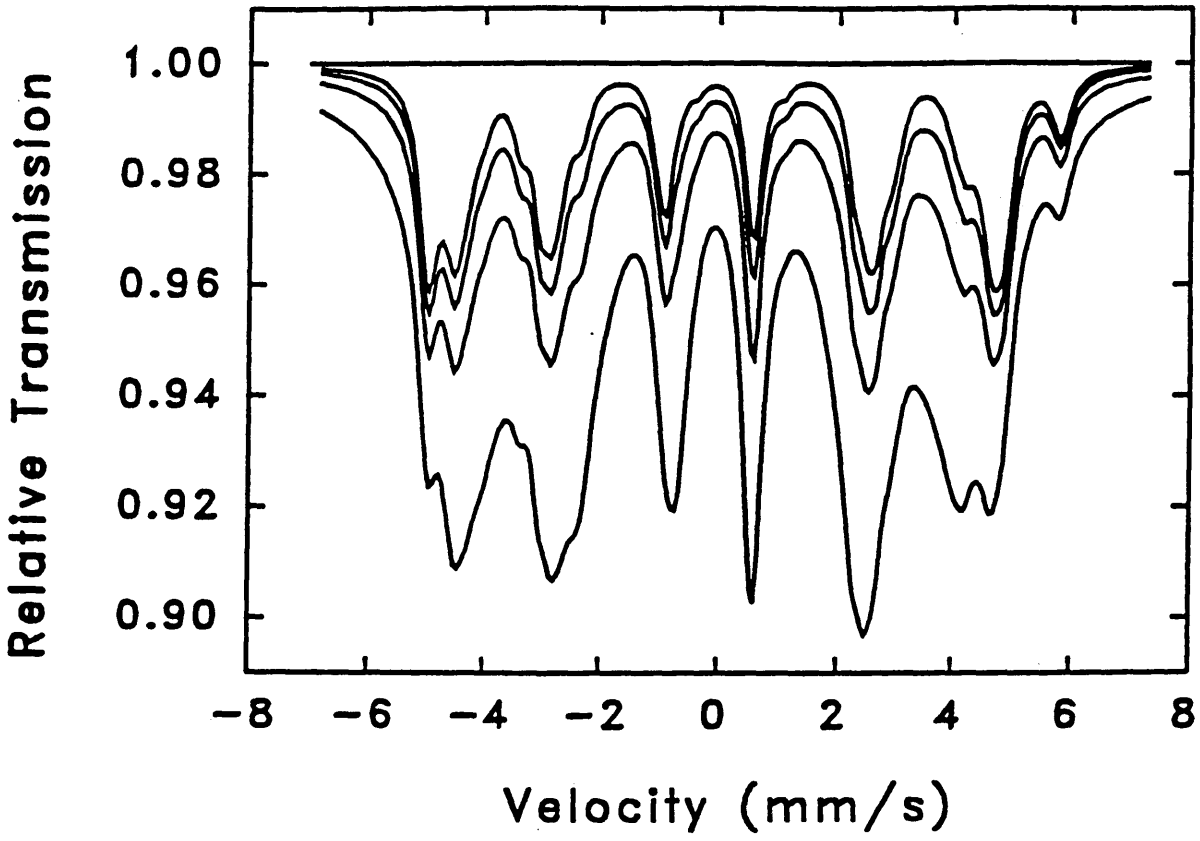

Figure 3-5: Reference spectrum showing theoretical mixtures of $Nd_2Fe_{14}B$ and amorphous Nd-Fe-B. Phase fractions used are $Nd_2Fe_{14}B$ + 0%, 25%, 50% and 75% amorphous Nd-Fe-B phase.

experimentation was relatively strong but high quality statistics were desired, so each sample wafer was measured for at least 12 hours.

A quantitative fraction of each iron-containing phase present can be determined mathematically, by calculating the relative area under each of the individual spectra (see Appendix I). Therefore, Mössbauer spectrometry not only detects all of the iron-containing phases present in the sample wafer, but it can be used to quantify the phase distribution of iron-containing phases present in the wafer. The relative phase fractions reported from the quantitative summation analysis are accurate to within 2 or 3 percentage points, based only on statistical errors in the deconvolution. However, the equations used in the quantitative analysis (Appendix I) are based on a major assumption. The equations assume that all of the iron-containing phases and each Fe site in a given phase have the same recoilless fraction. Not every ^{57}Fe site that could possibly recoillessly absorb a gamma-ray photon by the Mössbauer effect does so. The recoilless fraction is the fraction of ^{57}Fe sites that do experience Mössbauer absorption of incoming gamma rays. In actual practice, recoilless fraction values vary from about 0.5 to 0.8 at room temperature [Appendix I]. The recoilless fraction is a strong function of temperature. If the relative areas corresponding to different phases do not differ significantly between two temperature extremes, then based on Eq. 9 of Appendix I, the recoilless fractions are equal and therefore, Eq. 10, used in Appendix I, is valid. Table 3-2, taken from reference [20], shows the results of a Mössbauer analysis at liquid nitrogen temperatures to determine the reproducibility of Mössbauer phase fractions at two temperatures, 90°K and 298°K (room temperature) for an alloy sample with approximately the N28 composition. Table 3-2 indicates that the phase fractions do not change outside of statistical error ($\leq$ 3%) over a wide temperature range, and therefore the

TABLE 3-2: Evaluation of Effect of Sample Temperature on Mössbauer Spectra.

SAMPLE	SAMPLE TEMPERATURE (°K)	IRON DISTRIBUTION --- % (AS ONE OF THE FOLLOWING)		
		$Nd_2Fe_{14}B$	α-Fe	Nd-Fe-B
1013-100-SB	298	61	1	38
1013-100-SB	90	64	1	35

recoilless fractions in the 2-14-1 phase and the amorphous Nd-Fe-B phase are nearly equal. Nonetheless, the approximation that the recoilless fraction is the same in other phases present (1-4-4, Fe_3B, α-Fe) has not been validated. Therefore, the quantitative analysis could be in error when significant amounts of these other phases are present (which is not typical for most of the samples). Since the composition of the residual amorphous phase changes significantly during annealing, its recoilless fraction may change which could possibly lead to additional inaccuracy. However, due to the use of relative areas in the Mössbauer analysis, trends in the phase fractions seen among the various samples should be valid.

A software package, Normos, was used to deconvolute the spectral data files into summations of specific absorption spectra [21]. For each iron site present in each of the phases detected, the software allows a user to input a line of fitting parameters. The parameters are used to designate the line widths, the relative line depths expected for the Fe site of a specific phase, and the hyperfine interaction parameters (isomer shift, quadrupole splitting, magnetic field) expected for a given iron site within a specific phase (Table 2-1). As discussed in chapter 2, the 2-14-1 phase contains six separate distinguishable Fe sites, and

so using the Normos software package six different lines of parameters would be entered for the 2-14-1 phase. The program allows a user to fix parameters at specific known values, or allows the fitting program to numerically determine their optimal value. Using the user-specified parameters, the program then calculates a best fit, through minimization of the χ^2-parameter, for a specific Mössbauer spectrum. The output is a listing of the relative amounts of each calculated Fe site, and a data file containing the best-fit line and the actual data points. This data file can then be converted directly into a graphical spectrum using a graphics package (The Jandel Scientific program ***Sigma Plot*** was used for this work). Figure 3-6 shows a typical output Mössbauer spectrum.

3.4 X-ray Diffraction

A Rigaku model RU-200 x-ray diffractometer was used in this experimentation. The pre-crushed alloy powders were tightly packed into aluminum frames and loaded into the diffractometer. The Rigaku diffractometer used a copper source to produce a beam of $Cu_{K\alpha}$ x-rays (the $Cu_{K\beta}$ x-rays were filtered with a graphite crystal monochromater). The samples were scanned, in the symmetric Bragg-Brentano geometry, from 15 to 70° 2θ at a step size of 0.02°, and a count time of 10 seconds per step. The x-ray photon detector generated an electronic signal, which was converted to a data file of photonic counts per second at each value of 2θ.

The output data file was recorded as a single data column. Software produced by Materials Data, Inc. (MDI) was used to convert the single column data file to a MDI format. The converted data file was then loaded into a MDI program called ***JADE***. Using the ***JADE*** software, both the background noise, and the $Cu_{K\alpha-2}$ peaks were stripped from the original data file. A Microsoft

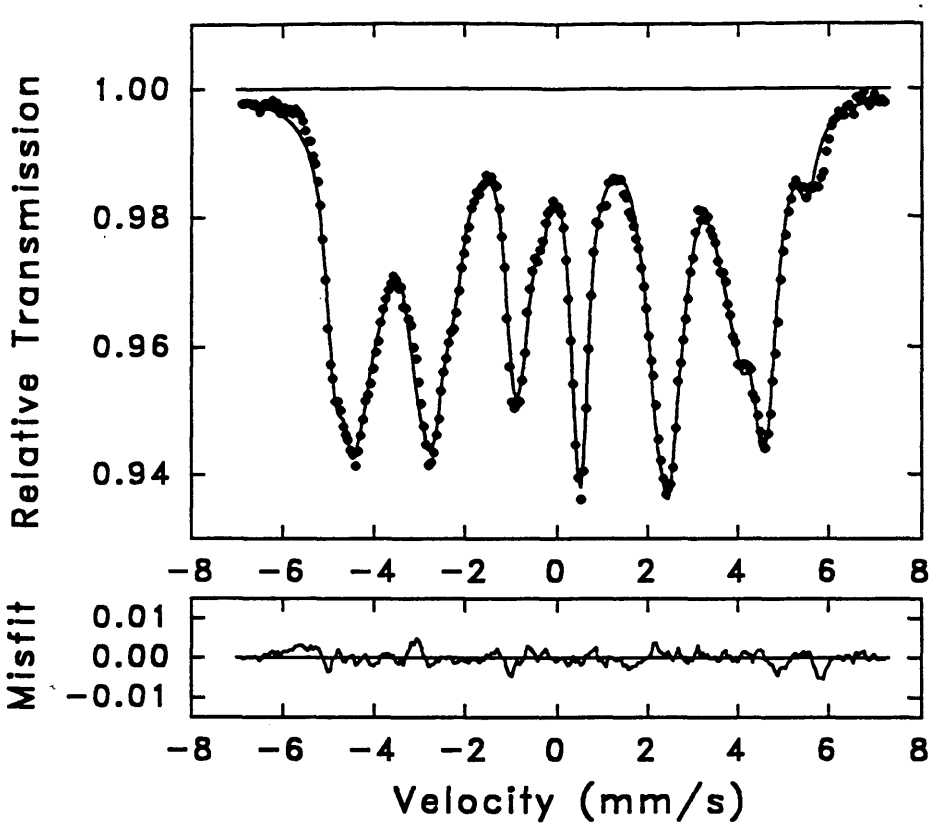

Figure 3-6: Mössbauer spectrum for U57-88-S2 sample annealed at 665°C for 3 minutes. Note: the misfit plot shows the deviation of the mathematically fit curve and the actual data points

EXCEL program was written and used to convert the ***JADE*** altered data file back to a single column of data. A Jandel Scientific program ***Peakfit*** was used for mathematical peak deconvolution and statistical analysis of the stripped data. The ***Peakfit*** software allowed separation of a large x-ray pattern into smaller peak subsections. A grouping of two or three peaks was separated and magnified into a sub-pattern of the original x-ray pattern. All of the peaks were fit with a superposition of Voigt functions in which the width parameters were forced to be shared by all of the peaks in the separated sub-pattern. ***Peakfit*** would then best fit the data by optimization of the r^2-parameter, and produce a file of standard statistical parameters to describe the peaks identified including the peak positions, widths at half maximum intensity, and parameter standard deviation.

3.5 Grainsize Measurements

A grainsize measuring technique was developed in cooperation between the Colorado School of Mines research team and a Rhodia laboratory in Paris. Dr. Valerie Archambault was the coordinator of the Rodia effort in France. The technique developed was based on the Scherrer equation as discussed in chapter 2. The two groups agreed upon procedural details, and six U23 samples were picked for the study (5 annealed samples and the head sample). Sample preparation was performed at the Colorado School of Mines and the crushed samples were split in two; half of the material was sent to Paris. Both research teams performed x-ray diffraction experiments on the same sample material using the same technique but different equipment. Finally, the results of the two teams were compared.

For the current discussion a quick review of some basic concepts previously discussed in chapter 2 may be helpful. The Scherrer equation (Eq. [2.6]) relies

on the line broadening of x-ray peaks generated in samples with crystallites less than 100 nm by incomplete interference of diffracted x-ray beams at angles that do not obey, but lie close to, the diffraction angles defined by the Bragg law (Eq. [2.5]). The B term that appears in the Scherrer equation is the measured peak broadening. The Warren method (Eq. [2.7]) is the standard method of calculating the Scherrer B term. The Warren method calculates the Scherrer equation B term based on the difference between the width at half-maximum of a x-ray peak in a well-crystallized standard and a sample in which line broadening is expected.

The National Institute of Standards and Technology (NIST) has developed crystal standard materials for line broadening calculations. There is another source of line broadening in x-ray diffraction patterns besides grain refinement. Non-uniform strain can cause line broadening in x-ray diffraction patterns. NIST standards are highly annealed to generate uniform grains with no compositional gradients or non-uniform strain, and grainsizes well in excess of the 100 nm limit to the line-broadening generated by grainsize refinement. A NIST lanthanum boride (LaB_6) standard was used as the standard, B_S term, for Eq. [2.7] calculations in this study.

A x-ray scan was performed on the NIST LaB_6 from 10 to 70° 2θ. ***Peakfit*** was used to mathematically deconvolute and statistically fit all of the peaks that appeared in the LaB_6 XRD pattern. The ***Peakfit*** software automatically measures the full peak width at half-maximum intensity (FWHM) as part of its statistical package. The LaB_6 peak widths at half-maximum intensity were then plotted as a function of the angle 2θ at which they appeared. Figure 3-7 shows the line width calibration plot for the LaB_6 standard. It should be noted that a 1° divergence slit was used in the XRD measurements of this study. The following polynomial trend line was then fit to the data points to develop a mathematical equation to describe the change in the LaB_6 widths at half maximum as a

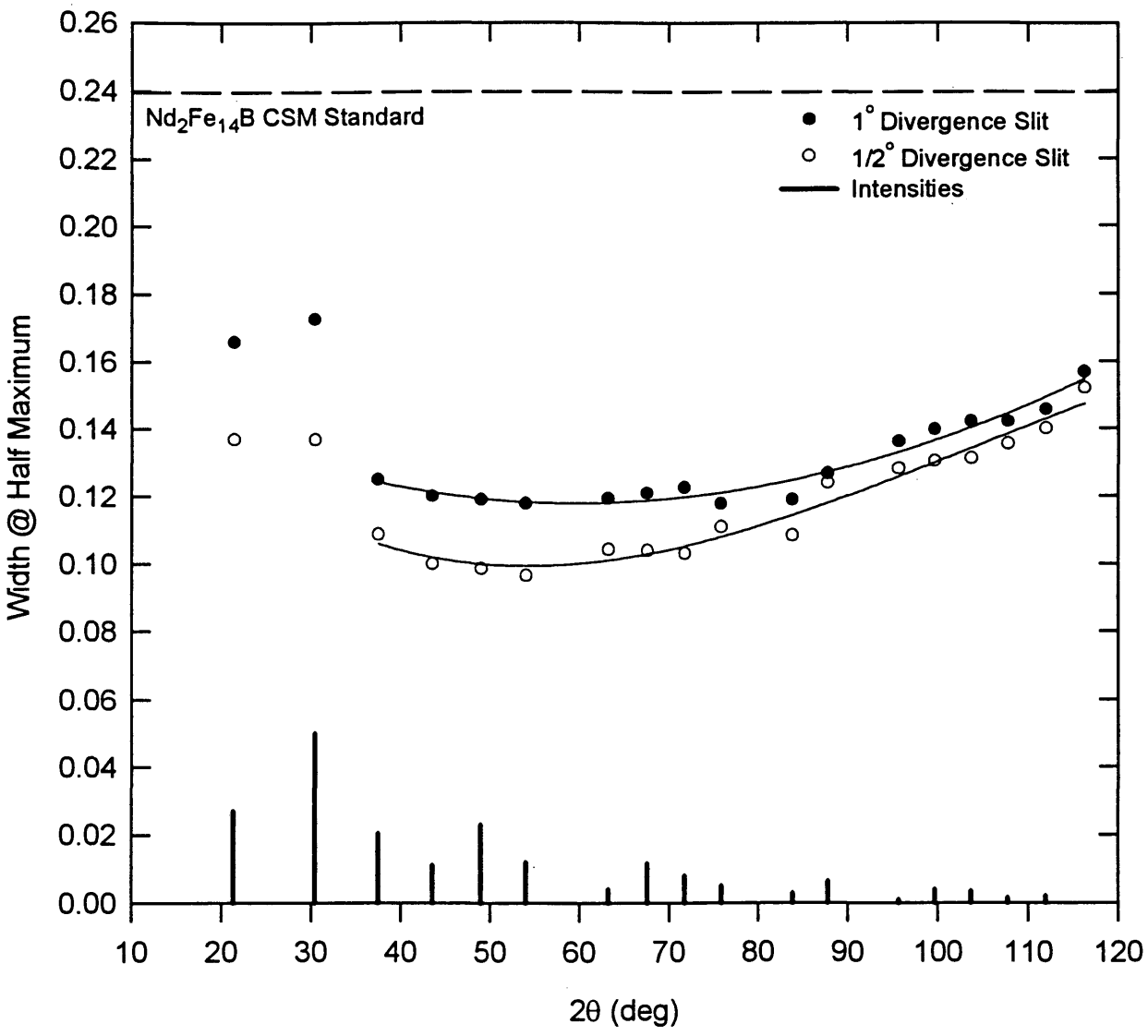

Figure 3-7: Line width calibration curve for CSM X-ray diffraction unit using a NIST LaB_6 standard sample [Cu-Kα].

function of the diffraction angle 2θ, so that the baseline standard value, B_S, could be calculated at any 2θ:

$$\text{FWHM } (LaB_6) = 0.168 - (2.69 \times 10^{-3})(2\theta) + (2.66 \times 10^{-5})(2\theta)^2 \qquad \textbf{[3.1]}$$

where:

FWHM = full width at half-maximum intensity [radians]
2θ = 2θ angle corresponding to peak position [radians]

For each alloy sample, the ***Peakfit*** software was used to fit the same four $Nd_2Fe_{14}B$ XRD peaks corresponding to the four diffraction planes with the following Miller indices: (212), (311), (214) and (410). The XRD pattern peaks corresponding to these four planes were picked for three reasons. First, the four peaks were well separated from other peaks in the XRD pattern. Second, the intensities of these four XRD peaks were high enough to produce good statistical counts for accurate fitting. Third, all four peaks appeared at low angles of 2θ. The ***Peakfit*** measured FWHM peak widths were used as the B_M term appearing in Eq. [2.7]. The mathematical equation developed for LaB_6 was used to calculate the B_S term, for Eq. [2.7], at the 2θ position corresponding to the respective 2-14-1-peak position. Using Eq. [2.7], the B term appearing in the Scherrer equation (Eq. [2.6]) was then calculated. The crystallite thickness, t, was calculated using Eq. [2.6]. The four t values corresponding to the four diffraction peaks were averaged together, and this average is the reported grainsize. It was agreed between the two groups that the grainsize would be reported along with the range of grainsize values determined for the four different peaks. For example, the measured grainsize for the U23-42-S1 sample would be reported as 35.0 (+1.2, -1.9) nm, where the average value for the four

measured peaks is 35.0 nm, and the highest determined t value would be 35.0 nm plus the first number in the parentheses, and the lowest determined t value would be 35.0 nm minus the second number in the parentheses. Appendix II contains all of the original data used in the grainsize calculations for all of the alloys measured.

Table 3-3, taken from reference [21], shows the measured t-values for both the Colorado School of Mines (CSM) and Rhodia (CRA) results for the joint grainsize study conducted on the U23 alloy. The Δt column appearing in Table 3-3 is the difference between the grainsize values measured at CSM and CRA

TABLE 3-3: Comparison of Grainsize Measuring Analysis Conducted at CSM and CRA.

Sample	CSM Grainsize (nm)	CRA Grainsize (nm)	Δt (nm)
U23-42-S1	38.5 (+1.2, -1.9)	41.1 (+4.4,-5.1)	2.6
U23-43-S1	39.3 (+4.1, -3.3)	46.0 (+10,-9.5)	6.7
U23-45-S1	38.0 (+2.5,-2.9)	44.4 (+3.6,-1.1)	6.4
U23-700-60	38.6 (+3.2,-3.6)	41.1 (+2.9,-5.1)	2.5
U23-750-60	39.3 (+3.0,-2.3)	41.6 (+4.4,-2.6)	2.3

(CRA value minus CSM value). Note that the data from both the Colorado School of Mines and the Rhodia Laboratory in France were in good agreement, although the consistently positive Δt values suggest a small systematic deviation. However, this deviation is typically within the experimental range of uncertainty. The technique used to develop these grainsize measurements was considered valid following this study.

Historically, another grainsize measuring technique similar to the one developed in cooperation with the Rhodia laboratory in Paris was developed at the Colorado School of Mines before the current technique [23]. In the first technique, an internally generated standard was used for the B_S term in Eq. [2.7]. The internally generated standard was produced by annealing a N28 alloy sample for 2 hours at 700°C, in hopes that the microstructure of the long term annealed sample would consist of uniform large grained 2-14-1 crystals with no strain gradients. The count time per step was shorter (4 s vs. 10 s) in the first analysis, decreasing the statistical clarity of the 2-14-1 peaks. In addition, no $Cu_{K\alpha-2}$ stripping was performed in the first analysis. A comparison of results from the two analysis methods will be presented in chapter 4.

It should be mentioned that the team led by Dr. Valerie Archambault in Paris produced some compelling results indicating that sample rotation during x-ray diffractometry reduces the standard deviation in the grainsize measurements [24]. Therefore, if powder samples are not rotated during x-ray diffraction measurements, then at least three samples must be analyzed to produce the same standard deviation determined for a rotating sample.

3.6 Experimental Matrix

Table 3-4A and 3-4B show the experimental matrix of samples investigated during this research effort, and include the CSM computer file numbers for both the XRD and Mössbauer data files.

TABLE 3-4A: Master List of Samples Analyzed

Alloy	Sample	Mössbauer File N°	XRD File N°
N28	N28-0-0	WA694	110797A
	N28-600-2	WA766	110897A
	N28-600-4	H-THS225	110997A
	N28-600-4-R1	NA	010798A
	N28-600-4-R2	NA	010798B
	N28-600-5.5	H-THS412	111097A
	N28-600-7	WA777	111197A
	N28-600-15	H-THS223	111297A
	N28-680-90	WA879	092596F
	N28-700-120	WA878	092596G
	N28-750-60	WA1215	120597A
	N28-750-60-R1	NA	010798C
	N28-750-60-R2	NA	010898C
U57	U57-HEAD	WA1130	111397A
	U57-750-60	WA1216	120697A
	U57-88-S1	WA1171	111797A
	U57-88-S2	WA1170	111697A
	U57-88-S3	WA1172	111897A
U58	U58-HEAD	WA1131	NA
	U58-750-60	WA1217	120797A
	U58-89-S1	WA1173	111997A
	U58-89-S2	WA1174	112097A
	U58-89-S3	WA1175	112197A

TABLE 3-4B: Master List of Samples Analyzed Continued

Alloy	Sample	Mössbauer File N°	XRD File N°
U54	U54-HEAD	WA1117	011998D
	U54-750-60	WA1218	120897A
	U54-87-S3	WA1190	112297A
	U54-87-S6	WA1191	112297B
	U54-87-S8	WA1192	112497A
U44	U44-HEAD	WA1092	011998C
	U44-750-60	WA1219	120997A
	U44-73-S5	WA1193	112397A
	U44-73-S11	WA1194	112597A
	U44-75-S3	WA1195	112697A
	U44-75-S5	WA1240	112897A
	U44-75-S8	WA1197	112997B
U43	U43-HEAD	WA1095	NA
	U43-750-60	WA1108	091697B
	U43-70-S3	WA1109	091797A
	U43-71-S3	WA1111	091897A
	U43-71-S5	WA1110	091997A
U45	U45-HEAD	WA1096	NA
	U45-750-60	WA1106	090997A
	U45-67-S4R	WA1097	092197A
	U45-69-S6	WA1105	091997B
	U45-69-S8	WA1098	082097A
U23	U23-HEAD	WA1047	061097A
	U23-42-S1	WA1041	081197E
	U23-43-S1	WA1046	062097A
	U23-45-S1	WA1063	061697A
	U23-700-60	WA1045	052997A
	U23-750-60	WA1053	060697A

Chapter 4

EXPERIMENTAL RESULTS AND DISCUSSION

4.1 Scope of Experiments Performed

During the course of this study, experiments were performed on eight different alloys with four different target compositions. Table 4-1 shows the nominal compositions of the eight alloys studied. Table 4-1 clearly shows that the primary

TABLE 4-1: Nominal Compositions (atomic%) of Alloys Examined in This Study.

Alloy	(Nd + La)	(Fe + Co)	Refractory Metal		B
			Nb	Ti	
N28	12	82	0	0	6
U43	11	77	2	0	10
U44	11	77	2	0	10
U45	11	77	2	0	10
U54	11	77	2	0	10
U23	9	79	0	2	10
U57	11	77	1	1	10
U58	11	77	1	1	10

difference in the nominal compositions lies in the refractory metal added for grain growth inhibition. Note that the N28 composition does not contain any refractory metal additions, and that the composition is almost exactly the stoichiometric composition for the $Nd_2Fe_{14}B$ (2-14-1) phase. All of the U-alloy compositions lie in the Koon patent range (Figure1-7). The U compositions are rich in boron when compared to the stoichiometric 2-14-1 composition.

Annealing experiments were performed on all eight alloys. Mössbauer spectroscopy was used to determine the phase distribution of the annealed samples as well as the samples in the as-received condition (head samples). X-ray diffraction (XRD) measurement were taken on all of the annealed samples and some of the more crystalline head samples to detect new phases and measure the grainsize of the 2-14-1 crystals.

In the following, two types of sample designations will be used, because two types of sampling were used during the experimental annealing. Samples labeled like U45-67-S4 list the alloy (U45), followed by the run number (67), and finally the sample number (S4). Samples labeled like U45-750-60 list the alloy (U45), followed by the annealing temperature (750), and finally the residence time in minutes (60).

4.2 The N28 Alloy Results

The N28 alloy is interesting for two reasons. First, N28 does not contain any refractory metal additions for grain growth inhibition. Second, N28 was the alloy used to develop the first grainsize measuring technique [22]. The first grainsize measuring efforts indicated that there was significant grain growth in the annealed N28 samples. An internally generated standard was used in the Scherrer grainsize calculations of the first grainsize measuring technique. As discussed in chapter 3, the new improved XRD technique developed in

cooperation between the Colorado School of Mines and the Rhodia laboratory in France (CRA) uses a NIST LaB_6 standard. The plan of this study was to compare the grain growth results obtained with the first grainsize measuring technique, with the results from the improved XRD collaborative grainsize measuring technique. In addition to the grain growth experiments, a high temperature anneal was conducted to determine if any previously undetected phases would appear during more extreme annealing conditions.

Table 4-2 shows both the Mössbauer and XRD results of the N28 series. Several interesting points are illustrated by Table 4-2. Note that the Mössbauer results are listed as % Fe as; this designation denotes the percentage of total iron in the sample reporting to a specific phase. The reanalysis of the N28 samples using the new improved XRD grainsize measuring technique produced some intriguing results. First, the reanalysis showed that the N28 samples, which do not contain any refractory metal grain growth inhibiting additions, do experience significant grain growth initially. Figure 4-1 is a plot of the increasing grainsize of the N28 samples as a function of annealing time. Note that the grainsize measuring technique used for Figure 4-1 is the improved grainsize measuring technique developed in cooperation with CRA. The error bars shown in Figure 4-1 do not correspond to the error values listed in Table 4-2. The grainsize ranges are listed in Table 4-2 according to the technique described in Chapter 3, while the error bars shown in Figure 4-1 are averaged values of the two range numbers listed in Table 4-2. Interestingly, the samples annealed at 600°C did experience continual growth during the first 15 minutes from approximately 36 nm to 50 nm. Samples annealed for periods longer than 15 minutes did not experience any further growth. It is important to note that the samples annealed in this study for time periods longer than 15 minutes were all annealed at different temperatures, and all annealed at temperatures greater than 600°C. It seems that there is an upper limit to the grainsize achievable in

TABLE 4-2: XRD Grainsize and Mössbauer Results for N28 alloy.

SAMPLE	ANNEAL TEMP (°C)	RESIDENCE TIME (min)	IRON DISTRIBUTION (% Fe AS)				GRAIN SIZE (nm)
			$Nd_2Fe_{14}B$	α-Fe	Nd-Fe-B	Fe_3B	
N28-HEAD	none	none	10	4	86	0	NA
N28-600-2	600	2.0	20	9	71	0	38.0 (+3.6,-4.3)
N28-600-4	600	4.0	34	7	59	0	34.4 (+3.2,-1.8)
N28-600-4-R1	600	4.0	NA	NA	NA	NA	35.0 (+4.8,-3.3)
N28-600-4-R2	600	4.0	NA	NA	NA	NA	34.8 (+2.4,-3.4)
N28-600-5.5	600	5.5	69	11	20	0	43.2 (+4.8,-2.5)
N28-600-7	600	7.0	81	11	8	0	46.5 (+7.5,-6.2)
N28-600-15	600	15	88	10	2	0	49.7 (+4.4,-3.5)
N28-680-90	680	90	88	12	0	0	47.4 (+3.2,-1.7)
N28-700-120	700	120	88	12	0	0	49.3 (+2.9,-1.1)
N28-750-60	750	60	80	13	0	7	54.6 (+3.6,-3.2)
N28-750-60-R1	750	60	NA	NA	NA	NA	51.9 (+6.6,-3.3)
N28-750-60-R2	750	60	NA	NA	NA	NA	45.2 (+0.8,-0.5)

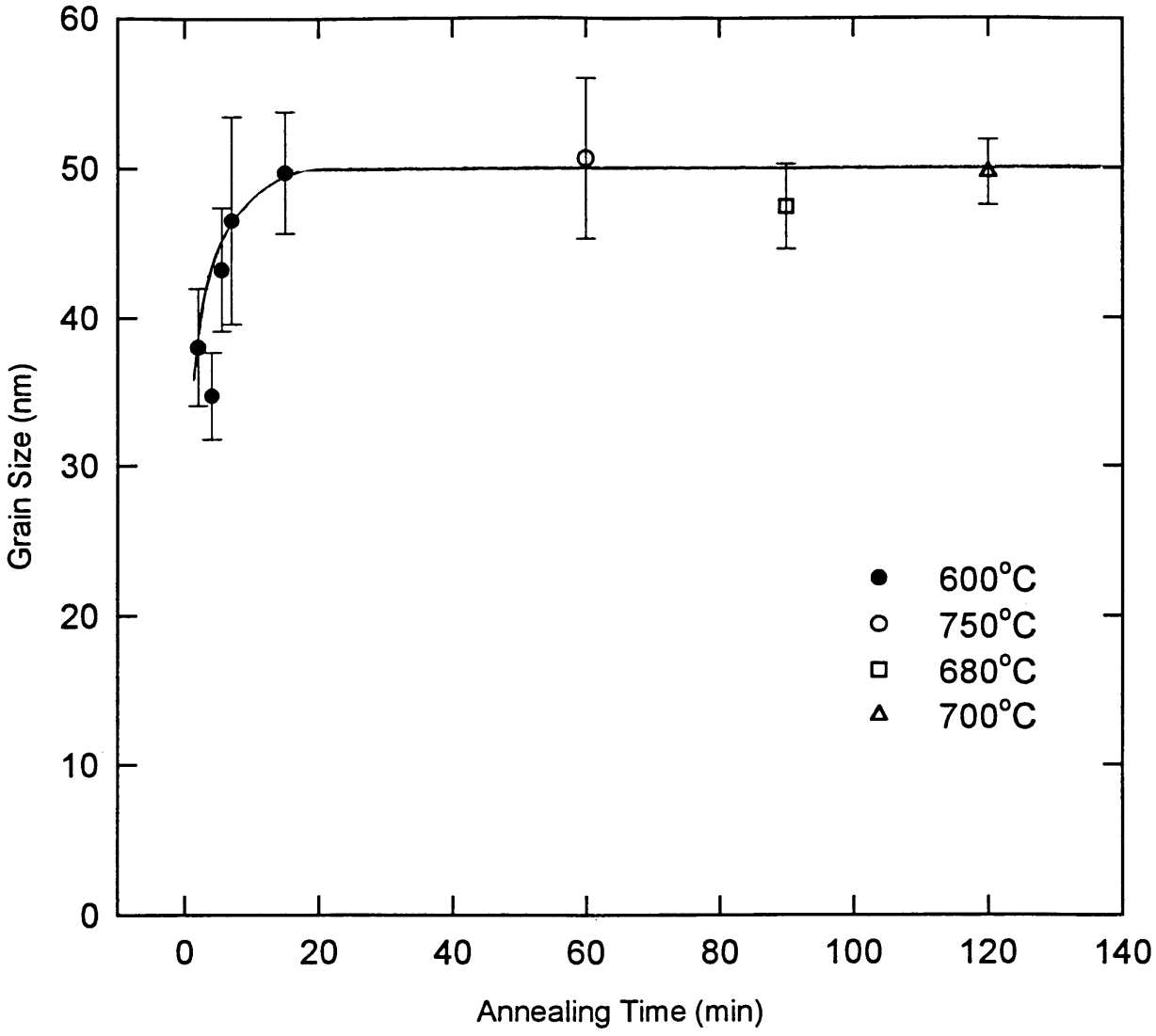

Figure 4-1: Variation of grain size as a function of annealing time for the N28 alloy. Note that a NIST LaB_6 standard was used for this Scherrer analysis. The solid line is drawn to guide the eye.

this alloy system independent of annealing time or temperature (at least up to 750°C). It is also important to note that the grainsize changes were only measured on the 2-14-1 phase. Therefore, the previous statements about limited grain growth can only be definitively made about the 2-14-1 phase.

Figure 4-2 is a plot based on the same raw XRD data as Figure 4-1. However, Figure 4-2 was generated using the first grainsize measuring technique. It would seem that generating an internal standard from the source material may overestimate the grain growth actually experienced by the samples. If the new XRD analysis as demonstrated in Figure 4-1 is correct, and no further grain growth is experienced by these samples after the first fifteen minutes independent of time or temperature, then an internally generated standard would not have sufficiently large grains to use effectively in a Scherrer analysis. Therefore, the continual grain growth demonstrated in Figure 4-2 is incorrect.

The Mössbauer phase distribution analysis also showed some interesting results. Table 4-2 shows the Mössbauer phase distributions for all of the samples examined. Figure 4-3 shows the variation in the phase distribution of the N28 samples as a function of annealing time. Please note that there was 4% α-Fe present in the head sample, and that there is a significant phase fraction of α-Fe in all of the annealed samples. Figure 4-3 clearly shows that in the 600°C series, as annealing time increases there is a continual increase in the phase fraction of 2-14-1, and a continual decrease in the amount of the amorphous Nd-Fe-B phase. The samples annealed at 680°C for 90 minutes and 700°C for 120 minutes showed a stable phase distribution of 88% 2-14-1 and 12% α-Fe, indicating that this is the equilibrium phase distribution in this temperature range independent of time. Comparison of the grain growth data plotted in Figure 4-1 and the phase transformation data plotted in Figure 4-3, shows that all of the grain growth experienced in this alloy occurred during the crystallization process.

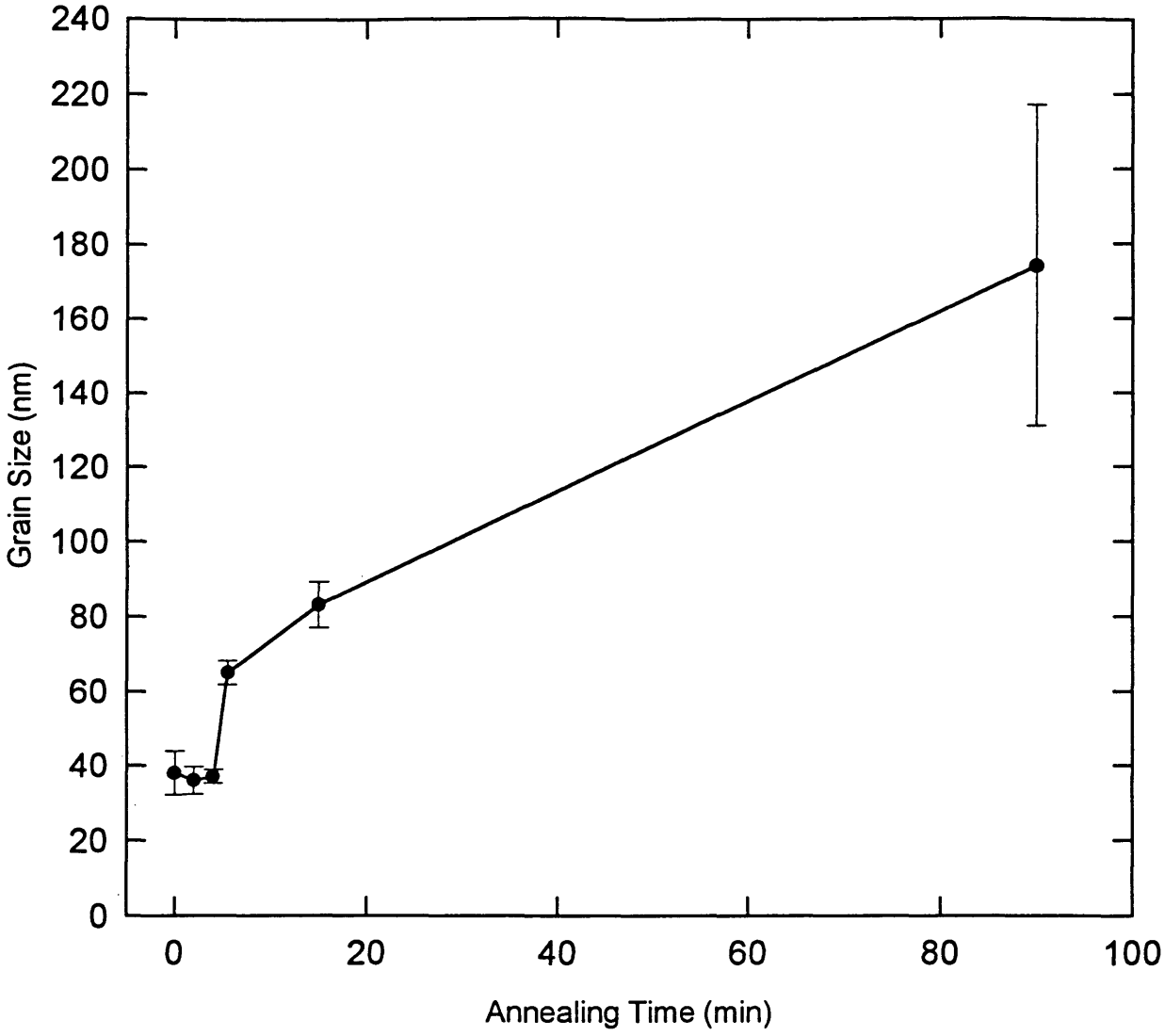

Figure 4-2: Variation of N28 grain size as a function of annealing time. Note that the standard used for this Scherrer analysis was a sample annealed for 120 min at 700°C.

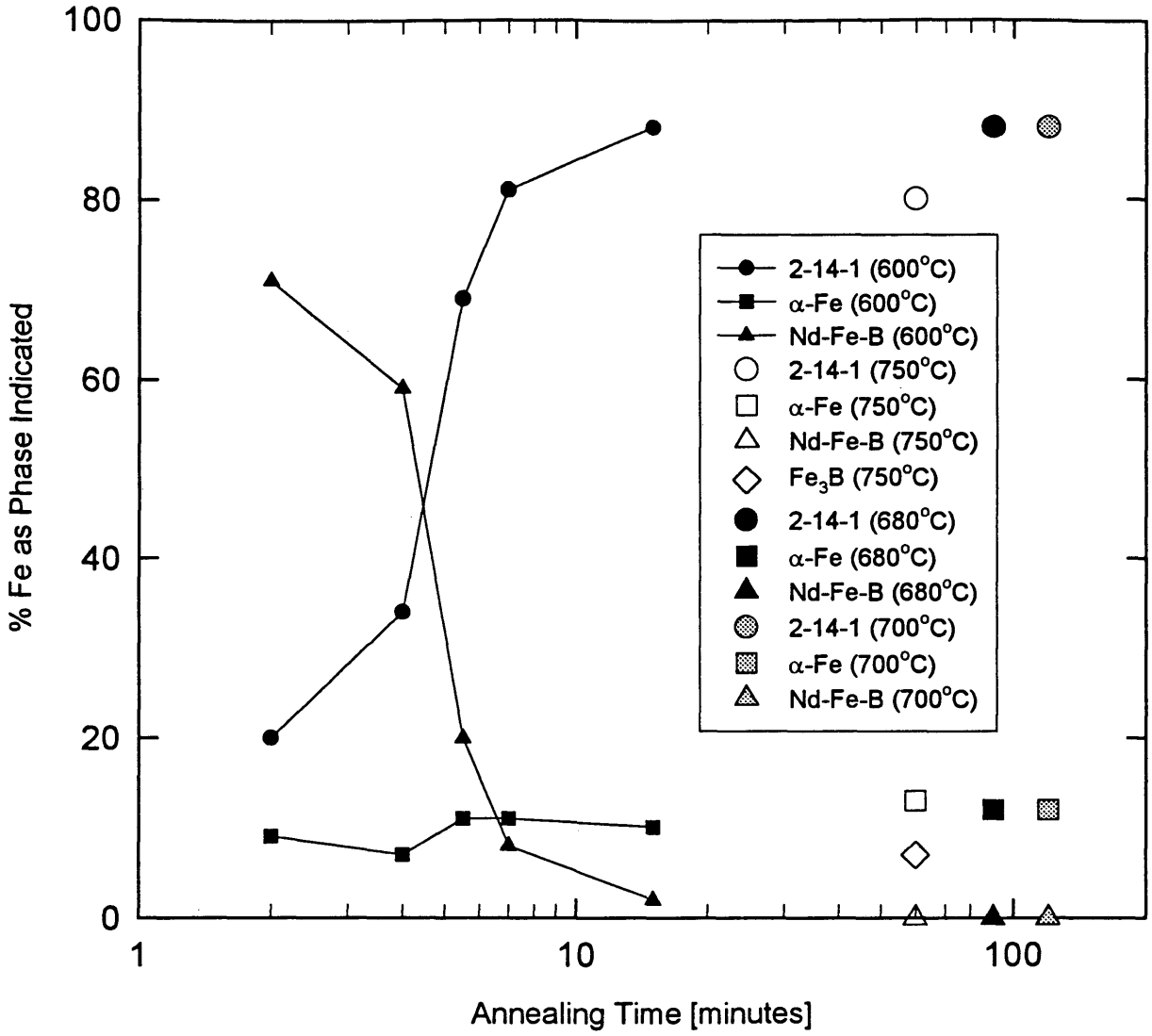

Figure 4-3: Variation in N28 phase distribution as a function of annealing time (on a logarithmic scale).

The sample annealed at 750°C for 60 minutes showed a significant phase fraction of Fe_3B (7%). Both the Mössbauer spectrum for this sample and the XRD pattern for this sample support the identification of Fe_3B. It is interesting to note that the Fe_3B phase was not detected in the N28 alloy until the annealing temperature was raised to 750°C in the N28-750-60 sample. In fact, the N28-680-90 and N28-700-120 samples were annealed for longer time periods at slightly lower temperatures, and yet no Fe_3B was detected in either of these samples. The lack of Fe_3B precipitation during long annealing periods until a specific temperature is reached, suggests an activation energy barrier for the precipitation of the Fe_3B.

Note that when the amount of $Nd_2Fe_{14}B$ present in the N28-700-120 sample is compared with the amount of $Nd_2Fe_{14}B$ present in the N28-750-60 sample, the amount of $Nd_2Fe_{14}B$ drops 8 atomic percent in the N28-750-60 sample. It seems that at the higher annealing temperature, 750°C, the $Nd_2Fe_{14}B$ phase decomposed to form the Fe_3B phase. As the iron and boron in the $Nd_2Fe_{14}B$ phase combined with the excess boron to form Fe_3B, where did the neodymium go? There may be neodymium solubility in the Fe_3B and α-Fe. The following reaction demonstrates how some of the neodymium could be present in the Fe_3B and the α-Fe:

$$Nd_2Fe_{14}B \longrightarrow [Fe_{0.7}Nd_{0.3}]_3B + 11[Fe_{0.9}Nd_{0.1}] \quad \textbf{[4.1]}$$

Mössbauer spectroscopy only detects iron-containing phases. If the neodymium formed a non-iron containing phase, then it would not be detected by the Mössbauer spectroscopy.

4.3 The U43, U44, and U45 Results

Several interesting features of this alloy series make it a prime candidate for this thesis. These alloys all have the same nominal composition and all are doped with niobium to inhibit grain growth. Experimental annealing runs were performed on all of these alloys with both standard (665°C, 3 min) and non-standard annealing conditions. In this series, the first alloy to be studied was U45. Because the U45 experiments showed some interesting results, the same experiments were duplicated with the U43 alloy to check for reproducibility. In the experimental runs of the U45 and U43 alloys, the furnace thermal profile was adjusted so that the powder experienced higher annealing temperatures for longer residence times than for the standard annealing conditions. A new series of experiments was developed for the U44 alloy. In the experimental run conducted on U44, the furnace thermal profile was adjusted so that the run powder experienced lower annealing temperatures for longer residence times than in standard annealing conditions. The powder annealed during the altered thermal profiles did show poorer magnetic properties.

Although these alloys all have the same target and nominal compositions, the magnetic properties of the U44 alloy annealed under standard annealing conditions are inferior to the magnetic properties of the U43 and U45 alloys annealed under standard annealing conditions.

Tables 4-3, 4-4, and 4-5 show the Mössbauer, XRD, and magnetic properties for the U45, U43, and U44 sample series respectively. Both standard and non-standard annealing experiments were conducted on all three alloys. The standard annealing conditions (665°C for 3 minutes) were used during experimental runs 67, 70, and 73 for the U45, U43, and U44 alloys respectively. During experimental run 69, conducted on the U45 alloy, the furnace temperature was ramped up from 665°C at a rate of 0.5°C/ min for one hour while alloy

TABLE 4-3: Mössbauer, XRD, and Magnetic Properties of U45 Alloy.

SAMPLE	ANNEAL	RESIDENCE	IRON DISTRIBUTION (% Fe AS)				MAGNETIC PROPERTIES			GRAIN SIZE
	T (°C)	TIME (min)	$Nd_2Fe_{14}B$	α-Fe	Nd-Fe-B	$NdFe_4B_4$	B_r (kG)	H_{ci} (kOe)	BH_{max} (MGOe)	(nm)
U45-HEAD	none	none	5	0	95	0	NA	NA	NA	NA
U45-67-S4	665	3.0	64	0	34	2	7.4	15.9	10.9	37.8 (+4.7,-3.0)
U45-69-S6	695	3.5 > t > 3.0	65	0	33	2	7.1	14.0	9.6	37.2 (+3.1,-3.3)
U45-69-S8	695	3.5 > t > 3.0	65	0	32	3	6.9	12.4	9.0	35.9 (+1.0,-1.8)
U45-750-60	750	60	77	0	17	6	NA	NA	NA	36.4 (+1.9,-2.7)

TABLE 4-4: Mössbauer, XRD, and Magnetic Properties of U43 Alloy.

SAMPLE	ANNEAL	RESIDENCE	IRON DISTRIBUTION (% Fe AS)				MAGNETIC PROPERTIES			GRAIN SIZE
	T (°C)	TIME (min)	$Nd_2Fe_{14}B$	α-Fe	Nd-Fe-B	$NdFe_4B_4$	B_r (kG)	H_{ci} (kOe)	BH_{max} (MGOe)	(nm)
U43-HEAD	none	none	9	0	91	0	NA	NA	NA	NA
U43-70-S3	665	3.0	62	0	36	2	7.4	15.7	10.9	36.4 (+2.5,-3.4)
U43-71-S3	695	3.5 > t > 3.0	66	0	32	2	7.3	14.8	10.6	37.0 (+1.6,-3.0)
U43-71-S5	695	3.5 > t > 3.0	64	0	33	3	7.3	13.2	10.0	37.2 (+3.8,-2.3)
U43-750-60	750	60	76	1	16	7	NA	NA	NA	37.2 (+1.8,-1.5)

TABLE 4-5: Mössbauer, XRD, and Magnetic Properties of U44 Alloy.

SAMPLE	ANNEAL	RESIDENCE	IRON DISTRIBUTION (% Fe AS)				MAGNETIC PROPERTIES			GRAIN SIZE
	T (°C)	TIME (min)	$Nd_2Fe_{14}B$	α-Fe	Nd-Fe-B	$NdFe_4B_4$	B_r (kG)	H_{cl} (kOe)	BH_{max} (MGOe)	(nm)
U44-HEAD	none	none	23	0	77	0	NA	NA	NA	31.5 (+0.5,-0.4)
U44-73-S5	665	3.0	65	0	33	2	7.0	14.1	9.4	37.4 (+1.9,-0.5)
U44-73-S11	665	3.0	64	0	34	2	7.1	13.9	10.0	39.8 (+3.8,-1.6)
U44-75-S3	650	3.0 > t > 2.5	63	0	34	3	7.0	13.2	8.7	38.9 (+1.9,-3.3)
U44-75-S5	640	3.0 > t > 2.5	64	0	33	3	7.0	13.6	9.2	39.7 (+0.8,-0.9)
U44-75-S8	635	3.0 > t > 2.5	52	0	45	3	5.4	9.1	3.2	38.8 (+1.1,-3.6)
U44-750-60	750	60	77	1	16	6	NA	NA	NA	35.0 (+2.1,-2.4)

powder samples were periodically taken. All of the powder annealed during experimental run 69 experienced higher temperatures for longer residence times than during a standard annealing run. Experimental run 71 conducted on the U43 alloy duplicated the thermal processing conditions of run 69. During experimental run 75, conducted on the U44 alloy, the furnace temperature was ramped down from 665°C at a rate of 0.5°C/min for one hour while alloy powder samples were periodically taken. All of the powder annealed during experimental run 75 experienced lower annealing temperatures for shorter residence times than during a standard annealing run.

Tables 4-3 and 4-4 show that a significant drop in intrinsic coercivity (H_{ci}) was measured in the samples annealed during experimental runs 69 and 71, which directly corresponded to the higher annealing temperatures. Although the powder annealed during runs 69 and 71 experienced significantly different thermal processing conditions and showed a drop in H_{ci} compared to the powder annealed during runs 67 and 70, Tables 4-3 and 4-4 show that there is no significant difference in either the measured grainsize or phase distribution of these samples. In fact, there seems to be no significant difference in the grainsize of the powders annealed for 3 minutes at 665°C and the powders annealed for 60 minutes at 750°C in the U43, U44, and U45 series.

Table 4-5 shows that the U44 powder annealed in experiment 75 did have inferior magnetic properties to the U44 powder annealed during the standard annealing conditions experienced during experiment 73. However, there is no significant difference in either phase distribution or grainsize to explain this drop in the magnetic properties in the U44-75-S3 and U44-75-S5 samples. In the U44-75-S8 sample, the 30°C drop is evident in a significantly less crystallized powder, which may explain the poor magnetic properties. However, even the poorly crystallized U44-75-S8 powder shows approximately the same 2-14-1 grainsize.

It should be noted that in all three alloys, the samples annealed at 750°C for 60 minutes showed larger phase fractions of 2-14-1 and $NdFe_4B_4$ than the samples annealed during standard annealing conditions. The samples annealed for 60 minutes at 750°C showed approximately the same phase distribution when comparing the U43, U44, and U45 alloys. Also, note that little or no α-Fe appeared in this alloy composition during any of the experimental annealing conditions. It is interesting that there was 16-17% retained amorphous phase in all of the samples annealed at 750°C for 60 minutes.

There is a possible explanation for the inferior coercivities measured in the U44 powder annealed under standard annealing conditions when compared with the coercivities of the U43 and U45 powders annealed under standard annealing conditions. Although the U44 powder annealed during run 73 does not show a significantly different grainsize or phase distribution than the U43 and U45 powders from runs 70 and 67, it is interesting to note that the U44-HEAD sample contains a significantly larger crystallized fraction of 2-14-1 (23%) than the head samples of the U45 (5%) and the U43 (9%) alloys. This suggests a correlation between a partially crystallized precursor and poor magnetic properties, independent of the final phase distribution or grainsize. It is possible that the final morphology of the microstructure is significantly affected by the amount of crystallinity in the precursor, and that these microstructural differences explain the magnetic differences.

4.4 The U54 Alloy Results

The U54 alloy has the same nominal composition as U43, U44, and U45; niobium is U54's refractory metal grain growth inhibiting additive (Table 4-1). This alloy is a good candidate for the study because Mössbauer spectroscopy revealed that the head sample of this alloy contained a significant phase fraction

of crystallized 2-14-1 (28%). The measured magnetic properties of the annealed samples of this alloy are poor, similar to the U44 behavior. It is possible that the head material contains a significantly different morphology, and therefore, one would expect the final product to also contain a different morphology that would explain the alloy's inferior magnetic properties. The U54 samples heat-treated in the standard annealing conditions (665°C, 3 minutes) were examined by both Mössbauer spectroscopy and XRD. In addition, a head sample was annealed for one hour at 750°C and fully analyzed. XRD analysis of the head sample was also performed, in an attempt to measure the crystallite sizes of the 2-14-1 grains present in the amorphous precursor coming directly from the quench.

Table 4-6 shows the Mössbauer, XRD, and magnetic properties for the U54 sample series. First, note that the head sample has significant crystallinity with 28% $Nd_2Fe_{14}B$ and 2% $NdFe_4B_4$. Only 70% of the iron in the head sample is reporting to the amorphous Nd-Fe-B. Both the intrinsic coercivities (H_{ci}) and the energy products (BH_{max}) of the samples annealed under standard annealing conditions (665°C, 3 minutes) are poor. Second, note that the phase distributions of the samples annealed under standard conditions are the same within measurement uncertainty. Third, note that the sample annealed at high temperature (750°C, 60 minutes) contains 3% α-Fe and 6% $NdFe_4B_4$. This is the only sample of the U54 series in which the α-Fe appeared. It seems that higher temperatures promote the precipitation of both α-Fe and $NdFe_4B_4$.

The XRD study also provides some interesting insights. First, note that the grainsize of all the samples remains constant at approximately 40 nm independent of annealing time or temperature. A grainsize of 40 nm is somewhat larger than previously discussed for U samples, but it is hard to say if the grainsize enlargement is responsible for the poor magnetic performance of

TABLE 4-6: Mössbauer, XRD, and Magnetic Properties of U54 Alloy.

SAMPLE	ANNEAL	RESIDENCE	IRON DISTRIBUTION (% Fe AS)				MAGNETIC PROPERTIES			GRAIN SIZE
	T (°C)	TIME (min)	$Nd_2Fe_{14}B$	α-Fe	Nd-Fe-B	$NdFe_4B_4$	B_r (kG)	H_{cl} (kOe)	BH_{max} (MGOe)	(nm)
U54-HEAD	none	none	28	0	70	2	NA	NA	NA	39.9 (+3.7,-3.8)
U54-87-S3	665	3.0	63	0	35	2	7.1	13.2	9.2	41.1 (+2.7,-2.5)
U54-87-S6	665	3.0	63	0	35	2	7.2	12.6	8.3	39.8 (+0.9,-0.8)
U54-87-S8	665	3.0	64	0	34	2	7.2	12.8	8.6	37.3 (+1.8,-1.7)
U54-750-60	750	60	75	3	16	6	NA	NA	NA	39.3 (+1.8,-1.5)

this alloy. It is more likely that the crystalline material present in the head material significantly altered the morphologies of the samples annealed under standard annealing conditions, degrading the magnetic properties of these samples in the process.

4.5 The U23 Alloy Results

The U23 alloy is a good candidate for the study for two reasons. First, U23 was doped with titanium to inhibit grain growth instead of niobium. The titanium additions may affect the morphology of the microstructure differently than niobium additions. It is possible that the Mössbauer and XRD studies might detect either a grainsize difference and/or a phase distribution difference. Second, U23 was the subject alloy of the XRD grainsize measuring technique developed in cooperation between the Colorado School of Mines and a Rhodia lab in France. Historically this alloy was important to the development of the thesis.

Table 4-7 shows the Mössbauer, XRD, and magnetic properties for the U23 sample series. First, note that the U23-HEAD sample contains a significant fraction of crystallized 2-14-1 (19%). It is interesting to note that the intrinsic coercivities (H_{ci}) and energy products (BH_{max}) of runs 42, 43 and 45 are relatively poor, while the remanence values (B_r) are quite good when compared to those of the U43, U44, U45, and U54 alloys. It is not clear whether the altered magnetic properties are due to compositional variations (this is the only alloy that contains only Ti as an addition), or due to a different morphology generated by a significantly crystalline head material (similar to U44 and U54). Second, note that the phase distributions of the samples from runs 42, 43, and 45 are the same within measurement uncertainty. Note that these samples have the same phase distribution even though the annealing conditions of run 43 (685°C, 2.4

TABLE 4-7: Mössbauer, XRD, and Magnetic Properties of U23 Alloy.

SAMPLE	ANNEAL	RESIDENCE	IRON DISTRIBUTION (% Fe AS)			MAGNETIC PROPERTIES			GRAIN SIZE
	T (°C)	TIME (min)	$Nd_2Fe_{14}B$	α-Fe	Nd-Fe-B	B_r (kG)	H_{cj} (kOe)	BH_{max} (MGOe)	(nm)
U23-HEAD	none	none	19	0	81	NA	NA	NA	35.5 (+2.8,-2.8)
U23-42-S1	665	3.0	61	0	39	8.0	10.0	11.8	38.5 (+1.2,-1.9)
U23-42-S1-R	665	3.0	NA	NA	NA	NA	NA	NA	39.4 (+4.5,-2.7)
U23-43-S1	685	2.4	63	0	37	8.1	9.9	12.2	39.3 (+4.1,-3.3)
U23-45-S1	665	3.0	61	0	39	7.9	10.0	11.6	38.0 (+2.5,-2.1)
U23-700-60	700	60	66	4	30	7.9	7.7	8.7	38.6 (+3.2,-3.6)
U23-750-60	750	60	67	11	22	7.5	7.5	8.0	39.3 (+3.0,-2.3)

minutes) were not the same as the annealing conditions of runs 42 and 45 (665°C, 3 minutes). Third, two different high temperature annealing experiments were performed, one at 700°C for 60 minutes and one at 750°C for 60 minutes. There does not seem to be a significant difference in the amount of 2-14-1 precipitated from the amorphous precursor in the 700°C sample and the 750°C sample. However, a significantly larger phase fraction of α-Fe precipitated in the 750°C sample. As mentioned for the precipitation of Fe_3B in the N28 alloy, the precipitation of α-Fe in the U23 alloy may have an activation energy barrier. It may be important to note that no phases besides α-Fe and 2-14-1 precipitated in this alloy, even at high temperatures.

The XRD grainsize analysis also provided some interesting results. Note that all of the samples investigated have approximately the same grainsize (~38 nm) independent of annealing time or temperature. The U23-HEAD sample does have a slightly finer grainsize (35.5 nm), but it is hard to say if this is a real effect or just experimental uncertainty. The U23-HEAD sample does contain a large phase fraction of amorphous material (81%), which tends to make accurate peak widths of the 2-14-1 phase hard to determine. There is more error inherent in grainsize measurements using the current technique for highly amorphous samples.

4.6 The U57 and U58 Alloy Results

There are several factors that make the U57 and U58 alloys prime candidates for this study. First, these alloys contain a combination of both titanium and niobium additions for grain growth inhibition (Table 4-1). Therefore, these alloys may contain a different phase distribution and/or crystallite size than the alloys doped with just niobium or just titanium. Second, preliminary Mössbauer phase distribution measurements of these two alloys indicated a significantly different

amount of crystalline material present in the head samples. Third, although the two alloys have the same nominal composition, the powder from these two alloys annealed under standard annealing conditions (665°C, 3 minutes) showed significantly different magnetic properties. In addition to the standard anneal conditions, a high temperature anneal (750°C, 60 minutes) was conducted on both the U57 and U58 alloys to determine if any new phases appear at high temperature, and to see if these alloys experienced high temperature grain growth.

Tables 4-8 and 4-9 show the Mössbauer, XRD, and magnetic properties for the U57 and U58 sample series, respectively. There are several interesting results shown by the XRD grainsize analysis. First, the U57 alloy seems to have a slightly larger average grainsize (~34 nm) than the U58 alloy (~31 nm). Note that the U57-HEAD sample already contains 28% crystalline $Nd_2Fe_{14}B$ (2-14-1), and that the average grainsize of these 2-14-1 crystals is already 35.7 nm before annealing. As noted before, it is probable that the morphology developed during the rapid quenching of these alloys directly affects the morphology of the end product. Second, in both the U57 alloy and the U58 alloy, there does not seem to be significant grain growth. All of the samples in either series have approximately the same grainsize independent of annealing time or temperature. Third, it is interesting to note that the U58 alloy, which has superior magnetic properties, is also the alloy with the finer grainsize.

The Mössbauer analysis also produced several interesting results. First, it is important to note again that the two head samples differ significantly in phase distribution. The U57-HEAD sample contains 28% crystalline 2-14-1 and only 72% amorphous matrix, while the U58-HEAD sample contains only 6% crystalline 2-14-1 and 94% amorphous matrix. Note that the intrinsic coercivities (H_{ci}) of the U57 alloy are inferior to those of the U58 alloy. Second, all of the samples annealed under standard annealing conditions (665°C, 3 minutes) in

TABLE 4-8: Mössbauer, XRD, and Magnetic Properties of U57 Alloy.

SAMPLE	ANNEAL	RESIDE.	IRON DISTRIBUTION (% Fe AS)					MAGNETIC PROPERTIES			GRAIN SIZE
	T (°C)	T (min)	$Nd_2Fe_{14}B$	α-Fe	Nd-Fe-B	$NdFe_4B_4$	Fe_3B	B_r (kG)	H_{cl} (kOe)	BH_{max} (MGOe)	(nm)
U57-HEAD	none	none	28	0	72	0	0	NA	NA	NA	35.7 (+2.2,-2.7)
U57-88-S1	665	3.0	64	0	34	2	0	7.1	13.2	9.2	35.6 (+4.0,-2.3)
U57-88-S2	665	3.0	64	0	34	2	0	7.3	14.6	11.2	33.1 (+3.0,-2.3)
U57-88-S3	665	3.0	64	0	34	2	0	7.1	14.6	9.8	33.5 (+2.0,-2.7)
U57-750-60	750	60	78	4	11	3	4	NA	NA	NA	33.3 (+0.9,-1.0)

TABLE 4-9: Mössbauer, XRD, and Magnetic Properties of U58 Alloy.

SAMPLE	ANNEAL	RESIDE.	IRON DISTRIBUTION (% Fe AS)					MAGNETIC PROPERTIES			GRAIN SIZE
	T (°C)	T (min)	$Nd_2Fe_{14}B$	α-Fe	Nd-Fe-B	$NdFe_4B_4$	Fe_3B	B_r (kG)	H_{ci} (kOe)	BH_{max} (MGOe)	(nm)
U58-HEAD	none	none	6	0	94	0	0	NA	NA	NA	NA
U58-89-S1	665	3.0	65	0	34	1	0	7.2	15.9	10.5	32.0 (+2.8,-3.5)
U58-89-S2	665	3.0	67	0	32	1	0	7.0	15.9	9.7	31.7 (+4.0,-2.7)
U58-89-S3	665	3.0	67	0	32	1	0	6.8	16.0	9.2	31.3 (+4.2,+3.4)
U58-750-60	750	60	78	1	15	2	4	NA	NA	NA	30.5 (+2.8,-1.8)

both alloys have approximately the same phase distribution. Third, the high temperature anneal samples (750°C, 60 minutes) developed different phase distributions. In both alloys, α-Fe precipitated during the 750°C anneals. However, it may be important to note that the U57 alloy, which had the significantly crystalline head sample, shows 4% α-Fe, while the U58 sample only precipitated 1% α-Fe. Both high temperature anneal samples precipitated 4 phases 2-14-1, α-Fe, $FeNd_4B_4$, and Fe_3B. This is the only alloy series that precipitated all four of the phases that have been detected to date. Finally, note that 10-15% amorphous phase is retained in the samples annealed at 750°C for 60 minutes. It is interesting that the metastable amorphous precursor does not completely crystallize even in severe annealing conditions.

4.7 Comparison of Results

Several important trends appear when the data from the eight alloys are compared. Tables 4-10 and 4-11 were generated for easy comparison between alloy compositions. Therefore, these tables show the magnetic properties in addition to the Mössbauer spectroscopy and XRD results for all of the alloys investigated. To look for systematic trends in the data in Tables 4-10 and 4-11, several space saving data compressions were made. In Tables 4-10 and 4-11, the sample designations marked with an asterisk denote that more than one measurement for this particular sample was taken, and the values have been averaged. The sample designations that end in AVG note that the measured values listed for this sample represent an average value of all of the samples with this composition that were annealed under the same conditions. Notice that no magnetic properties were measured for the N28 alloy series.

TABLE 4-10: Comparison Table of Mössbauer, XRD, and Magnetic Properties for All Alloys Studied.

SAMPLE	ANNEAL	RESIDE.	IRON DISTRIBUTION (% Fe AS)					MAGNETIC PROPERTIES			GRAIN SIZE
	T (°C)	T (min)	$Nd_2Fe_{14}B$	α-Fe	Nd-Fe-B	$NdFe_4B_4$	Fe_3B	B_r (kG)	H_{cj} (kOe)	BH_{max} (MGOe)	(nm)
N28-HEAD	none	none	10	4	86	0	0	NA	NA	NA	NA
N28-600-2	600	2.0	20	9	71	0	0	NA	NA	NA	38.0 (+3.6,-4.3)
N28-600-4*	600	4.0	34	7	59	0	0	NA	NA	NA	34.7 (+3.5,-2.8) *
N28-600-5.5	600	5.5	69	11	20	0	0	NA	NA	NA	43.2 (+4.8,-2.5)
N28-600-7	600	7.0	81	11	8	0	0	NA	NA	NA	46.5 (+7.5,-6.2)
N28-600-15	600	15	88	10	2	0	0	NA	NA	NA	49.7 (+4.4,-3.5)
N28-680-90	680	90	88	12	0	0	0	NA	NA	NA	47.4 (+3.2,-1.7)
N28-700-120	700	120	88	12	0	0	0	NA	NA	NA	49.3 (+2.9,-1.1)
N28-750-60*	750	60	80	13	0	0	7	NA	NA	NA	50.6 (+3.7,-2.3)*
U45-HEAD	none	none	5	0	95	0	0	NA	NA	NA	NA
U45-67-S4	665	3.0	64	0	34	2	0	7.4	15.9	10.9	37.8 (+4.7,-3.0)
U45-69-S8	695	3.5 > t > 3.0	65	0	32	3	0	6.9	12.4	9.0	35.9 (+1.0,-1.8)
U45-750-60	750	60	77	0	17	6	0	NA	NA	NA	36.4 (+1.9,-2.7)
U43-HEAD	none	none	9	0	91	0	0	NA	NA	NA	NA
U43-70-S3	665	3.0	62	0	36	2	0	7.4	15.7	10.9	36.4 (+2.5,-3.4)
U43-71-S5	695	3.5 > t > 3.0	64	0	33	3	0	7.3	13.2	10.0	37.2 (+3.8,-2.3)
U43-750-60	750	60	76	1	16	7	0	NA	NA	NA	37.2 (+1.8,-1.5)

TABLE 4-11: Comparison Table of Mössbauer, XRD, and Magnetic Properties for All Alloys Studied.

SAMPLE	ANNEAL	RESIDE.	IRON DISTRIBUTION (% Fe AS)					MAGNETIC PROPERTIES			GRAIN SIZE
	T (°C)	T (min)	$Nd_2Fe_{14}B$	α-Fe	Nd-Fe-B	$NdFe_4B_4$	Fe_3B	B_r (kG)	H_{ci} (kOe)	BH_{max} (MGOe)	(nm)
U44-HEAD	none	none	23	0	77	0	0	NA	NA	NA	31.5 (+0.5,-0.4)
U44-73-AVG	665	3.0	65*	0*	33*	2*	0*	7.0*	14.0*	9.7*	38.6 (+2.9,-1.1)*
U44-75-S3	650	3.0 > t > 2.5	63	0	34	3	0	7.0	13.2	8.7	38.9 (+1.9,-3.3)
U44-75-S5	640	3.0 > t > 2.5	64	0	33	3	0	7.0	13.6	9.2	39.7 (+0.8,-0.9)
U44-75-S8	635	3.0 > t > 2.5	52	0	45	3	0	5.4	9.1	3.2	38.8 (+1.1,-3.6)
U44-750-60	750	60	77	1	16	6	0	NA	NA	NA	35.0 (+2.1,-2.4)
U54-HEAD	none	none	28	0	70	2	0	NA	NA	NA	39.9 (+3.7,-3.8)
U54-87-AVG	665	3.0	63*	0*	35*	2*	0*	7.2*	12.9*	8.7*	39.4 (+1.8,-1.7)*
U54-750-60	750	60	75	3	16	6	0	NA	NA	NA	39.3 (+1.8,-1.5)
U23-HEAD	none	none	19	0	81	0	0	NA	NA	NA	35.5 (+2.8,-2.8)
U23-42-S1*	665	3.0	61	0	39	0	0	8.0	10.0	11.8	39.0 (+2.9,-2.3)*
U23-43-S1	685	2.4	63	0	37	0	0	8.1	9.9	12.2	39.3 (+4.1,-3.3)
U23-45-S1	665	3	61	0	39	0	0	7.9	10	11.6	38.0 (+2.5,-2.1)
U23-700-60	700	60	66	4	30	0	0	7.9	7.7	8.7	38.6 (+3.2,-3.6)
U23-750-60	750	60	67	11	22	0	0	7.5	7.5	8.0	39.3 (+3.0,-2.3)
U57-HEAD	none	none	28	0	72	0	0	NA	NA	NA	35.7 (+2.2,-2.7)
U57-88-AVG	665	3.0	64*	0*	34*	2*	0*	7.2*	14.1*	10.1*	34.1 (+3.0,-2.4)*
U57-750-60	750	60	78	4	11	3	4	NA	NA	NA	33.3 (+0.9,-1.0)
U58-HEAD	none	none	6	0	94	0	0	NA	NA	NA	NA
U58-89-AVG	665	3.0	66*	0*	33*	1*	0*	7.0*	15.9*	9.8*	31.7 (+3.7,-3.2)*
U58-750-60	750	60	78	1	15	2	4	NA	NA	NA	30.5 (+2.8,-1.8)

4.7.1 Crystallinity in the head material

The first trend appears when comparing the head samples. Note that XRD grainsize measurements were taken for all of the head samples that contained more than 19% crystalline phase. The XRD peaks were not well resolved from the amorphous background if less than ~20% crystalline phase precipitated during the quenching process, and therefore a mathematical fit of the data became increasingly difficult and inaccurate below this threshold. When comparing the magnetic properties of the samples annealed under standard annealing conditions (665°C, 3 min), with highly amorphous head samples (within a given alloy target composition), to the magnetic properties of the samples annealed under standard annealing conditions, with >20% crystalline phase in the head samples, a definite trend appears. The samples with >20% crystalline phase present in the head samples have lower intrinsic coercivities. Figure 4-4 shows the magnetic properties of the alloy annealed under standard annealing conditions (665°C, 3 min) for all of the alloys except N28. Note from Table 4-11 that the U44, U54, and U57 head samples contain 23%, 30%, and 28% crystalline phase respectively. Figure 4-4 clearly shows that all of these alloys have lower intrinsic coercivities than their highly amorphous counterparts within the same target composition. However, Tables 4-10 and 4-11 also show that the average grainsizes and phase distributions of all of the samples annealed under standard annealing conditions within a target composition do not vary significantly. This point is reinforced by Figures 4-5 and 4-6 which show the average measured grainsizes of the alloys annealed under standard annealing conditions, and the phase distributions of the alloys annealed under standard annealing conditions respectively. Although there seems to be a direct correlation between the amount of crystalline phase present in the head samples and the intrinsic coercivities of samples annealed under standard annealing

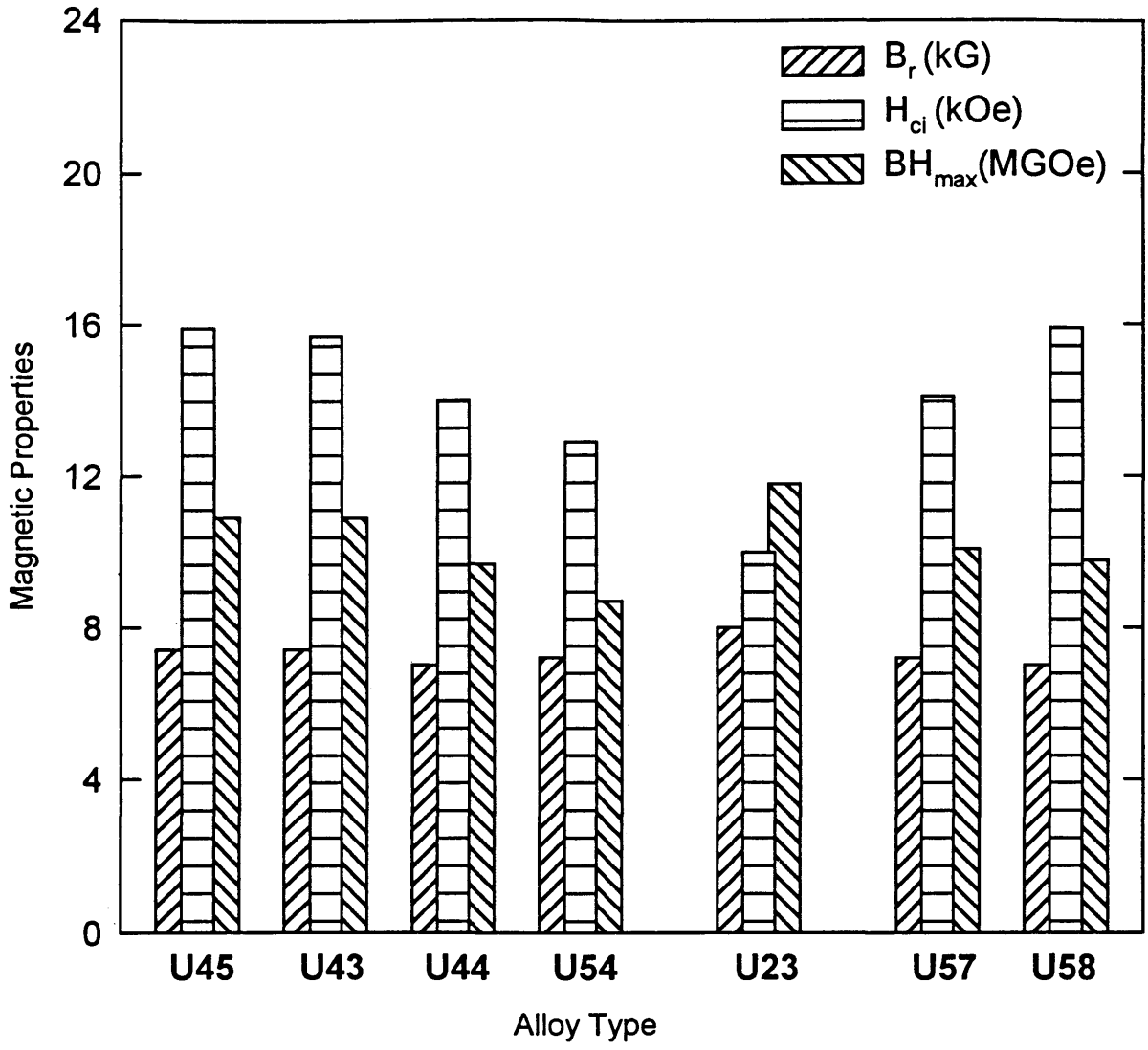

Figure 4-4: Magnetic properties for alloys annealed under standard annealing conditions (665°C, 3 min).

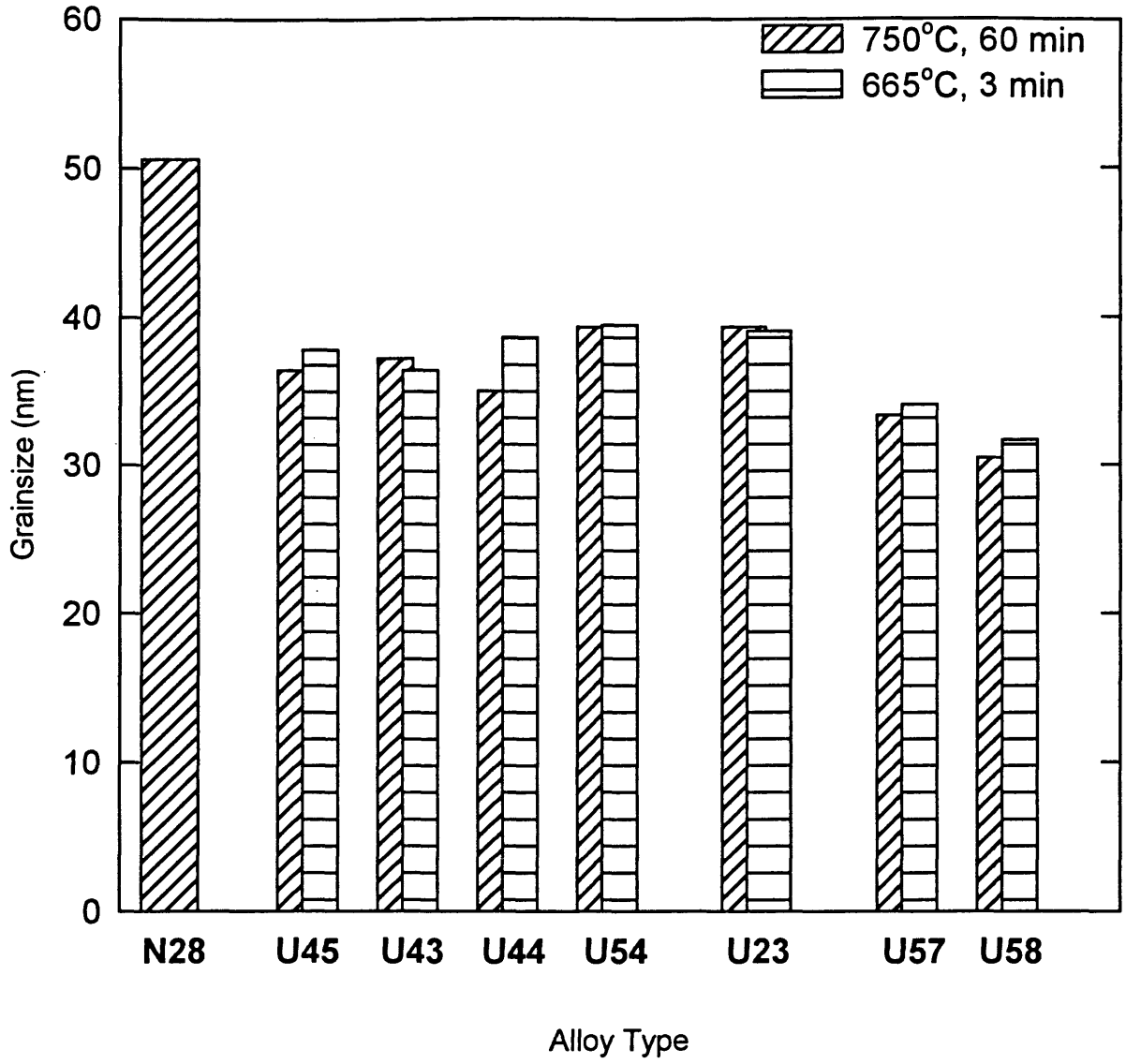

Figure 4-5: Grainsizes measured for all the alloys in the study. This plot shows the average grainsizes for the samples annealed under standard annealing conditions, and at 750°C for 1 hour.

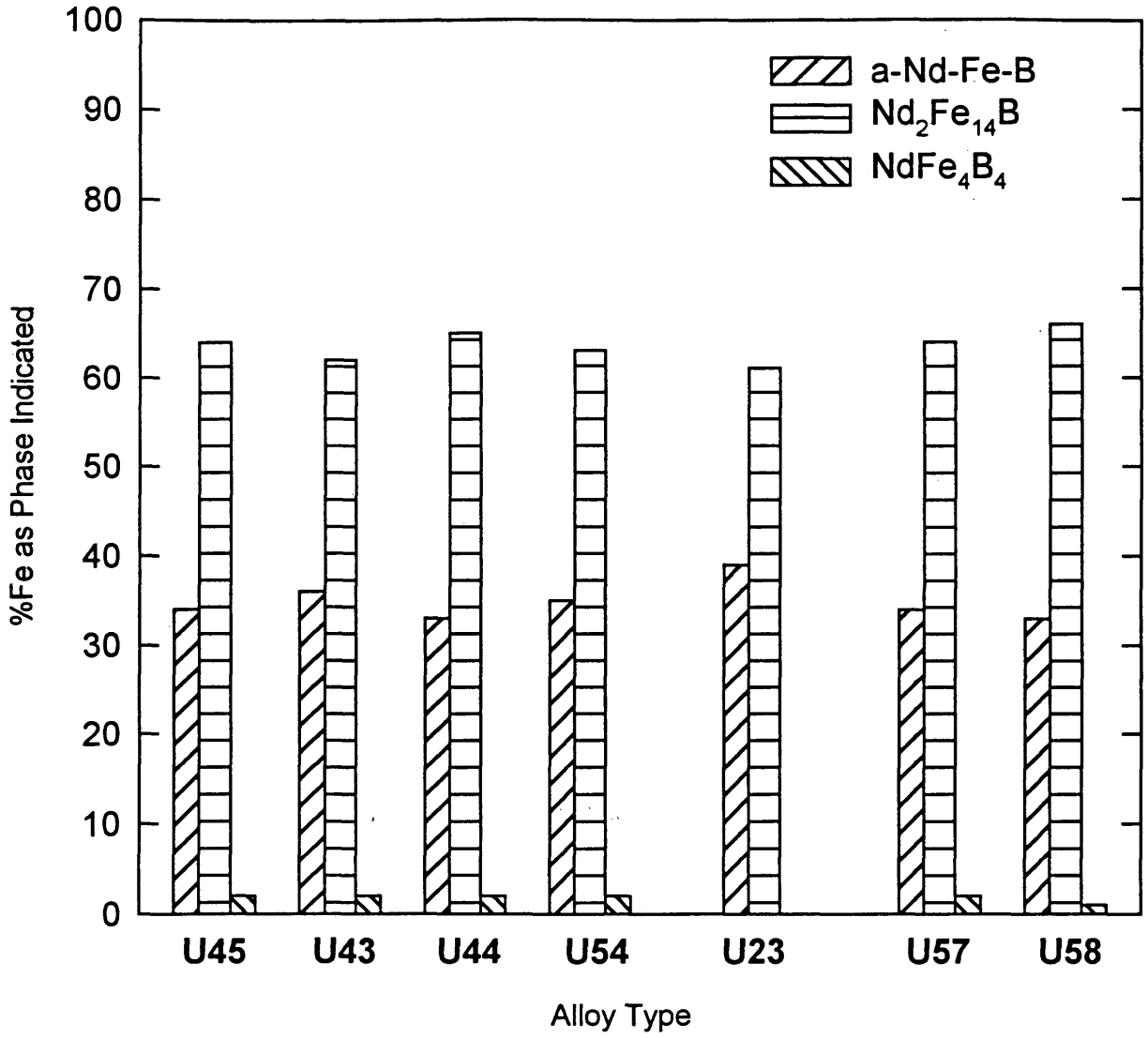

Figure 4-6: Phase distributions of alloys annealed under standard annealing conditions (665°C, 3 min).

conditions (665°C, 3 min), there are no apparent correlations between the magnetic properties and the measured grainsizes or phase distributions of the samples annealed under standard annealing conditions.

It is interesting to note that the U23-HEAD sample also contained 19% crystalline phase. Please remember that the U23 alloy's composition differed in two significant ways. First, U23 used only titanium additions to inhibit grain growth. Second, the rare earth content of the U23 alloy was leaner, and therefore, U23 was richer in iron. Note that no other alloys were examined in with this target composition. The intrinsic coercivities (H_{ci}) measured on the U23 alloy series were less than satisfactory, however this alloy did show higher remanence values (B_r) than the other alloys examined. It is possible that if the amount of crystalline 2-14-1 present in the head sample was reduced with a better quench, then the intrinsic coercivity of this target composition may improve while the remanence remained high, perhaps making the U23 alloy composition the most marketable.

4.7.2 Amorphous phase

Tables 4-10 and 4-11 clearly show that with the exception of the N28 samples annealed at high temperatures for long periods of time, the Mössbauer results indicate that all of the alloys examined contained at least 10-15% retained amorphous phase (Nd-Fe-B). Note that the N28 composition lies closest to the stoichiometric $Nd_2Fe_{14}B$ composition of all the compositions examined (see Figure 1-7). It is very surprising that the metastable amorphous precursor was not completely crystallized even in extreme annealing conditions. Two questions immediately come to mind. First, are the Mössbauer results accurate? Second, if the Mössbauer results are accurate why doesn't the amorphous precursor crystallize?

Several other authors have reported the presence of a retained amorphous phase. With a high resolution SEM and TEM analysis, Pamyatnykh et al [25] reported seeing a regular and fine substructure consisting of small grains about 30-50 nm in size separated by amorphous interlayers of 3-5 nm width. While examining an alloy with a composition ($Nd_{14.7}Fe_{77.45}Al_{0.15}B_{7.7}$), Spassov [26] reported finding a microstructure composed of microcrystals of $Nd_2Fe_{14}B$ with a Nd-rich amorphous phase between them. During a TEM analysis of samples of an $Fe_{90}Nd_7B_3$ amorphous alloy annealed for 3 minutes at 650°C, Inoue et al [27] discovered very fine crystallites with particle sizes 20 to 50 nm surrounded by a residual amorphous phase with a thickness of about 5 to 30 nm. Two independent studies directly related to this research effort support the Mössbauer results showing a large phase fraction of retained amorphous phase. First, Archambault [22,24] in France conducted a study in which x-ray diffraction was performed on samples with differing amounts of pure crystalline $Nd_2Fe_{14}B$ powder mechanically mixed with amorphous powder. This study concluded that a fraction of amorphous phase less than 30% is hard to detect in x-ray diffraction patterns. Therefore, the lack of a large amorphous background in the patterns of the powders studied for this thesis is not evidence that the retained amorphous phase does not exist. Second, Dr. Williamson, an expert in Mössbauer spectroscopy, made an extensive effort at the Colorado School of Mines to fit the Mössbauer spectrum of the U57-88-S1 sample without allowing for an amorphous phase. Note that Table 4-8 shows that sample U57-88-S1 has 34% of the iron reporting to the amorphous phase. The alloys examined in this study do not have a stoichiometric $Nd_2Fe_{14}B$ composition. The alloying additions of lanthanum, cobalt, and refractory metals could alter the Mössbauer patterns significantly by altering the hyperfine interactions of the Fe^{57} atoms. Using this philosophy, an attempt was made to alter the hyperfine parameters of the crystalline phases known to be present in the U57-88-S1 sample for the

mathematical fitting in a way that would eliminate the need for an amorphous phase. However, if the amorphous phase was eliminated from the fitting all together, the statistical fitting parameter χ^2 was driven to large numbers indicating poor quality fits. By allowing the parameters of the a magnetic residual phase to drift to their optimal numbers, the χ^2 reduced to its lowest value, but this fitting still indicated 27% of a residual magnetic phase present in the U57-88-S1 sample. It seems impossible to reasonably fit the Mössbauer spectra of this system without allowing for an additional phase that is magnetic but distinct from the 2-14-1 phase.

Why didn't this amorphous precursor crystallize? The first step in addressing this question is to define what the "amorphous" phase is. The powders examined are produced in a melt-spinning process, in which the molten alloy is quenched so rapidly that the diffusion required for crystallization from the homogenous liquid is arrested. Therefore, these powders start off as a metallic glass in which there is no long-range crystalline order. The "amorphous" precursor is a snapshot of the homogenous molten metal. During annealing, the thermal energy of the system is raised allowing diffusion to occur, and crystallization is initiated in the powder. The crystallites grow until boride precipitates and other defects, that impinge grain boundary motion, impede their growth, or the grain boundary network itself impinges further grain boundary motion. The growth of the crystallites is an ordering of the amorphous precursor into a regularly arranged crystal lattice with a specific composition. As the atoms required to generate the crystal lattice diffuse from the precursor to the growing 2-14-1 crystallites, the composition of the precursor is continually changing (unless the precursor composition is exactly 2-14-1).

Tables 4-12A and 4-12B were generated with mass balance calculations. Table 4-12A was generated assuming that all of the titanium and niobium additions precipitated TiB_2 and $NbB_{1.97}$ particles [28, 29, 30]. In Table 4-12B it

TABLE 4-12A: Results of Mass Balance Calculations to Determine Compositions of Amorphous Phases.

SAMPLE	IRON DISTRIBUTION (% Fe AS)					BORON(mol) IN BORIDES		AMORPHOUS MOL DISTRIBUTION			Nd_X-Fe_Y-B_Z		
	$Nd_2Fe_{14}B$	α-Fe	Nd-Fe-B	$NdFe_4B_4$	Fe_3B	B in TiB_2	B in $NbB_{1.97}$	Nd (mol)	Fe (mol)	B (mol)	X	Y	Z
N28-HEAD	10	4	86	0	0	0	0	10.7	70.6	5.0	2.1	14.1	1
N28-600-2	20	9	71	0	0	0	0	9.6	58.3	4.4	2.2	13.2	1
N28-600-4	34	7	59	0	0	0	0	7.9	48.4	3.6	2.2	13.4	1
N28-600-5.5	69	11	20	0	0	0	0	3.8	16.4	1.6	2.5	10.6	1
N28-600-7	81	11	8	0	0	0	0	2.4	6.6	0.9	2.8	7.7	1
N28-600-15	88	10	2	0	0	0	0	1.6	1.6	0.4	3.6	3.7	1
U54-HEAD	28	0	70	2	0	3.6	0	7.3	54.2	3.4	2.2	16.2	1
U54-87-AVG	63	0	35	2	0	3.6	0	3.4	27.1	1.4	2.4	19.1	1
U54-750-60	75	3	16	6	0	3.6	0	1.3	12.4	-2.4	NA	NA	NA
U23-HEAD	19	0	81	0	0	0	4.1	7.0	63.5	5.2	1.3	12.2	1
U23-42-S1*	61	0	39	0	0	0	4.1	2.3	30.6	2.8	0.8	10.7	1
U23-700-60	66	4	30	0	0	0	4.1	1.7	23.5	2.6	0.7	9.2	1
U23-750-60	67	11	22	0	0	0	4.1	1.6	17.2	2.5	0.6	6.9	1
U57-HEAD	28	0	72	0	0	2.2	2.0	7.7	55.3	4.6	2	12.1	1
U57-88-AVG	64	0	34	2	0	2.2	2.0	3.3	26.1	1.1	3	24.7	1
U57-750-60	78	4	11	3	4	2.2	2.0	1.6	11.5	-1.5	NA	NA	NA

TABLE 4-12B: Results of Mass Balance Calculations to Determine Compositions of Amorphous Phases.

SAMPLE	IRON DISTRIBUTION (% Fe AS)					BORON(mol) IN BORIDES		AMORPHOUS MOL DISTRIBUTION			Nd_X-Fe_Y-B_Z		
	$Nd_2Fe_{14}B$	α-Fe	Nd-Fe-B	$NdFe_4B_4$	Fe_3B	B in TiB	B in $NbB_{1.97}$	Nd (mol)	Fe (mol)	B (mol)	X	Y	Z
N28-HEAD	10	4	86	0	0	0	0	10.7	70.6	5.0	2.1	14.1	1
N28-600-2	20	9	71	0	0	0	0	9.6	58.3	4.4	2.2	13.2	1
N28-600-4	34	7	59	0	0	0	0	7.9	48.4	3.6	2.2	13.4	1
N28-600-5.5	69	11	20	0	0	0	0	3.8	16.4	1.6	2.5	10.6	1
N28-600-7	81	11	8	0	0	0	0	2.4	6.6	0.9	2.8	7.7	1
N28-600-15	88	10	2	0	0	0	0	1.6	1.6	0.4	3.6	3.7	1
U54-HEAD	28	0	70	2	0	1.8	0	7.3	54.2	5.1	1.4	10.5	1
U54-87-AVG	63	0	35	2	0	1.8	0	3.4	27.1	3.2	1.1	8.5	1
U54-750-60	75	3	16	6	0	1.8	0	1.3	12.4	-0.6	NA	NA	NA
U23-HEAD	19	0	81	0	0	0	4.1	7.0	63.5	5.2	1.3	12.2	1
U23-42-S1*	61	0	39	0	0	0	4.1	2.3	30.6	2.8	0.8	10.7	1
U23-700-60	66	4	30	0	0	0	4.1	1.7	23.5	2.6	0.7	9.2	1
U23-750-60	67	11	22	0	0	0	4.1	1.6	17.2	2.5	0.6	6.9	1
U57-HEAD	28	0	72	0	0	1.1	2.0	7.7	55.3	5.7	1	9.7	1
U57-88-AVG	64	0	34	2	0	1.1	2.0	3.3	26.1	2.2	2	12.0	1
U57-750-60	78	4	11	3	4	1.1	2.0	1.6	11.5	-0.4	NA	NA	NA

was assumed that the titanium additions formed TiB particles instead of TiB_2 precipitates [27]. Assuming the stoichiometries of the species reported in the tables are strictly adhered to, that the iron and cobalt and the neodymium and lanthanum behave identically in the matrix, and that no other species are present, the composition of the retained amorphous phase is tracked by the two tables. Note that in the N28 and U23 compositions, the residual composition becomes boron rich at long annealing times relative to 2-14-1. In the U54 and U57 compositions, the residual composition becomes boron poor. Boron is the glass-stabilizing element in these alloys. The amount of boron present in the residual phase should significantly affect the ability of the phase to maintain amorphous stability.

4.7.3 Determination of grain boundary thickness

Is this "retained amorphous phase" truly amorphous or is it the residual elements not consumed during crystallization residing in the disordered grain boundary regions? Remember that the powders examined have fine grainsizes on the order of 30 nm to 40 nm. Therefore, there is a considerable amount of grain boundary volume in the matrix. The following sample derivation shows how the grain boundary thickness required to contain 30 percent of the total volume as amorphous phase on the grain boundaries was calculated:

Assumptions for Calculations:

- Grain boundary region is represented by volume external to hexagonal prisms spaced in a hexagonal array
- Grains are perfectly ordered 6-sided polygons
- The cross sectional depth is a constant thickness, d
- If 30% of the total volume is contained in the grain

boundary region, then 15% is contained in the area between the dashed region and the solid hexagon, since all boundaries are shared

- Grainsize = 30 nm

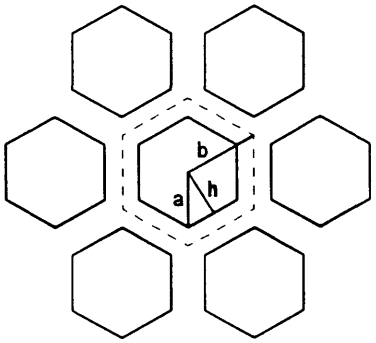

Grain Size = 30nm=2a
a=15nm

Calculating Area of Polygon:

$\sin 60^\circ = h/a$

$h = a \sin(60)$

Area = $A = 6\ (1/2)Bh$

$A = (3)Bh$

$A = (3)\ a\ [a \sin(60)]$

$A = (3)\ a^2 \sin(60)$

Calculating grain boundary thickness (t) to maintain 30% residual phase grain boundary fraction:

$$0.15 = \frac{[\text{Volume of Dashed Polygon}] - [\text{Volume of Small Polygon}]}{[\text{Volume of Dashed Polygon}]}$$

$$0.15 = \frac{[d\ (3)\ b^2 \sin(60)] - [d\ (3)\ a^2 \sin(60)]}{[d\ (3)\ b^2 \sin(60)]}$$

$$0.15 = \frac{[b^2] - [a^2]}{[b^2]}$$

$$0.15 = \frac{[b^2] - [(15nm)^2]}{[b^2]}$$

$(0.85)\, b^2 = (15)^2$

$b = 16.3$ nm

Note: $h_1 = a \sin(60)$, $h_2 = b \sin(60)$

Thickness = $t = h_2 - h_1$

$t = b \sin(60) - a \sin(60)$

$t = (16.3 \text{ nm}) \sin(60) - (15 \text{ nm}) \sin(60)$

$t = 14.09 \text{ nm} - 12.99 \text{ nm}$

$t = 1.10$ nm

Total Grain Boundary Thickness = 2t = 2.20 nm

Table 4-13 shows the results of calculations performed to determine the grain boundary thickness required to contain 16 to 30 percent of the total matrix volume on the grain boundaries of 6 sided polyhedron grains with 30 to 40 nm grainsizes. Considering that the unit cell of the $Nd_2Fe_{14}B$ phase is 1.2 nm long

TABLE 4-13: Results of Grain Boundary Thickness Calculations.

Grainsize (nm)	Volume % of Grain Boundary	Grain Boundary Thickness (nm)
30	16	1.11
30	30	2.20
40	16	1.47
40	30	2.93

on the c-axis, the grain boundary thickness values reported in Table 4-13 seem quite plausible. It is therefore suggested that the "retained amorphous phase" is

not amorphous, but instead is a disordered grain boundary phase composed of the residual elements not consumed during crystallite growth.

4.7.4 Precipitation of refractory metal borides

The refractory metals titanium and niobium were added to this alloy system to inhibit grain growth and increase intrinsic coercivity by the precipitation of refractory metal borides. Magnetic theory predicts that enhanced remanence occurs as the grainsize of the $Nd_2Fe_{14}B$ crystals approaches the size of a single magnetic domain. The enhanced remanence should be achieved in a nanocrystal-like structure with a mean grainsize less than 30 nm [4]. A distribution of refractory metal borides throughout the microstructure could act to pin grain boundaries, and therefore inhibit grain growth. Coercivity is the resistivity of the microstructure to form reverse domains when a magnetic field is applied in the reverse direction of the existing domain alignment. Reverse domains are nucleated at grain boundaries and grow in the same manner as grains. Precipitates that act to pin grain boundaries also pin domain walls, and therefore increase the intrinsic coercivity of the microstructure.

The advantages to a distribution of borides in the microstructure are clear, but two critical questions need to be asked. Are refractory metal borides precipitated in this system? If borides are precipitated in this system, when are they precipitated? The first indication that the grain boundaries are being pinned is shown in Tables 4-10 and Tables 4-11. Only the N28 composition did not contain refractory metal additions, and only the N28 samples showed grain growth during annealing as well as a larger final grain size than all of the other samples. Figure 4-7 shows the relative thermodynamic stability of several different borides by plotting the standard free energy of formation (ΔG°_f) of the borides as a function of temperature. It is clear from Figure 4-7 that both niobium

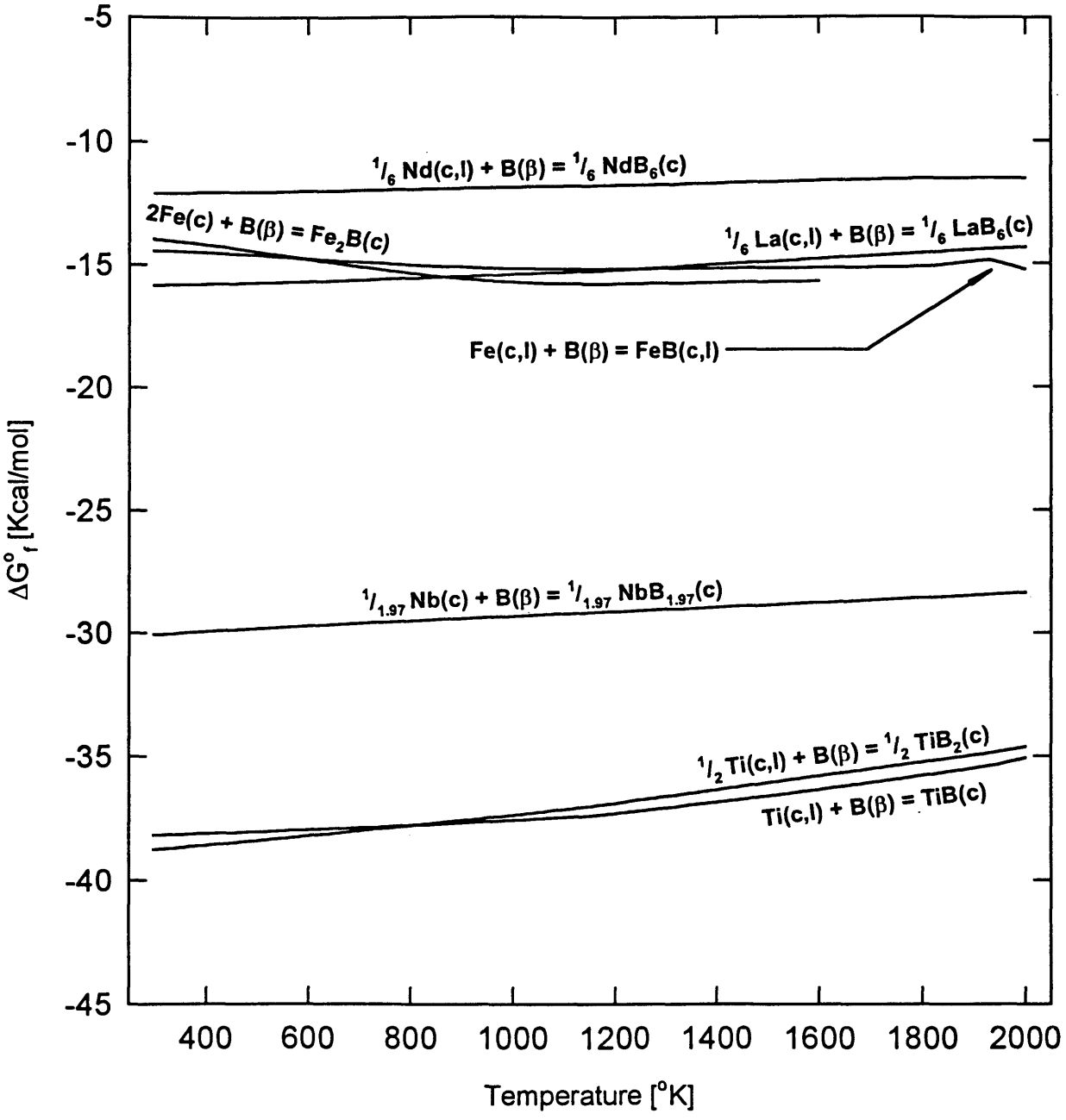

Figure 4-7: Ellingham diagram showing the standard free energy of formation (ΔG°_{f}) as a function of temperature for several boride species.

and titanium form borides that are much more stable than the rare-earth and iron borides. Figures 4-8, 4-9, and 4-10 show the free energy (ΔG) for the precipitation of niobium and titanium borides for the three different compositions U23, U45, and U57 (respectively) as a function of temperature. The free energy of precipitation was calculated in the following way:

$$Ti\ (c,l) + 2B\ (\beta) = TiB_2\ (c) \qquad \textbf{[4.2]}$$

$$\Delta G = \Delta G^o + RT\ln(Q) \qquad \textbf{[4.3]}$$

where in this case:

$$Q = \frac{[A(TiB_2)]}{[A(Ti)][A(B)]^2} \qquad \textbf{[4-4]}$$

- The activity of the titanium boride, $A(TiB_2)$, was assumed to be 1 since the calculation is for the purpose of determining whether TiB_2 precipitates.
- The activities of the reactants were assumed to be Raoultian and calculated in the following way:

$$A(Ti) = \gamma_{Ti} X_{Ti} \qquad \textbf{[4.5]}$$
$$A(B) = \gamma_B X_B \qquad \textbf{[4.6]}$$

where:

γ = activity coefficient of species
X = mole fraction of species

Two lines are plotted for each precipitation equation in Figures 4-8, 4-9, and 4-10. The solid lines in these figures show the ΔG calculated assuming that the activity coefficients (γ) are the activity coefficients of the reactant species in the limit of infinite dilution (γ^o). The solid lines represent the upper limit to free energy calculations. In actuality, there is between 1 and 2 atomic percent refractory

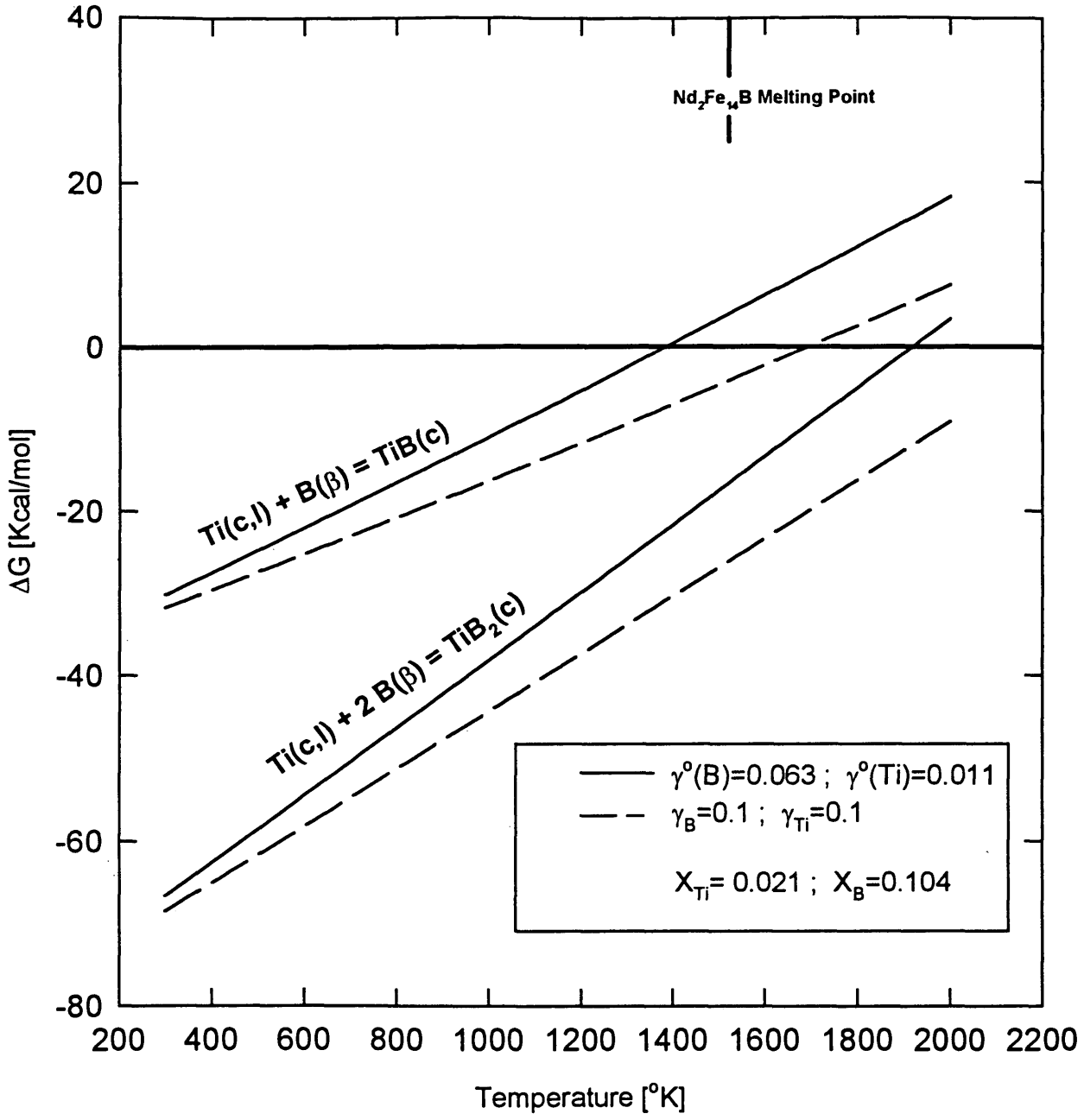

Figure 4-8: Thermodynamic driving force (ΔG) for the precipitation of titanium borides in the U23 alloy as a function of temperature.

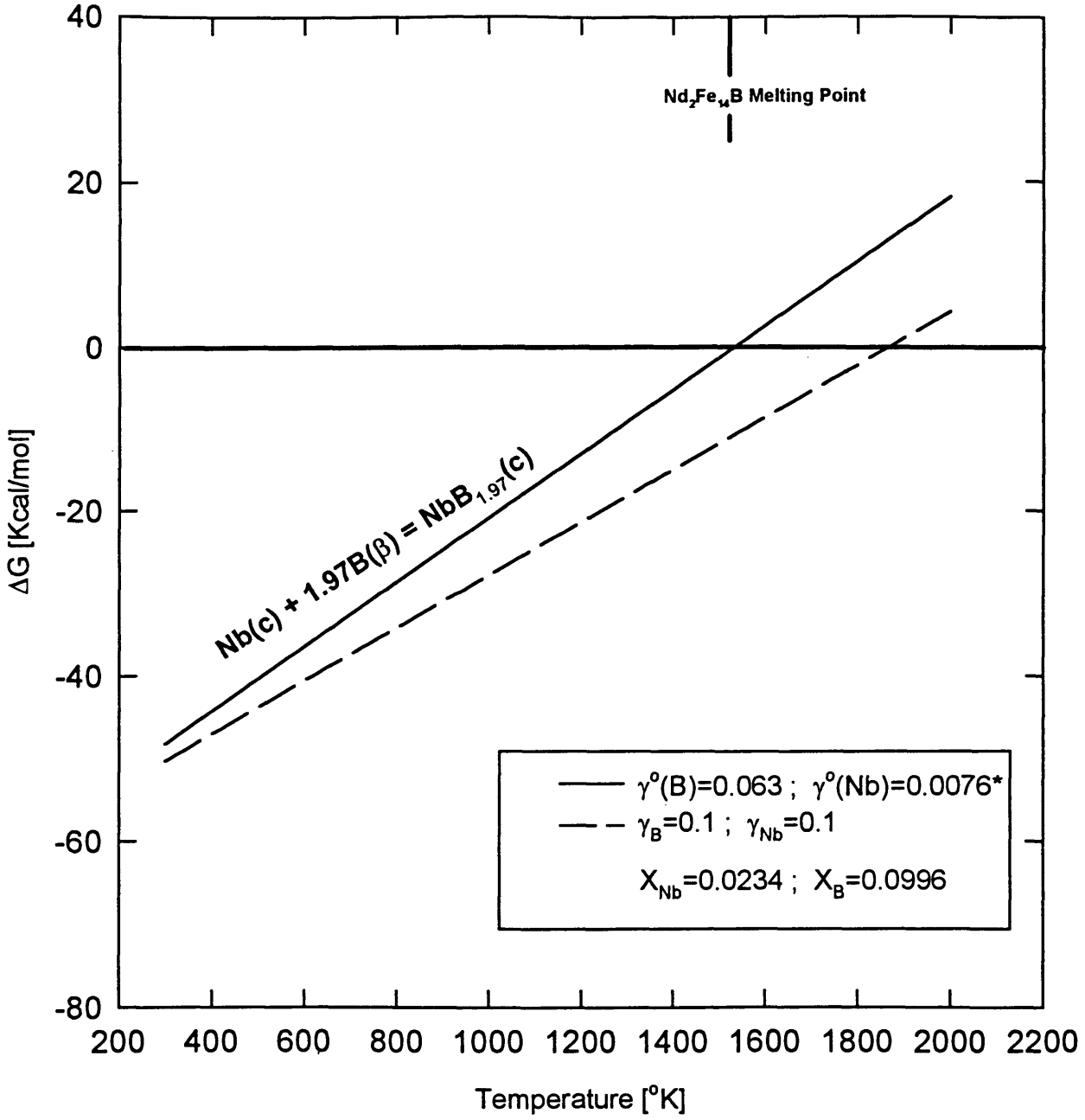

Figure 4-9: Thermodynamic driving force (ΔG) for the precipitation of niobium boride in the U45 alloy as a function of temperature.

* The activity coefficient γ^0 for Nb in Fe was unknown and approximated with Zr

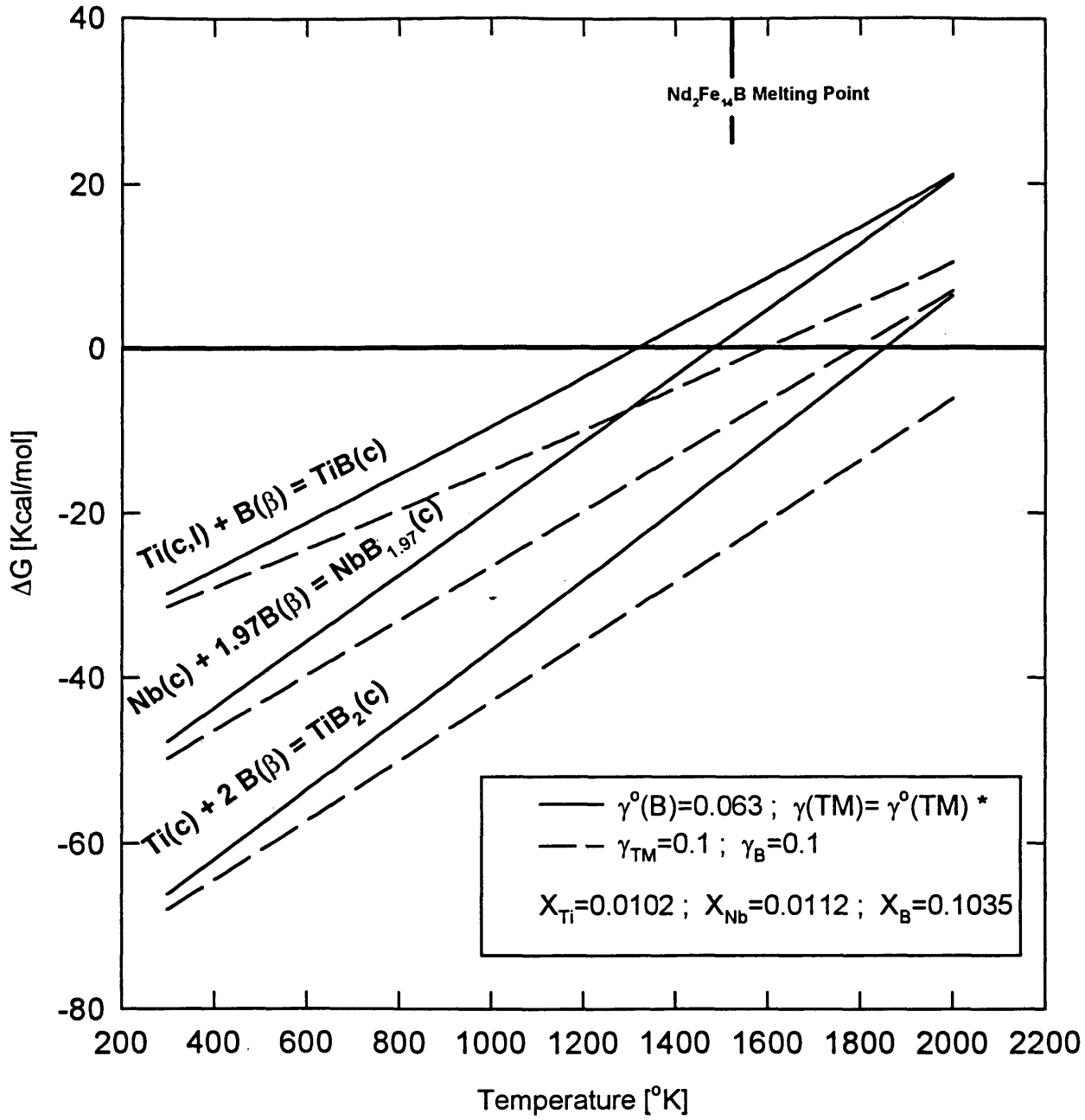

Figure 4-10: Thermodynamic driving force (ΔG) for the precipitation of both titanium borides and niobium borides in the U57 alloy as a function of temperature.

* TM stands for Transition Metal: γ_{Ti}°=0.011 ; γ_{Nb}°=0.0076**

** The activity coefficient γ° for Nb in Fe was unknown and approximated with Zr

metal addition and approximately 10 atomic percent boron addition to the alloys examined. Therefore, the activity coefficients of the species examined most likely lie outside of the Henrian activity regime and are greater than the γ^o values. The dashed lines in Figures 4-8, 4-9, and 4-10 show the ΔG calculated assuming higher activity coefficients at 0.1, and probably represent more realistic values. It is interesting to note that the free energy of precipitation values stay negative at temperatures above the melting point of $Nd_2Fe_{14}B$. This result suggests that refractory metal borides do precipitate, and that possibly these borides precipitate in the melt before the alloy is cast onto the melt-spinner. If the borides do precipitate in the melt, and assuming that the borides precipitate to a standard size and are homogeneously distributed throughout the melt, then an even distribution of refractory metal borides would exist in the powders before the annealing process. This would suggest that the ultimate grainsize achieved in given alloy with refractory metal additions is determined by the composition and distribution of the refractory metal borides before annealing even starts.

4.7.5 Comparison of grainsize results

Several interesting results are illuminated when the grainsizes of the alloys studied are compared. Remember that Figure 4-1 demonstrated that the N28 alloy which did not include any refractory metal additions showed a steady grain growth up to approximately 50 nm and then no further growth independent of annealing time or temperature. Tables 4-10 and 4-11 show that in the alloys which included refractory metal additions, all of the annealed samples for a given composition yielded approximately the same average grainsize independent of annealing time or temperature, and further that all of the average grainsizes were on the order of 30-40 nm. These results suggest that the refractory metal additions were successful at impinging grain growth and reducing the average

grainsize.

Figure 4-5 depicts the average grainsizes for each of the alloy samples annealed under standard annealing conditions (665°C, 3 min), and for the samples annealed at 750°C for 60 minutes. Note that all the alloys with the same nominal composition have been grouped together. It is interesting to note that the U45 nominal composition series and the U23 nominal composition alloy have approximately the same grainsizes of 36-40 nm, while the U57 nominal composition series shows a smaller average grainsize of 30-34 nm. Remember that the U45 nominal composition series contains 2% niobium additions, the U23 alloy contains 2% titanium additions, and the U57 nominal composition series contains 1% niobium and 1% titanium additions.

Why did the U57 and U58 alloys show a finer grainsize? The U57 and U58 alloys contained both niobium and titanium additions. The finer grainsize might be explained by a difference in size and shape between the titanium borides and niobium borides precipitated. Differently shaped particles could act to pin the grain boundaries in different ways. With the two differently shaped particles acting in concert, a more effective overall grain boundary pinning may be achieved. If the grain boundary pinning precipitates are not formed in the melt as previously suggested, and instead are precipitated during annealing, then there may be different preferential precipitation locations within the microstructure for the two different borides. Again the two borides acting in concert may be more effective then one type of boride acting alone to prevent grain growth. It may also be significant to note that 1% titanium and niobium additions were made to the U57 and U58 alloys instead of the 2% additions made to the U45-U54 composition series and U23 alloys. Smaller quantity additions may result in the precipitation of finer borides either in the melt or during annealing. A finer boride distribution could result in a finer grainsize.

Tables 4-10 and 4-11 show one other interesting grainsize effect. Note that in

the U54-HEAD sample and the U57-HEAD sample the measured grainsize is approximately the same as in the annealed samples of these two series respectively. The grainsize of the crystals formed during quenching is the same as the grainsize of the crystals formed during annealing. This suggests that the same borides that act to retard grain growth during annealing act to retard grain growth during quenching, indicating that the refractory metal borides are already present during quenching because they were formed in the melt. It is true that the U44-HEAD sample and the U23-HEAD sample have finer grainsizes than their annealed counterparts, but this does not refute the previous theory. There is no recorded thermal history of these quenches. The quenches in the U44 and U23 series may have been more severe, therefore not allowing the crystallites formed adequate time to grow to their full potential. Note that the U44 and U23 head samples contained only 23% and 19% crystalline 2-14-1 respectively, while the U54 and U57 head samples both contained 28% crystalline 2-14-1. The smaller amount of crystalline material in the U44 and U23 head samples does indicate a more severe quench.

4.7.6 The precipitation of different phases in different alloys

During the examination of the four different nominal compositions, five different iron-containing phases were detected by Mössbauer spectroscopy and confirmed by x-ray diffraction. Not all five phases were detected in every alloy composition examined. Tables 4-10 and 4-11 show the phases detected for each alloy sample investigated. In Figure 4-6 the phase distributions of the samples annealed at 665°C for 3 minutes are shown, and in Figure 4-11 the phase distributions of the samples annealed at 750°C for 60 minutes are shown.

Note that the U23 sample annealed at 665°C for 3 minutes was the only sample that did not show any formation of $NdFe_4B_4$. It is also interesting that the

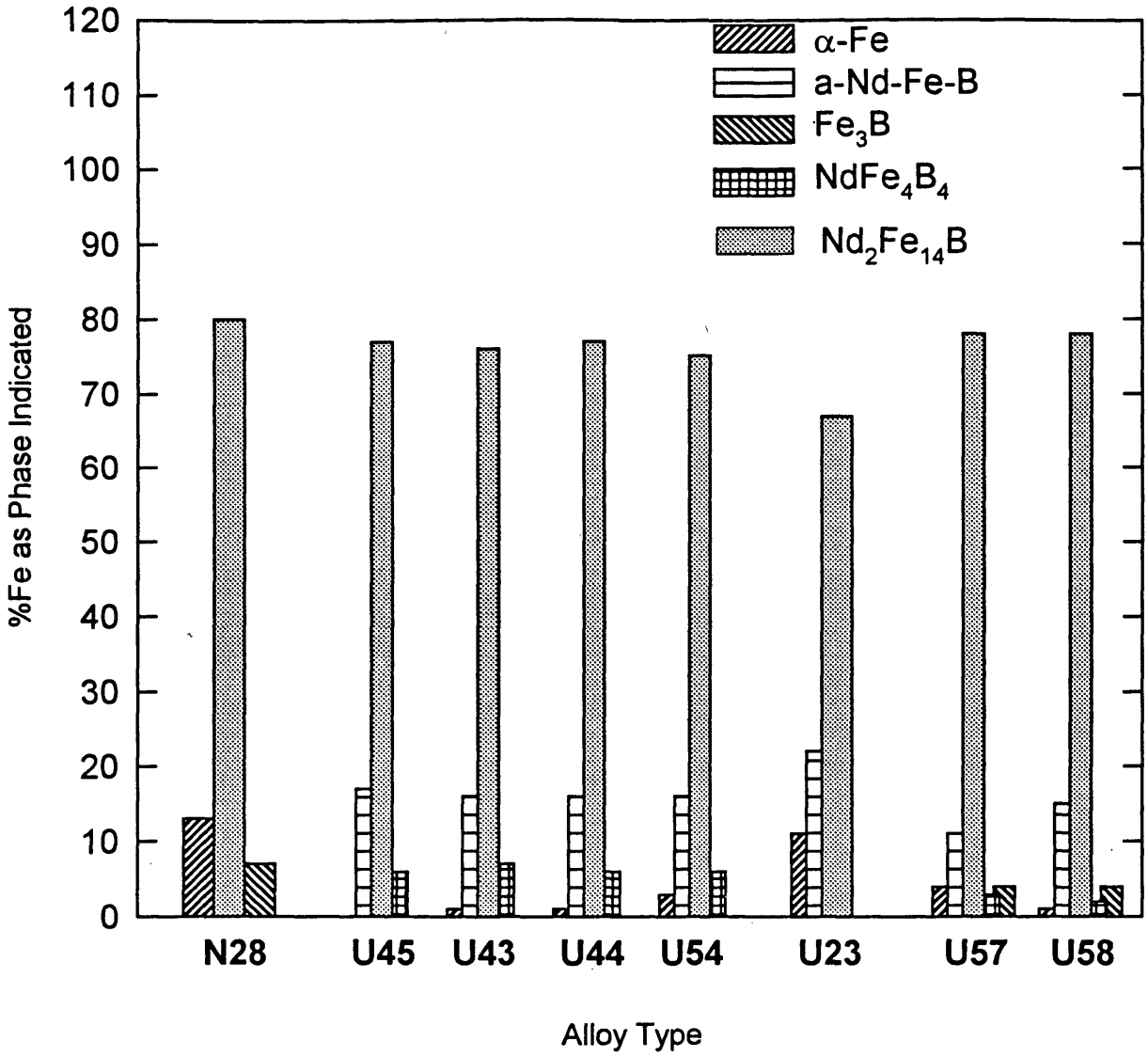

Figure 4-11: Phase distributions of all alloys studied annealed at 750°C for 1 hour.

U23 sample annealed at 750°C for 60 minutes did not precipitate any $NdFe_4B_4$ either. $NdFe_4B_4$ is a potential bad actor in these alloys because it is non-magnetic. Exchange coupling theory predicts that a composite of soft and hard magnetic material may produce the optimal magnetic energy fields. For optimum coercivity, the soft regions should have dimensions of the order of a domain wall width of the hard phase δ_W, which is 3-4 nm, similar to the exchange length l_{ex} in both hard and soft phases [2]. If a nonmagnetic phase is present it could drop both coercivity and remanence in the powder.

Why didn't the U23 alloy precipitate any $NdFe_4B_4$ phase? When looking at the nominal compositions displayed in Table 4-1, the U23 alloy does not differ significantly from the U45 or U57 compositions. The U23 does have 2% less Nd+La and 2% more Fe+Co. The slightly higher (Fe+Co)/(Nd+La) ratio may have prevented the precipitation of the $NdFe_4B_4$ phase. But the primary difference between the U23 alloy and the U45 and U57 compositions lies in the refractory metal addition; the U23 alloy contains 2% titanium and no niobium. Does the titanium addition inhibit the formation of the $NdFe_4B_4$ phase? The U57 alloy also contains 1% titanium additions, and it precipitated significant amounts of $NdFe_4B_4$. Does the niobium addition promote the formation of $NdFe_4B_4$? All of the alloys that contained niobium additions precipitated $NdFe_4B_4$, while the N28 alloy and the U23 alloy which do not contain niobium additions did not precipitate $NdFe_4B_4$. Other authors have indicated that niobium additions promote the formation of the $NdFe_4B_4$ phase [31].

Note that both Figures 4-6 and 4-11 show that approximately the same amount of $Nd_2Fe_{14}B$ precipitated in all the compositions examined, except the U23 sample. The U23 sample shows less $Nd_2Fe_{14}B$ precipitation and a corresponding larger phase fraction of the residual amorphous or grain boundary phase retained. The U23 sample also precipitated a significant phase fraction of α-Fe in the sample annealed at 750°C for 60 minutes.

In the samples annealed at 750°C for 60 minutes, Fe_3B was only precipitated in the N28 alloy and the U57 alloy composition. It is interesting to note that the N28 alloy did not contain any refractory metal additions, and that the U57 nominal composition series contained only 1% additions each of titanium and niobium, instead of the 2% additions contained in the other alloy series. It is not clear if either refractory metal inhibits Fe_3B precipitation, and if one of the additions does inhibit Fe_3B formation, it is not clear which one. Is it possible that large additions of either titanium and/or niobium metal, in excess of 2%, inhibits the formation of the Fe_3B phase? If a larger quantity of refractory metal raises the activation energy barrier for the precipitation of Fe_3B, then higher annealing temperatures may precipitate the Fe_3B in the alloy compositions that did not precipitate Fe_3B in this study.

Chapter 5

CONCLUSIONS

5.1 Research Summary

The purpose of this study was to use Mössbauer spectroscopy and x-ray diffraction to characterize the microstructures of rare earth nano-structured magnetic alloy powders doped with various refractory metal additions, and thereby correlate the powders' magnetic properties with composition and processing conditions. Eight Nd-Fe-B alloys with four different nominal compositions were examined. The alloys in the as-received condition were rapidly quenched powders with a microstructure composed mostly of an amorphous matrix. Annealing experiments were performed at the Colorado School of Mines to crystallize the metastable amorphous precursor into a nano-scale matrix of $Nd_2Fe_{14}B$ crystallites for hard magnetic applications. The as-quenched and annealed samples were characterized with ^{57}Fe Mössbauer spectroscopy and x-ray diffraction. Mössbauer spectroscopy was used to determine the iron-containing phase composition and distribution in the samples. Using the Scherrer equation and x-ray diffraction line broadening, a technique was developed and applied to determine the grainsizes of the alloy samples' $Nd_2Fe_{14}B$ crystallites. X-ray diffraction was also used to confirm the phase distributions reported by the Mössbauer spectroscopy, and to detect any non iron-containing phases present in the matrix.

5.2 Usefulness of Mössbauer Spectroscopy

^{57}Fe Mössbauer spectroscopy was successfully used to identify several different phases in the powder samples examined. One drawback to Mössbauer spectroscopy is that only iron-containing phases can be detected. However, the compositions of the alloys investigated all lie in the iron rich corner of the Nd-Fe-B ternary phase diagram, and therefore, almost every phase precipitated should contain iron. The phase distribution precipitated in a sample is directly related to the heat-treating schedule that the sample experienced. The magnetic properties of the powder samples seem to be heavily dependent on the annealing scenario used, maybe more so than on the compositions of the samples. However, two samples with similar phase distributions as reported by Mössbauer spectroscopy may have significantly different magnetic properties. All of the annealed U43 samples showed similar phase distributions, and yet the intrinsic coercivities varied significantly. This is probably due to morphological differences that would only be detected by a high resolution TEM analysis. Nevertheless, Mössbauer spectroscopy is very successful at detecting small quantities of either non-magnetic iron containing phases like $NdFe_4B_4$ which may be bad actors in the magnetic matrix, or other iron-containing phases which may impede magnetic performance (α-Fe). In addition, Mössbauer spectroscopy does an excellent job of detecting small quantities of residual amorphous or disordered phase which would not be detected by x-ray diffraction, and which may be critical to magnetic performance. Mössbauer spectroscopy is an excellent tool to investigate highly amorphous samples. Highly amorphous samples are hard to analyze quantitatively with x-ray diffraction. With a small crystalline fraction diffracting, the peak intensities are weak and the signal to noise ratio is smaller, therefore accurate quantitative analysis is difficult.

The Mössbauer analysis of the phase distributions of head samples was critical to this study. The presence of 20-30% fraction of crystalline material in a

head sample has been directly correlated to poor magnetic performance in annealed samples. Figure 5-1 shows that there is an excellent correlation between the measured intrinsic coercivities of samples annealed at 665°C for 3 min, and the amount of crystalline material in the head samples. The U44 and U45 samples, which had the same nominal composition as the U43 and U45 samples, showed significantly inferior intrinsic coercivities, in samples, which experienced identical heat treatments. The phase distributions and grainsizes in the annealed samples of all these alloys were similar. In fact, Figure 5-2 clearly demonstrates that there is no relationship between the measured grainsizes and the H_{ci} values measured for the samples examined, but the same trend that appeared in Figure 5-1 appears again. The U44-HEAD and U54-HEAD samples contained 23% and 30% crystalline phase, while the U43-HEAD and U45-HEAD samples were 91% and 95% amorphous respectively. The Mössbauer spectra of the head samples were the best indication that the U44 and U54 powders might have poor magnetic properties after annealing. X-ray diffraction of the head samples would also indicate crystallinity, but less quantitatively. Figure 5-3 clearly shows that no correlation was determined between the amount of crystalline phase in the head samples and the remanences measured in samples annealed at 665°C, 3 min. In fact there was no correlation determined between any of the measured parameters and the remanence. Figure 5-4 shows the lack of correlation between the measured grainsizes, and the measured remanences.

5.3 X-ray Diffraction Effectiveness

As outlined in Chapter 3, a grainsize measuring technique was developed in cooperation between the Colorado School of Mines and a Rhodia laboratory in Paris. The technique depends on using x-ray diffraction peak line broadening and the Scherrer equation. Diffraction peak line broadening occurs in samples with a grainsize less than 100 nm. There are other sources of peak broadening.

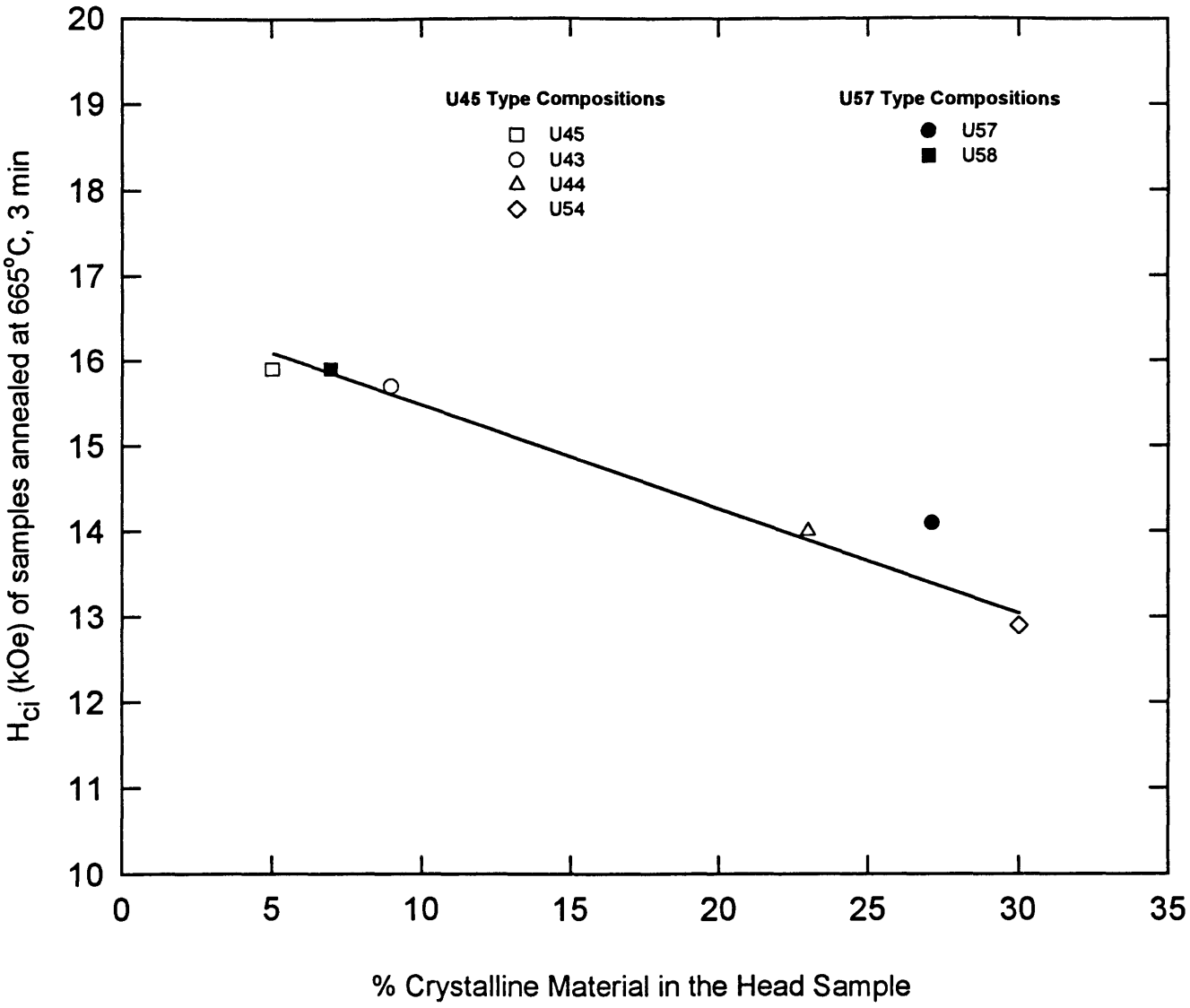

Figure 5-1: Intrinsic coercivity of samples annealed under standard annealing conditions (665°C, 3 min) as a function of the total crystallinity in the head sample.

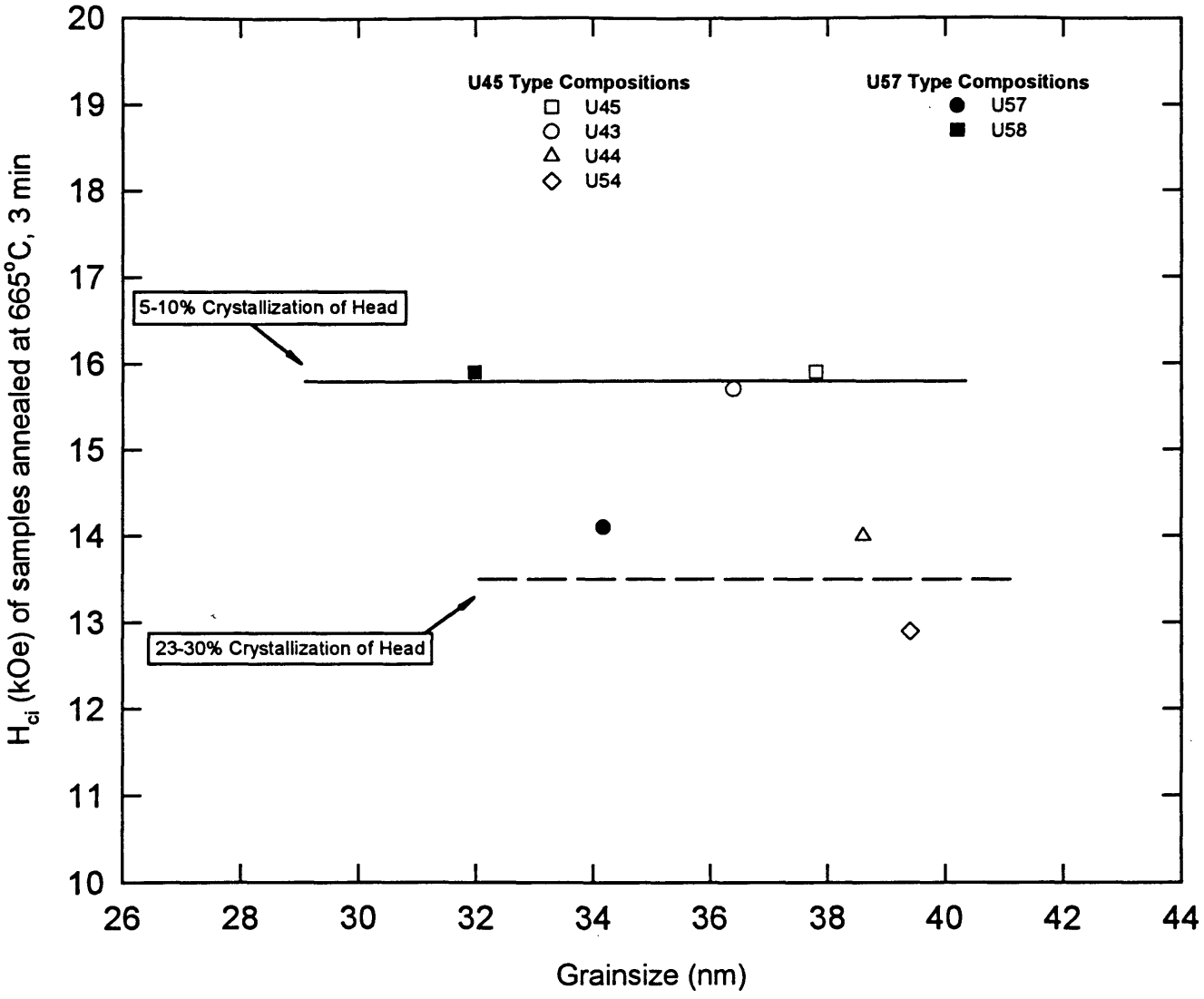

Figure 5-2: Intrinsic coercivity H_{ci} of samples annealed at 665°C for 3 min as a function of the measured grainsize.

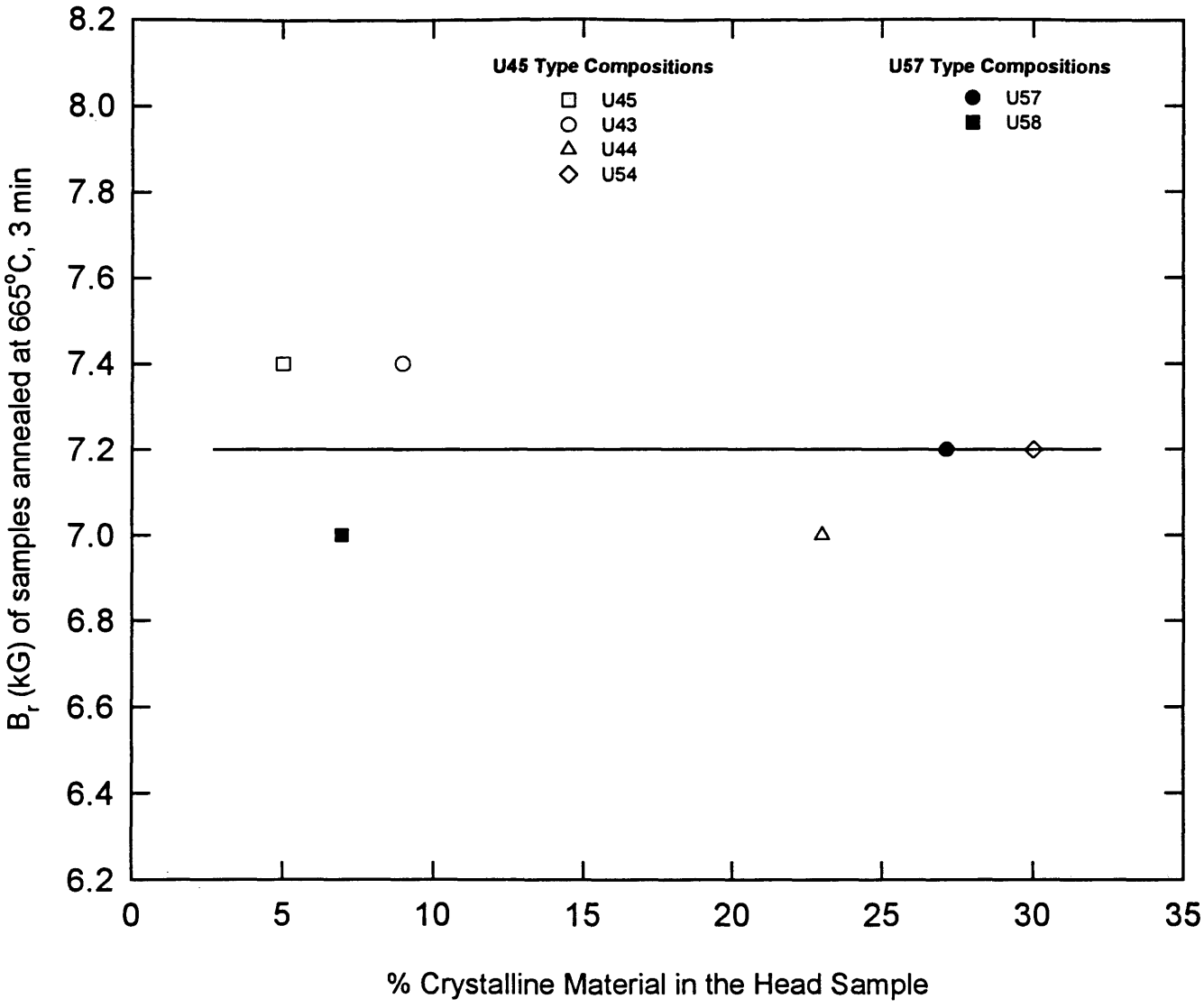

Figure 5-3: Remanence B_r of samples annealed under standard annealing conditions (665°C, 3 min) as a function of the total crystallinity in the head sample.

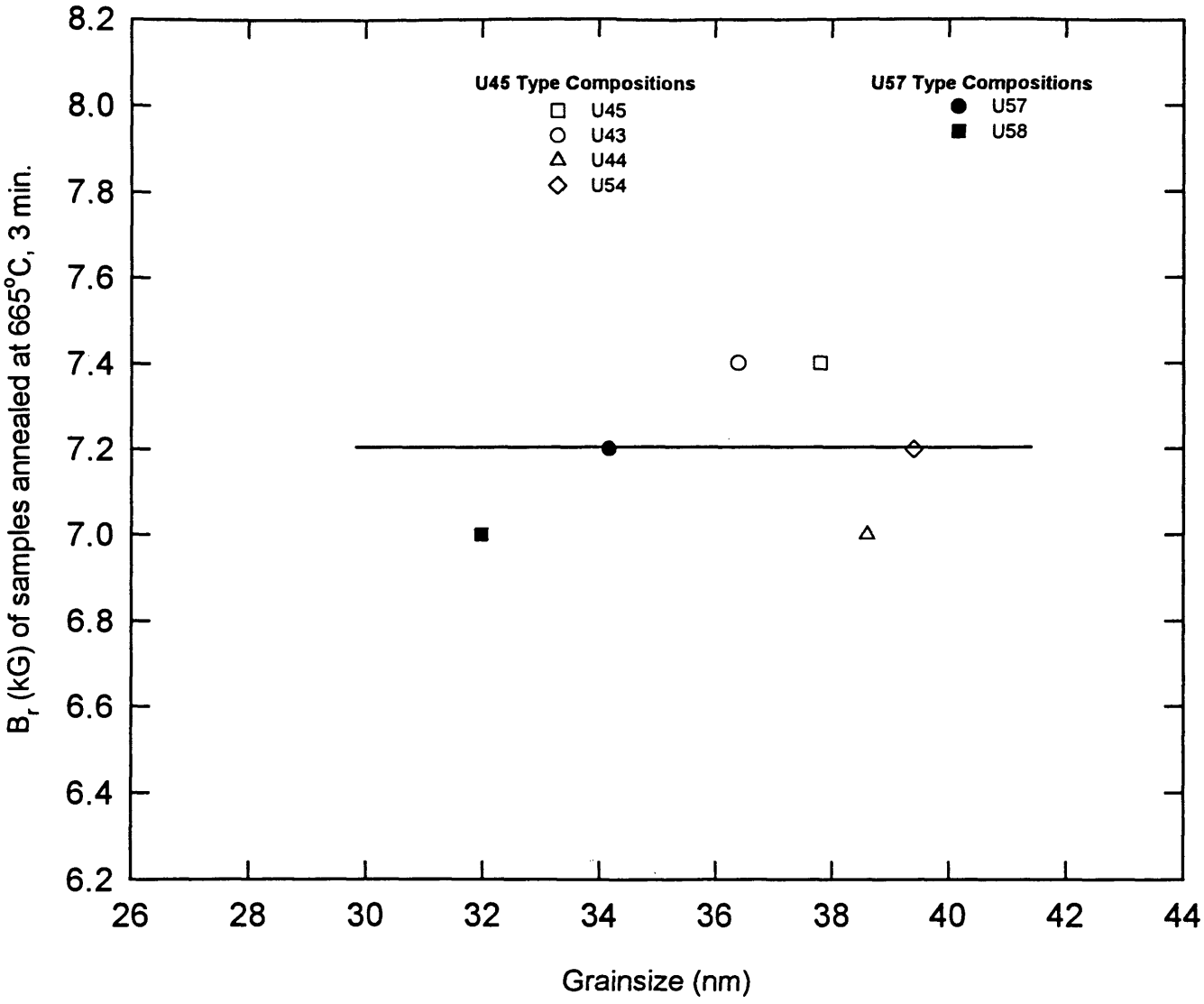

Figure 5-4: Remanence B_r of samples annealed at 665°C for 3 min as a function of the measured grainsize.

Lattice strain gradients in a sample can also generate line broadening. Theoretically, the line broadening generated by lattice strain can be distinguished from the line broadening generated by grainsize refinement. Unfortunately, the x-ray patterns developed in this alloy do not have enough higher order peaks to use the theoretical line broadening separation techniques. In the Scherrer equation calculations, as line broadening increases, the grainsizes calculated decrease. There is another source of line broadening that was not previously discussed. Compositional gradients in a crystal can locally change the lattice parameters, and therefore cause a line broadening. It is probable that these samples have compositional gradients because of their rapid crystallization, and because the 2-14-1 phase should have significant solid solubility for several of the alloying agents. Therefore, the line broadening generated by compositional variation is another source of error in the grainsize measurements made in this study. The grainsizes reported in this study may be finer than the actual grainsizes of the microstructures.

Unfortunately, no TEM sample preparation technique was available for the research conducted at the Colorado School of Mines. Without TEM measurements, no accurate confirmations of the grainsizes measured with the XRD technique were possible. Rhodia conducted an independent TEM study on an alloy with a similar composition. The Rhodia TEM pictures show an average grainsize of 40-50 nm, which correlates well with the grainsizes reported by the XRD analysis. In addition, several other authors have reported nano-structured alloys with 2-14-1 grainsizes on the order of 20-50 nm [28,30], when investigating similar alloys. It is clear that the grainsizes determined by the XRD technique are in reasonable agreement, but the absolute accuracy cannot be established without TEM analysis of the same samples studied by XRD.

5.4 Refractory Metal Additions

Niobium and titanium additions were made to this alloy system to tie up the excess boron. It was hoped that a fine distribution of titanium and niobium borides would precipitate to inhibit grain growth and improve intrinsic coercivities by preventing the formation and growth of reverse domains. Although there is no direct evidence of boride precipitation, thermodynamic analysis predicts the formation of very stable borides of both niobium and titanium. Free energy of precipitation (ΔG) as a function of temperature plots suggest that the refractory metal borides may be precipitated within the melt. The fact that the grainsize developed during quenching is the same as the grainsize of fully annealed samples in two of the alloys examined, supports the idea that the refractory metal borides are acting to prevent grain growth during quenching. If this is the case, then the borides must have been precipitated prior to casting.

The refractory additions of niobium and titanium seem to be effective at inhibiting grain growth in the alloys examined. In all of the alloys with refractory metal additions, the reported grainsizes (30-40 nm) are finer than in the N28 alloy (40-50 nm), which did not contain any refractory metal additions. It is interesting that the grainsizes of the samples with refractory metal additions did not seem to vary within a given composition independent of annealing time or temperature. This lack of grain growth may be attributable to the precipitation of refractory metal borides. However, the N28 alloy did not experience any grain growth beyond 50 nm, even in high temperature anneals for extended time periods. Is there a natural limit to the grain growth in this alloy system?

It is hard to say whether niobium or titanium additions were more successful at inhibiting grain growth. There is no detectable difference in the grainsize between the samples doped with 2% Nb and the samples doped with 2% Ti. The U57 and U58 alloys that were doped 1% Nb and 1% Ti showed the finest reported grainsizes at 30-34 nm. This is about a 7-8 nm reduction in grainsize

compared to the alloys doped with 2% additions. It is not clear why the U57 and U58 alloys had the finest grainsizes. The reduction may be due to the smaller percentages of additions in these alloys. If the 1% titanium and 1% niobium additions act independently when precipitating borides, then the individually smaller additions may result in a finer distribution of borides being precipitated, which could result in a more effective grain growth inhibiting matrix. Titanium borides may have a different morphological shape and/or precipitate distribution than niobium borides, and therefore the two borides may act differently to pin grain boundaries. If this is the case, then niobium and titanium borides acting in concert may be more effective at preventing grain growth. Regardless of the method of grainsize reduction, the decrease in grainsize seen in the U57 and U58 alloys did not generate improved magnetic properties.

It is hard to state whether niobium or titanium additions are better at enhancing magnetic performance. The U43 and U45 alloy samples, which contained 2% Nb additions, that were annealed under standard annealing conditions (665°C, 3 min), showed the best magnetic properties of the samples studied. The remanences B_r of the U23 alloy, which contained 2% Ti additions, were higher than the B_r values of the alloys with Nb additions. Unfortunately, the intrinsic coercivities in the U23 alloy were inferior to the niobium alloys. However, the large amount of crystalline $Nd_2Fe_{14}B$ present in the U23-HEAD sample (19%) could be responsible for the poor coercivities. Titanium may be a better addition from a magnetic standpoint, if the coercivity of the U23 system could be improved.

5.5 Residual Grain Boundary Phase

Mössbauer spectroscopy reported the presence of a retained residual magnetic phase in all of the annealed samples of the refractory metal containing alloys. The question was addressed if this was retained amorphous precursor left from the initial severe quenching, or if a new phase had been detected. The powders were generated by rapidly quenching a homogenous molten alloy into a metallic glass. Therefore, the alloy powders were received in a highly amorphous state. As the amorphous matrix was heat-treated, the thermal energy of the system was raised to the point where diffusion was no longer arrested, and precipitation of crystallites was initiated. The crystallization process is an ordering of the amorphous matrix into specific repetitive crystal patterns by diffusion of the atoms needed to build the crystal into the phase precipitating, and possible rejection of insoluble atoms. As the crystallites grow, the composition of the uncrystallized amorphous matrix is continually changing. After annealing the composition of the residual magnetic phase does not even resemble the composition of the initial amorphous matrix.

It is suggested that the residual magnetic phase detected by Mössbauer spectroscopy is actually a disordered grain boundary phase composed of the residual elements not consumed during crystallization. The highly disordered nature of this phase would make it difficult to distinguish from a true amorphous phase. Therefore, the microstructure would consist of nano-crystals of $Nd_2Fe_{14}B$ surrounded by residual grain boundary phase. Grain boundary thickness calculations show that because of the extremely fine grain size of these microstructures, 15% - 30% of the volume of the matrix can easily be accommodated in the grain boundary regions, and therefore account for the phase fraction detected by Mössbauer analysis. It is suggested that it is exchange coupling between the $Nd_2Fe_{14}B$ hard magnetic crystallites and the surrounding thin layer of soft magnetic residual grain boundary phase that is

producing the enhanced remanence detected in these alloys.

5.6 Final Comments and Suggestions for Further Work

The primary conclusion of this study is that yes, Mössbauer spectroscopy and x-ray diffraction can be powerful tools to examine the nano-scale microstructures of Nd-Fe-B alloy powders. By coordinating Mössbauer phase distribution results with x-ray diffraction grainsize results and the measured magnetic properties of annealed samples, several insights into the nano-scale microstructures of these alloys are gained. Ultimate optimization of the microstructure and therefore magnetic properties will be dependent on seeing morphological variation. High resolution TEM analysis is critical to confirming predictions made in this thesis, and may be the key to future process control predictions to optimize these alloys for a bonded magnet market. Further research should focus on developing an effective TEM sample preparation technique, so that high-resolution microstructural evaluation can be used to confirm the suggestions of this thesis, and further microstructural optimization can begin.

The high remanence values experienced in the U23 alloy indicate that titanium additions may generate a larger enhanced remanence than niobium additions. Unfortunately, the coercivities of the U23 alloy samples were poor. However, the U23-HEAD sample did contain a large volume fraction of 2-14-1 crystallites (19%). The large fraction of crystallites in the head sample may be responsible for the poor coercivities. An in depth investigation of titanium additions may prove that the U23 alloy's coercivities could be improved while maintaining the high remanence values provided that the amount of crystallization generated during quenching could be impeded.

Although the magnetic properties did not improve in the U57 and U58 samples that contained titanium and niobium additions, the reduced grainsize is intriguing. Theoretical sources indicate that reducing the grainsize below 15 nm

could further enhance the remanence values [4,5]. By altering the quantity and type of additions made, the grainsize might be drastically reduced. Further investigation of addition quantities needs to be thoroughly investigated to see if further grainsize reductions can be achieved.

A different annealing scheme may also inhibit grain growth. As the annealing temperature is increased, the amount of energy available for crystallite nucleation is increased. A high temperature flash anneal may increase the nucleation rate of 2-14-1 crystallites. With more nuclei growing, grain boundary motion impingement should increase because of grain boundary impingement. A study of high temperature impulse annealing may generate some interesting results.

Current work suggests that the residual grain boundary phase has a soft-magnetic behavior at room temperature. Firm confirmation of the existence and properties of this proposed phase has not been determined to date. Remember that magnetic phases experience six-line Zeeman splitting of ^{57}Fe absorption spectral lines. Above their Curie temperature, all ferromagnetic phases lose their metastable magnetic properties. An experiment, in which Mössbauer scans were measured while an absorber wafer was heated to various temperatures, could show the collapse of a six-line Zeeman absorption pattern to a two line pattern for the residual disordered grain boundary phase at its Curie temperature.

This thesis suggested that refractory metal borides may be precipitated in the melt prior to quenching. If borides are precipitated prior to quenching, then they may have a different density then the melt. Therefore, boride particles may float to the top if they attain sufficient buoyancy, or sink to the bottom. In either case, a chemical analysis of the alloy ribbon at different pouring times may show a gradient in refractory metal concentration. The refractory metal borides were undetectable by x-ray diffraction in the head samples, because the head samples always contained some crystalline 2-14-1, which produced diffraction peaks that interfered with boride detection. Analysis of a fully amorphous head sample may indicate the presence of borides in the as-quenched material.

REFERENCES CITED

[1] Halliday, D., Resnick, R., Walker, J. 1997. Fundamentals of Physics, Fifth Edition. New York: John Wiley & Sons, Inc.: 793-799.

[2] Coey, J.M.D., ed. 1996. Rare-earth Iron Permanent Magnets. New York: Oxford University Press, Inc.

[3] 1974. International Tables for X-ray Crystallography. Birmingham, England: Kynoch Press.

[4] Fischer, R., Schrefl, T., Kronmuller, H., Fidler, J. 1996. Grain-size dependence of remanence and coercive field of isotropic nanocrystalline composite permanent magnets. *J. of Magnetism and Magnetic Mat*, 153: 35-49.

[5] Kneller, E., Hawig, R. 1991. The exchange-spring magnet: a new material principle for permanent magnets. *IEEE Transactions on Magnetics*, 27: 3588-3600.

[6] Schrefl, T., Kronmuller, H., Fidler, J. 1993. Exchange hardening in nano-structured two-phase permanent magnets. *J. of Magnetism and Magnetic Mat*, 127: 273-277.

[7] Skomski, R., Coey, J.M.D. 1993. Giant energy product in nanostructured two-phase magnets. *Physical Review B*, 48: 15812-15816.

[8] Skomski, R. 1994. Aligned two-phase magnets: permanent magnetism of the future? *J. Appl. Phys*, 76: 7059-7064.

[9] Tipler, Paul A. 1992. Elementary Modern Physics. New York: Worth Publishers, Inc.

[10] Williamson, D. L. Colorado School of Mines, Private Communication.

[11] Snyder, George. Mössbauer Spectrometer. Cambridge: Ealing Science Teaching: 4-9.

[12] Greenwood, N. N. 1967. The Mössbauer spectra of chemical compounds. *Chemistry in Britain*, 3: 56-72.

[13] Park, E. B., Yang, C. J. 1997. Mössbauer study on $Nd_2Fe_{14}B/Fe_3B$ composite magnet treated by an external magnetic field. *RIST*: 114-119.

[14] Pringle, O.A., Long, G. J., Tharp, D.E., James, W. J., Yang, Y. 1988. The temperature dependence of the Mössbauer hyperfine parameters in $Nd_2Fe_{14}B$. *Hyperfine Interactions,* 40: 437-440.

[15] Stevens, J. G., Stevens, V. E., ed. 1972. Mössbauer Effect Data Index Covering the 1970 Literature. New York: Plenum Data Corp. 18-20.

[16] Rosenberg, M., Deppe, P., Stadelmaier, H. 1986. Mössbauer spectroscopy of $R_2Fe_{14}B$ alloys. *Hyperfine Interactions*, 28: 503-506.

[17] Cullity, B. D. 1978. Elements of X-ray Diffraction. Menlo Park, California: Addison-Wesley Publishing Company, Inc.

[18] Hager, J. P., Williamson, D.L., Templeton, B. P. February 28,1996. Experimental Investigation of Characterization Techniques and Annealing Practice for Magnetic Nd-Fe-B Powders Produced by Melt Spinning. Report submitted to Rhône-Poulenc by CSM research team.

[19] Stephens, F. Iron Carbide Holdings, Private Communication.

[20] Hager, J. P., Williamson, D.L., Templeton, B. P. June 5,1996. Experimental Investigation of Phase Distributions in Melt-Spun Nd-Fe-B Alloys Using Mössbauer Spectrometry. Report submitted to Rhône-Poulenc by CSM research team.

[21] Brand, R. A., Lauer, J., Herlach, D. M. 1983. The evaluation of hyperfine field distributions in overlapping and asymmetric Mössbauer spectra: a study of the amorphous alloy $Pd_{77.5-x}Cu_6Si_{16.5}Fe_x$. *J. Phys. F: Met. Phys.,* 13: 675-683.

[22] Archambault, V. August 19, 1997. Crystallite Size Determination. Rhône-Poulenc report. Reference: N° 3531.

[23] Templeton, B.P., Hager, J. P., Williamson, D. L. October 5,1996. Use of X-ray Diffraction to Measure Changes in the $Nd_2Fe_{14}B$ Grain Size for Melt-Spun Alloys Annealed at CSM. Report submitted to Rhône-Poulenc by CSM research team.

[24] Archambault, V. October 10, 1997 Crystallite size determination and TEM characterization. Rhône-Poulenc report. Reference: N°3574.

[25] Pamyatnykh, L. A., Pushkarsky, V. I., Andreev, S. V., Korznikova, G. F., Kudrevatykh, N. V., Lobanov, B. N. 1995. New structural state in melt-spun Nd-Fe-B alloys. *J. of Alloys and Compounds*, 226: 158-160.

[26] Spassov, T. 1995. Phase transformations in rapidly quenched Nd-Fe-B alloys. 123-128.

[27] Inoue, A., Takeuchi, A., Makino, A., Masumoto, T. 1994. Hard magnetic properties of nanocrystalline Fe-Nd-B alloys containing α-Fe and intergranular amorphous phase. *Met. Trans.*, 36: 676-685.

[28] Pankratz, L. B. 1994. Thermodynamic properties of carbides, nitrides, and other selected substances. Bulletin / United States Department of the Interior, Bureau of Mines.

[29] Elliot, John F., Gleiser, M., Ramakrishna, V. 1963. Thermochemistry for Steelmaking Thermodynamic and Transport Properties. Reading, MA: Addison-Wesley Pub. Co., Inc.

[30] Pehlke, R. D. 1977. Unit Processes of Extractive Metallurgy. New York: Elsevier Scientific Pub. Co., Inc.

[31] Steyaert, S., Le Breton, J. M., Ahmed, F. M., Edgley, D. S., Harris, I. R., Teillet, J. 1998. A Mössbauer investigation of the homogenisation of $Nd_{11.8}Fe_{82.3-x}Nb_xB_{5.9}$ alloys. *J. of Alloys and Compounds*, 264: 277-284.

[32] Williamson, D. L. Colorado School of Mines, Unpublished document given in Private Communication.

APPENDIX I

Quantitative Analysis of Mössbauer Spectra

The following excerpt is an unpublished explanation of quantitative analysis of Mössbauer spectra written by D. L. Williamson [32].

1-1 Theoretical Basis for Quantitative Iron Analysis

In this section we develop relations between the ^{57}Fe Mössbauer resonance area and the concentration of Fe atoms in the sample. The resonance area is a function of the effective thickness, T, of the sample:

$$T = \sigma_o \cdot f \cdot n \cdot a \cdot t \qquad [1]$$

where $\sigma_o = 2.56 \times 10^{-18}$ cm^2, f is the recoilless fraction of the Fe atoms in the sample, n is the total number of Fe atoms per unit volume of sample, a is the isotopic abundance of ^{57}Fe in the sample (0.0214 for natural abundance) and t is the sample thickness. In this work we will deal only with samples containing the natural abundance of ^{57}Fe and will be interested in the mass concentration of iron per unit area for a sample of uniform thickness. Under these conditions Equation [2] may be written:

$$T = \sigma_o \cdot f \cdot a \cdot m\ (N_o/M) = C \cdot f \cdot m \qquad [2]$$

where N_o is Avagadro's number, M is the atomic weight of Fe, and m is the mass of Fe per unit area. If m is expressed in mg/cm^2, then C = 0.591 cm^2/mg.

If one is working with an absorber in which the Fe atoms occupy more than one site, then we can define the effective thickness of the i^{th} compound or site by:

$$T_i = C \cdot f_i \cdot m_i \qquad [3]$$

The exact expression for the resonance area of the i^{th} component (compound or site) is a complicated integral expression. It has been shown, however, that provided $T_i \leq 5$ and the resonance lines are well resolved for each component, that the following expression for the area A_i is valid to better than one percent:

$$A_i = (\pi/2)\ \Gamma_o \cdot f_s \cdot K(T_i) \qquad [4]$$

where Γ_o = 0.097 mm/sec, f_s is the recoilless fraction of the source and

$$K(T_i) = T_i\ e^{-[Ti/2]}\ [\ I_o\ (T_i/2) + I_1\ (T_i/2)] \qquad [5]$$

where I_o and I_1 are modified Bessel functions of zero and first order respectively. Equation [5] assumes that the resonance line is fitted with a Lorentzian function.

The resonance associated with the i^{th} component may involve more than one resonance line due to the presence of hyperfine interactions. For example, the quadrupole interaction splits the resonance into two lines. Provided the split lines are well resolved then Equation [5] is still applicable and can be used with the same degree of accuracy to even higher values of T_i. If we introduce the notation T_{ij} for the effective thickness associated with the j^{th} hyperfine line of the i^{th} component then:

$$A_{ij} = (\pi/2)\, \Gamma_o \cdot f_s \cdot K(T_{ij}) \qquad \textbf{[6]}$$

and Equation [6] is used with T_i replaced by T_{ij}. Equation [3] is modified to:

$$T_{ij} = C \cdot f_i \cdot m_{ij} \qquad \textbf{[7]}$$

where m_{ij} now represents the mass of Fe/cm^2 giving rise to the $(ij)^{th}$ resonance line. We note here that the mass of Fe/cm^2 giving rise to the i^{th} component is $m_i = \Sigma_j\, m_{ij}$ and the total mass of Fe/cm^2 $M = \Sigma_{ij}\, m_{ij}$.

If one is interested in only the relative amount of Fe associated with the i^{th} component then the fractional area a_i is given by:

$$a_i = (\Sigma_j\, A_{ij}) \,/\, (\Sigma_{ij}\, A_{ij}) = [\, \Sigma_j\, K(T_{ij})\,] \,/\, [\, \Sigma_{ij}\, K(T_{ij})] \qquad \textbf{[8]}$$

In the case that all $T_{ij} << 1$ then $K(T_{ij}) = T_{ij}$ so that Equation [8] simplifies to:

$$a_i = (f_i \cdot m_i) / \Sigma_{ij} f_i \cdot m_{ij} \qquad \textbf{[9]}$$

Further simplification results if all f_i are assumed the same so that:

$$a_i = m_i / M \qquad \textbf{[10]}$$

Equation [10] is the most often used modification of Equation [8], but one must recognize its very limited range of applicability ($T_{ij} << 1$, $f_i = f$). Equation [10] is the equation used here to provide the relative phase fractions. Typical values of T_{ij} are often in the neighborhood of unity and recoilless fraction values typically vary from about 0.5 to about 0.8 at room temperature. Thus, use of Equation [10] can be expected to give only qualitative results in most cases. Equations [8], [9], and [10] will be valid to higher values of effective thickness than for Equation [6] due to some cancellation of error in taking ratios. Thus one can expect more accuracy in determining relative amounts of Fe than the total amount of Fe.

1-2 Experimental Determination of Resonance Area

The experimental data for a given sample are conventionally expressed as numbers of counts versus Doppler velocity in mm/sec. The spectrum is fitted with a superposition of Lorentzian lines each of which is characterized by the number of counts at maximum resonance N and the full width at half maximum

Γ. The off-resonance count rate N_∞ is also a fitted parameter of each spectrum. A background correction factor B must be determined to account for unwanted counts, which are inadvertently included in the resonance spectrum. The area of the $(ij)^{th}$ resonance line is then given by:

$$A_{ij} = B\,(\pi/2)\,\Gamma_{ij}\,[(N_\infty - N_{ij})/\,N_\infty] \qquad \textbf{[11]}$$

where Γ_{ij} is expressed in mm/sec so that A_{ij} also has these units.

Fitting complications arise when the resonance lines are not well resolved. In such cases some restrictions may be required in order to get a reasonable fit. For example, the restriction that all lines have equal widths is valuable for overlapping resonance lines.

APPENDIX II

Origional XRD Data for Grainsize Analysis

N28 Series

SAMPLE	Peak	2θ	COSθ	FWHM	d	LaB_6 FWHM	B (deg)	B (rad)	t (Å)	t(nm)	STDev
N28-600-2	311	32.95	0.959	0.268	2.716	0.1085	0.2455	0.00428	337.5	33.7	
	214	37.24	0.948	0.242	2.413	0.1049	0.2177	0.00380	385.1	38.5	
	313	39.17	0.942	0.228	2.298	0.1037	0.2026	0.00354	416.2	41.6	
										38.0	**3.97**
N28-600-4	311	32.88	0.959	0.274	2.722	0.1085	0.2515	0.00439	329.3	32.9	
	214	37.11	0.948	0.277	2.420	0.1050	0.2568	0.00448	326.4	32.6	
	313	39.08	0.942	0.247	2.303	0.1037	0.2244	0.00392	375.6	37.6	
										34.4	**2.76**
N28-600-4-R1	311	33.05	0.959	0.283	2.708	0.1084	0.2612	0.00456	317.2	31.7	
	214	37.28	0.948	0.271	2.410	0.1049	0.2497	0.00436	335.8	33.6	
	313	39.25	0.942	0.236	2.294	0.1036	0.2120	0.00370	397.8	39.8	
										35.0	**4.22**
N28-600-4-R2	311	33.03	0.959	0.255	2.710	0.1084	0.2310	0.00403	358.7	35.9	
	214	37.27	0.948	0.287	2.411	0.1049	0.2668	0.00466	314.2	31.4	
	313	39.22	0.942	0.249	2.295	0.1036	0.2268	0.00396	371.8	37.2	
										34.8	**3.02**
						600° C, 4 MINUTE ANNEALING AVERAGE =				***34.7***	**2.95**
N28-600-5.5	311	32.94	0.959	0.231	2.717	0.1085	0.2034	0.00355	407.2	40.7	
	214	37.19	0.948	0.230	2.416	0.1050	0.2047	0.00357	409.5	41.0	
	313	39.14	0.942	0.204	2.300	0.1037	0.1756	0.00307	480.0	48.0	
										43.2	**4.14**
N28-600-7	311	32.98	0.959	0.213	2.714	0.1084	0.1835	0.00320	451.5	45.2	
	214	37.24	0.948	0.233	2.412	0.1049	0.2078	0.00363	403.4	40.3	
	313	39.19	0.942	0.187	2.297	0.1036	0.1562	0.00273	540.0	54.0	
										46.5	**6.93**

N28 Series - Continued

SAMPLE	Peak	2θ	COSθ	FWHM	d	LaB_6 FWHM	B (deg)	B (rad)	t (Å)	t(nm)	STDev
N28-600-15	311	32.96	0.959	0.202	2.716	0.1085	0.1704	0.00297	486.3	48.6	
	214	37.23	0.948	0.210	2.413	0.1049	0.1814	0.00317	462.2	46.2	
	313	39.17	0.942	0.187	2.298	0.1037	0.1558	0.00272	541.4	54.1	
										49.7	**4.06**
N28-680-90	311	33.07	0.959	0.196	2.707	0.1084	0.1636	0.00286	506.4	50.6	
	214	37.36	0.947	0.211	2.405	0.1048	0.1834	0.00320	457.3	45.7	
	313	39.28	0.942	0.212	2.292	0.1036	0.1847	0.00322	456.8	45.7	
										47.4	**2.85**
N28-700-120	311	33.06	0.959	0.203	2.707	0.1084	0.1718	0.00300	482.4	48.2	
	214	37.36	0.947	0.202	2.405	0.1048	0.1722	0.00300	487.1	48.7	
	313	39.28	0.942	0.192	2.292	0.1036	0.1615	0.00282	522.4	52.2	
										49.7	**2.19**
N28-750-60	311	33.03	0.959	0.179	2.710	0.1084	0.1423	0.00248	582.2	58.2	
	214	37.33	0.947	0.187	2.407	0.1049	0.1549	0.00270	541.3	54.1	
	313	39.25	0.942	0.194	2.294	0.1036	0.1641	0.00286	513.8	51.4	
										54.6	**3.44**
N28-750-60-R1	311	32.96	0.959	0.202	2.716	0.1085	0.1705	0.00298	486.0	48.6	
	214	37.25	0.948	0.202	2.412	0.1049	0.1720	0.00300	487.3	48.7	
	313	39.17	0.942	0.178	2.298	0.1037	0.1441	0.00252	585.0	58.5	
										51.9	**5.68**
N28-750-60-R2	311	32.93	0.959	0.210	2.718	0.1085	0.1800	0.00314	460.2	46.0	
	214	37.22	0.948	0.215	2.414	0.1049	0.1875	0.00327	447.0	44.7	
	313	39.14	0.942	0.214	2.300	0.1037	0.1875	0.00327	449.7	45.0	
										45.2	**0.70**
									750° C, 60 MINUTE ANNEALING AVERAGE =	***50.6***	**5.35**

U45 Series

SAMPLE	Peak	2θ	COSθ	FWHM	d	LaB_6 FWHM	B (deg)	B (rad)	t (Å)	t(nm)	STDev
U45-67-S4	212	26.96	0.972	0.250	3.305	0.1151	0.2225	0.00388	367.2	36.7	
	311	33.02	0.959	0.261	2.710	0.1084	0.2379	0.00415	348.3	34.8	
	214	37.30	0.947	0.223	2.409	0.1049	0.1974	0.00344	424.8	42.5	
	313	39.23	0.942	0.249	2.295	0.1036	0.2260	0.00394	373.2	37.3	
										37.8	**3.27**
U45-69-S6	212	26.95	0.972	0.255	3.306	0.1151	0.2279	0.00398	358.4	35.8	
	311	33.02	0.959	0.267	2.711	0.1084	0.2442	0.00426	339.3	33.9	
	214	37.29	0.948	0.240	2.410	0.1049	0.2155	0.00376	389.0	38.9	
	313	39.22	0.942	0.233	2.295	0.1036	0.2092	0.00365	403.1	40.3	
										37.2	**2.89**
U45-69-S8	212	26.95	0.972	0.255	3.306	0.1151	0.2272	0.00397	359.5	36.0	
	311	33.01	0.959	0.266	2.711	0.1084	0.2430	0.00424	341.0	34.1	
	214	37.29	0.948	0.251	2.409	0.1049	0.2279	0.00398	367.9	36.8	
	313	39.23	0.942	0.251	2.295	0.1036	0.2283	0.00398	369.4	36.9	
										35.9	**1.31**
U45-750-60	212	26.95	0.972	0.249	3.306	0.1151	0.2207	0.00385	370.2	37.0	
	311	33.02	0.959	0.268	2.711	0.1084	0.2456	0.00429	337.3	33.7	
	214	37.30	0.947	0.243	2.409	0.1049	0.2189	0.00382	383.0	38.3	
	313	39.23	0.942	0.253	2.294	0.1036	0.2309	0.00403	365.3	36.5	
										36.4	**1.92**

U43 Series

SAMPLE	Peak	2θ	COSθ	FWHM	d	LaB_6 FWHM	B (deg)	B (rad)	t (Å)	t(nm)	STDev
U43-70-S3	212	26.93	0.973	0.257	3.308	0.1151	0.2296	0.00401	355.8	35.6	
	311	33.00	0.959	0.273	2.712	0.1084	0.2509	0.00438	330.2	33.0	
	214	37.28	0.948	0.243	2.410	0.1049	0.2193	0.00383	382.3	38.2	
	313	39.21	0.942	0.240	2.296	0.1036	0.2167	0.00378	389.1	38.9	
										36.4	**2.69**
U43-71-S3	212	26.96	0.972	0.244	3.305	0.1151	0.2151	0.00375	379.8	38.0	
	311	33.02	0.959	0.267	2.710	0.1084	0.2439	0.00426	339.7	34.0	
	214	37.30	0.947	0.241	2.409	0.1049	0.2173	0.00379	385.9	38.6	
	313	39.23	0.942	0.249	2.294	0.1036	0.2263	0.00395	372.8	37.3	
										37.0	**2.06**
U43-71-S5	212	26.92	0.973	0.254	3.309	0.1151	0.2267	0.00396	360.3	36.0	
	311	32.99	0.959	0.261	2.713	0.1084	0.2376	0.00415	348.7	34.9	
	214	37.27	0.948	0.230	2.411	0.1049	0.2046	0.00357	409.8	41.0	
	313	39.21	0.942	0.251	2.296	0.1036	0.2284	0.00399	369.3	36.9	
										37.2	**2.66**
U43-750-60	212	26.97	0.972	0.239	3.303	0.1150	0.2095	0.00366	390.0	39.0	
	311	33.04	0.959	0.256	2.709	0.1084	0.2322	0.00405	356.8	35.7	
	214	37.33	0.947	0.245	2.407	0.1049	0.2214	0.00386	378.8	37.9	
	313	39.26	0.942	0.255	2.293	0.1036	0.2330	0.00407	361.9	36.2	
										37.2	**1.53**

U44 Series

SAMPLE	Peak	2θ	COSθ	FWHM	d	LaB_6 FWHM	B (deg)	B (rad)	t (Å)	t(nm)	STDev
U44-HEAD	212	26.87	0.973	0.282	3.315	0.1152	0.2576	0.00450	317.1	31.7	
	311	32.92	0.959	0.288	2.719	0.1085	0.2665	0.00465	310.9	31.1	
	214	37.21	0.948	0.288	2.414	0.1050	0.2684	0.00468	312.3	31.2	
	313	39.13	0.942	0.283	2.300	0.1037	0.2631	0.00459	320.4	32.0	
										31.5	**0.44**
U44-750-60	212	26.93	0.973	0.276	3.308	0.1151	0.2505	0.00437	326.1	32.6	
	311	33.00	0.959	0.267	2.712	0.1084	0.2442	0.00426	339.3	33.9	
	214	37.29	0.948	0.254	2.409	0.1049	0.2311	0.00403	362.8	36.3	
	313	39.22	0.942	0.250	2.295	0.1036	0.2274	0.00397	370.8	37.1	
										35.0	**2.07**
U44-73-S5	212	26.87	0.973	0.250	3.315	0.1152	0.2215	0.00387	368.7	36.9	
	311	32.94	0.959	0.247	2.717	0.1085	0.2221	0.00388	373.0	37.3	
	214	37.22	0.948	0.238	2.414	0.1049	0.2133	0.00372	393.0	39.3	
	313	39.15	0.942	0.255	2.299	0.1037	0.2327	0.00406	362.3	36.2	
										37.4	**1.33**
U44-73-S11	212	26.89	0.973	0.230	3.312	0.1151	0.1987	0.00347	411.1	41.1	
	311	32.96	0.959	0.254	2.715	0.1085	0.2299	0.00401	360.4	36.0	
	214	37.23	0.948	0.232	2.413	0.1049	0.2066	0.00361	405.8	40.6	
	313	39.16	0.942	0.228	2.298	0.1037	0.2035	0.00355	414.3	41.4	
										39.8	**2.52**
U44-75-S3	212	26.95	0.972	0.237	3.305	0.1151	0.2077	0.00363	393.3	39.3	
	311	33.02	0.959	0.257	2.711	0.1084	0.2328	0.00406	355.9	35.6	
	214	37.29	0.948	0.231	2.409	0.1049	0.2055	0.00359	408.1	40.8	
	313	39.23	0.942	0.235	2.295	0.1036	0.2113	0.00369	399.2	39.9	
										38.9	**2.30**

U44 Series - Continued

SAMPLE	Peak	2θ	COSθ	FWHM	d	LaB_6 FWHM	B (deg)	B (rad)	t (Å)	t(nm)	STDev
U44-75-S5	212	26.92	0.973	0.235	3.310	0.1151	0.2054	0.00358	397.8	39.8	
	311	32.99	0.959	0.239	2.713	0.1084	0.2133	0.00372	388.4	38.8	
	214	37.26	0.948	0.232	2.411	0.1049	0.2069	0.00361	405.2	40.5	
	313	39.19	0.942	0.237	2.297	0.1036	0.2130	0.00372	395.8	39.6	
										39.7	**0.69**
U44-75-S8	212	26.95	0.972	0.235	3.306	0.1151	0.2045	0.00357	399.4	39.9	
	311	33.02	0.959	0.259	2.711	0.1084	0.2357	0.00411	351.6	35.2	
	214	37.29	0.948	0.237	2.409	0.1049	0.2123	0.00370	395.0	39.5	
	313	39.22	0.942	0.250	2.295	0.1036	0.2276	0.00397	370.5	39.5	
										38.9	**2.25**

U54 Series

SAMPLE	Peak	2θ	COSθ	FWHM	d	LaB_6 FWHM	B (deg)	B (rad)	t (Å)	t(nm)	STDev
U54-HEAD	212	26.88	0.973	0.220	3.314	0.1152	0.1873	0.00327	436.2	43.6	
	311	32.95	0.959	0.254	2.716	0.1085	0.2296	0.00401	360.8	36.1	
	214	37.24	0.948	0.227	2.412	0.1049	0.2018	0.00352	415.3	41.5	
	313	39.29	0.942	0.243	2.292	0.1036	0.2196	0.00383	384.1	38.4	
										39.9	**3.33**
U54-750-60	212	26.86	0.973	0.227	3.316	0.1152	0.1953	0.00341	418.3	41.8	
	311	32.93	0.959	0.246	2.718	0.1085	0.2207	0.00385	375.4	37.5	
	214	37.22	0.948	0.242	2.413	0.1049	0.2180	0.00380	384.6	38.5	
	313	39.15	0.942	0.237	2.299	0.1037	0.2132	0.00372	395.6	39.6	
										39.3	**1.85**
U54-87-S3	212	26.91	0.973	0.241	3.311	0.1151	0.2119	0.00370	385.6	38.6	
	311	32.96	0.959	0.231	2.715	0.1085	0.2038	0.00356	406.4	40.6	
	214	37.25	0.948	0.218	2.412	0.1049	0.1913	0.00334	438.2	43.8	
	313	39.17	0.942	0.228	2.298	0.1037	0.2032	0.00355	415.0	41.5	
										41.1	**2.18**
U54-87-S6	212	26.89	0.973	0.237	3.312	0.1151	0.2071	0.00361	394.4	39.4	
	311	32.95	0.959	0.239	2.716	0.1085	0.2125	0.00371	389.8	39.0	
	214	37.24	0.948	0.231	2.413	0.1049	0.2061	0.00360	406.8	40.7	
	313	39.17	0.942	0.234	2.298	0.1037	0.2102	0.00367	401.1	40.1	
										39.8	**0.75**
U54-87-S8	212	26.88	0.973	0.255	3.314	0.1152	0.2278	0.00398	358.6	35.9	
	311	32.94	0.959	0.257	2.717	0.1085	0.2328	0.00406	355.8	35.6	
	214	37.23	0.948	0.240	2.413	0.1049	0.2161	0.00377	387.9	38.8	
	313	39.16	0.942	0.239	2.299	0.1037	0.2155	0.00376	391.3	39.1	
										37.3	**1.88**

U23 Series

SAMPLE	Peak	2θ	COSθ	FWHM	d	LaB_6 FWHM	B (deg)	B (rad)	t (Å)	t(nm)	STDev
U23-HEAD	4 1 0	42.22	0.933	0.267	2.139	0.1349	0.2304	0.00402	369.6	37.0	
	2 1 4	37.22	0.948	0.281	2.414	0.1366	0.2452	0.00428	341.9	34.2	
	3 1 1	32.88	0.959	0.257	2.722	0.1385	0.2162	0.00377	383.2	38.3	
	2 1 2	26.84	0.973	0.288	3.320	0.1419	0.2501	0.00437	326.5	32.7	
										35.5	**2.58**
U23-42-S1	4 1 0	42.23	0.933	0.253	2.138	0.0999	0.2326	0.00406	366.0	36.6	
	2 1 4	37.24	0.948	0.236	2.412	0.1016	0.2131	0.00372	393.4	39.3	
	3 1 1	32.89	0.959	0.245	2.721	0.1036	0.2225	0.00388	372.3	37.2	
	2 0 4	35.76	0.952	0.234	2.509	0.1022	0.2103	0.00367	396.9	39.7	
	2 1 2	26.85	0.973	0.232	3.317	0.1070	0.2056	0.00359	397.3	39.7	
										38.5	**1.49**
U23-42-S1-R	4 1 0	42.37	0.932	0.253	2.132	0.1020	0.2319	0.00405	367.4	36.7	
	2 1 4	37.39	0.947	0.230	2.403	0.1048	0.2042	0.00356	410.8	41.1	
	3 1 1	33.05	0.959	0.242	2.709	0.1084	0.2158	0.00377	383.9	38.4	
	2 0 4	35.91	0.951	0.218	2.499	0.1059	0.1902	0.00332	439.1	43.9	
	2 1 2	27.00	0.972	0.250	3.300	0.1150	0.2225	0.00388	367.3	36.7	
										39.4	**3.10**
U23-43-S1	4 1 0	42.35	0.932	0.257	2.132	0.0999	0.2368	0.00413	359.8	36.0	
	2 1 4	37.87	0.946	0.227	2.374	0.1014	0.2027	0.00354	414.4	41.4	
	3 1 1	33.03	0.959	0.251	2.710	0.1035	0.2290	0.00400	361.8	36.2	
	2 0 4	35.90	0.951	0.218	2.500	0.1022	0.1926	0.00336	433.7	43.4	
	2 1 2	26.98	0.972	0.233	3.302	0.1069	0.2072	0.00362	394.3	39.4	
										39.3	**3.24**

U23 Series - Continued

SAMPLE	Peak	2θ	COSθ	FWHM	d	LaB_6 FWHM	B (deg)	B (rad)	t (Å)	t(nm)	STDev
U23-45-S1	4 1 0	42.27	0.933	0.257	2.136	0.0999	0.2371	0.00414	359.3	35.9	
	2 1 4	37.29	0.948	0.230	2.409	0.1016	0.2068	0.00361	405.5	40.5	
	3 1 1	32.94	0.959	0.258	2.717	0.1035	0.2361	0.00412	350.9	35.1	
	2 0 4	35.82	0.952	0.232	2.505	0.1022	0.2081	0.00363	401.3	40.1	
	2 1 2	26.90	0.973	0.237	3.312	0.1069	0.2120	0.00370	385.2	38.5	
										38.0	**2.45**
U23-700-60	4 1 0	42.31	0.933	0.263	2.134	0.0999	0.2437	0.00425	349.5	35.0	
	2 1 4	37.32	0.947	0.230	2.407	0.1016	0.2059	0.00359	407.2	40.7	
	3 1 1	32.97	0.959	0.250	2.714	0.1035	0.2280	0.00398	363.3	36.3	
	2 0 4	35.85	0.951	0.224	2.503	0.1022	0.1996	0.00348	418.3	41.8	
	2 1 2	26.93	0.973	0.233	3.309	0.1069	0.2075	0.00362	393.6	39.4	
										38.6	**2.91**
U23-750-60	4 1 0	42.34	0.932	0.251	2.133	0.0999	0.2302	0.00402	370.1	37.0	
	2 1 4	37.83	0.946	0.223	2.376	0.1014	0.1985	0.00346	423.1	42.3	
	3 1 1	33.01	0.959	0.240	2.711	0.1035	0.2170	0.00379	381.8	38.2	
	2 0 4	35.84	0.951	0.228	2.503	0.1022	0.2033	0.00355	410.6	41.1	
	2 1 2	26.95	0.972	0.241	3.305	0.1069	0.2164	0.00378	377.5	37.7	
										39.3	**2.30**

U57 Series

SAMPLE	Peak	2θ	COSθ	FWHM	d	LaB_6 FWHM	B (deg)	B (rad)	t (Å)	t(nm)	STDev
U57-HEAD	212	26.85	0.973	0.244	3.318	0.1152	0.2152	0.00376	379.5	37.9	
	311	32.92	0.959	0.261	2.718	0.1085	0.2370	0.00414	349.5	35.0	
	214	37.22	0.948	0.251	2.414	0.1049	0.2281	0.00398	367.6	36.8	
	313	39.13	0.942	0.276	2.300	0.1037	0.2553	0.00446	330.3	33.0	
										35.7	**2.15**
U57-750-60	212	26.95	0.972	0.278	3.306	0.1151	0.2529	0.00441	323.0	32.3	
	311	33.01	0.959	0.278	2.711	0.1084	0.2558	0.00446	324.0	32.4	
	214	37.31	0.947	0.266	2.408	0.1049	0.2448	0.00427	342.4	34.2	
	313	39.23	0.942	0.268	2.295	0.1036	0.2473	0.00432	341.1	34.1	
										33.3	**1.06**
U57-88-S1	212	26.89	0.973	0.255	3.313	0.1151	0.2272	0.00396	359.6	36.0	
	311	32.94	0.959	0.271	2.717	0.1085	0.2485	0.00434	333.3	33.3	
	214	37.24	0.948	0.236	2.413	0.1049	0.2117	0.00369	396.0	39.6	
	313	39.15	0.942	0.271	2.299	0.1037	0.2504	0.00437	336.7	33.7	
										35.6	**2.89**
U57-88-S2	212	26.83	0.973	0.284	3.321	0.1152	0.2600	0.00454	314.1	31.4	
	311	32.89	0.959	0.290	2.721	0.1085	0.2692	0.00470	307.7	30.8	
	214	37.19	0.948	0.255	2.416	0.1050	0.2321	0.00405	361.1	36.1	
	313	39.11	0.942	0.268	2.301	0.1037	0.2476	0.00432	340.5	34.1	
										33.1	**2.47**
U57-88-S3	212	26.85	0.973	0.265	3.317	0.1152	0.2383	0.00416	342.7	34.3	
	311	32.91	0.959	0.290	2.720	0.1085	0.2687	0.00469	308.2	30.8	
	214	37.20	0.948	0.258	2.415	0.1050	0.2361	0.00412	355.0	35.5	
	313	39.13	0.942	0.272	2.300	0.1037	0.2512	0.00438	335.7	33.6	
										33.5	**1.98**

U58 Series

SAMPLE	Peak	2θ	COSθ	FWHM	d	LaB_6 FWHM	B (deg)	B (rad)	t (Å)	t(nm)	STDev
U58-750-60	212	26.91	0.973	0.296	3.311	0.1151	0.2730	0.00477	299.2	29.9	
	311	32.97	0.959	0.308	2.714	0.1084	0.2886	0.00504	287.1	28.7	
	214	37.27	0.948	0.273	2.411	0.1049	0.2519	0.00440	332.8	33.3	
	313	39.19	0.942	0.300	2.297	0.1036	0.2816	0.00492	299.4	29.9	
										30.5	**1.96**
U58-89-S1	212	26.87	0.973	0.274	3.315	0.1152	0.2484	0.00434	328.8	32.9	
	311	32.93	0.959	0.310	2.718	0.1085	0.2909	0.00508	284.8	28.5	
	214	37.21	0.948	0.263	2.414	0.1049	0.2408	0.00420	348.1	34.8	
	313	39.14	0.942	0.283	2.300	0.1037	0.2635	0.00460	320.0	32.0	
										32.0	**2.65**
U58-89-S2	212	26.84	0.973	0.301	3.319	0.1152	0.2785	0.00486	293.3	29.3	
	311	32.90	0.959	0.306	2.720	0.1085	0.2858	0.00499	289.8	29.0	
	214	37.18	0.948	0.257	2.416	0.1050	0.2345	0.00409	357.4	35.7	
	313	39.11	0.942	0.278	2.301	0.1037	0.2577	0.00450	327.2	32.7	
										31.7	**3.18**
U58-89-S3	212	26.90	0.973	0.299	3.312	0.1151	0.2755	0.00481	296.5	29.7	
	311	32.97	0.959	0.317	2.715	0.1085	0.2975	0.00519	278.5	27.9	
	214	37.25	0.948	0.259	2.412	0.1049	0.2365	0.00413	354.5	35.5	
	313	39.17	0.942	0.282	2.298	0.1037	0.2621	0.00458	321.7	32.2	
										31.3	**3.30**

BIOGRAPHICAL NOTE

The author, Bryan Patrick Templeton, was born in Niskayuna, New York on March 18, 1972. His parents Hugh and Bonnie Templeton raised him. He moved quite a bit when he was younger, attending three different elementary schools in New York and New Jersey and 2 junior high schools, one in Freehold, New Jersey and the other in Ann Arbor, Michigan. He graduated from Ann Arbor Huron High School in June of 1990.

The author started his college career at the University of Colorado in Boulder studying aerospace engineering. After a year at CU, he took a year off to establish residency in Colorado. In August of 1992, he returned to study mechanical engineering at CU. However, in December of 1992, he was offered an opportunity to transfer to a school in Australia for no additional tuition costs. From February 1993 to November 1993, the author studied civil engineering at the University of Curtin in Perth, Western Australia. The author wanted to graduate from an American university, and so he transferred to the Colorado School of Mines in January of 1994. After a semester of studying mechanical engineering at Mines, the author switched his major to metallurgical and materials engineering.

Following his junior year, the author worked at a Rhône-Poulenc rare-earth magnetic alloy production facility in Phoenix, Arizona as a metallurgical engineering summer intern in the summer of 1995. This was his first exposure to rare-earth magnetic alloy research. Following a successful summer career in

Phoenix, the author was asked to continue rare-earth magnetic alloy research during his senior year and following summer at the Colorado School of Mines.

Upon graduating from Mines with a Bachelor of Science degree in Metallurgical and Materials Engineering in August of 1996, the author immediately began pursuing a Master of Science degree under the guidance of Dr. John P. Hager.